Microscale Fracture of Composite Materials for Wind Turbine Blades

Martyniuk, Karolina; Sørensen, Bent F.; Lauridsen, Erik Mejdal; Yang, Qingda

Publication date:
2014

Document Version
Peer reviewed version

Technical University
of Denmark

Microscale Fracture of Composite Materials for Wind Turbine Blades

PhD thesis by Karolina Martyniuk

October 2013

DTU Wind Energy
Department of Wind Energy

PREFACE

This Ph.D. thesis is based on research performed between 2010 and 2013 at the Section of Composites and Materials Mechanics, Department of Wind Energy, Technical University of Denmark (formerly known as Risø National Laboratory for Sustainable Energy). The project was financially supported by the Danish Research Council and by the Danish Centre for Composites Structures and Materials for Wind Turbines.

The study has been supervised by:

Main supervisor: Prof. mso, Dr. Tech., Bent F. Sørensen (DTU Wind Energy)

Co-supervisor: Senior Scientist, Ph.D., Erik M. Lauridsen (DTU Energy Conversion and Storage)

Co-supervisor during the external research stay: Associate Professor, Ph.D., Qingda Yang (Department of Mechanical and Aerospace Engineering, University of Miami, USA)

PAPERS INCLUDED IN THE THESIS

Journal Papers

[A1] 3D *in situ* observations of glass fibre/matrix interfacial debonding.
Karolina Martyniuk, Bent F. Sørensen, Peter Modregger, Erik M. Lauridsen.
Compos Part A 55 (2013):63–73.

[A2] *In situ* determination of mixed mode fracture energy of glass fibre/matrix interface.
Karolina Martyniuk, Bent F. Sørensen, Stergios Goutianos.
Submitted to Composites Part A

[A3] Mixed mode cohesive-zone model for identification of fracture properties of a fibre/matrix interface under transverse load.
Karolina Martyniuk, Bent F. Sørensen, Qingda Yang, Wei Liu.
To be submitted to Composites Part A

Conference Papers

[B1] Mixed mode cohesive law for fibre/matrix interface- a coupled experimental and numerical study.
K. Martyniuk, B.F. Sørensen, Q. Yang, W. Liu.
Proceedings of 19th International Conference on Composite Materials (ICCM-19), July, 2013, Montreal, Canada.

The papers are referred in the thesis by their appendix number.

ACKNOWLEDGEMENTS

I sincerely thank my supervisors for their encouraging support and guidance during this study. I am grateful for their patience, inspiring ideas and shearing their knowledge with me.

I would like to thank my office mates, Mustafa Aslan and Morten Rask for all help I received from them and for making the workplace really friendly.

Furthermore, I would like to express my gratitude to Dr. Stergios Goutianos for advices and assistance with specimen design and test set up, Dr. Yukihiro Kusano, Jonas H. Kreutzfeld, Johannes Steen Bang, Christian H. Madsen, Ebtisam Abdellahi and Tom L. Andersen for help with specimen preparation, Erik Vogeley, Malcolm McGugan and Jens Olsson for technical assistance with equipment design and experimental test set up and Dr. Julie Glasscock for help with the SEM experiments. Dr. Lars Pilgaard Mikkelsen is thanked for help with numerical simulations and Hans Lilholt is acknowledged for inspiring discussions and proof reading of manuscripts included in this thesis. is thanked for the advices

I wish to thank my family, especially my dearest parents, Lucyna and Adam, and all friends for their support and belief in me. Special thanks to Reza for his love and endless patience during the final phases of this study.

SUMMARY

Due to the increase in wind turbines size it is essential that weight savings due to design changes do not compromise the reliability of the rotor blades. The reliability can be increased by improving design rules and the material models that describe the materials properties. More reliable materials models can be developed if the understanding of the microscale damage- the first stage of material failure- is increased. Therefore it is important to characterize materials' microstructures and micro-cracks initiation and propagation.

The microstructure of fibre reinforced composite materials which are the most extensively used in the rotor blades, has been shown to play an important role on the overall response of the material. The properties of a fibre/matrix interface have been found to have a significant influence on the macroscopic behavior of composites. Therefore, the characterization of the fibre/matrix interface has received a considerable attention in the research. So far, however, most of studies related to the fibre/matrix interface focus on the interface subjected to shear stresses acting parallel to the fibre direction. Thereby, the fibre/matrix interface has been characterized in terms of interfacial shear strength or Mode II interface fracture toughness. However, for the fibres oriented off the principle stress direction, fibre/matrix debonding occurs under mixed mode conditions. The mode mixity of an interfacial crack tip is not considered in many studies. It has been shown, that the fracture parameters of an interface between dissimilar materials depends on mode mixity of the crack tip. Therefore, the fracture parameters of the fibre/matrix interface must be determined in terms of mode mixity. Experimental investigation must be conducted in order to provide reliable parameters for micromechanical models.

The present PhD study is concerned with the experimental investigations of the micro-cracks initiation and propagation in the glass fibre composites with the aim of measuring the input parameters required for micromechanical modelling. A special attention is given to the determination of fracture parameters for the glass fibre/matrix

interfacial debonding and the interfacial crack kinking into the matrix by two different approaches, linear elastic fracture mechanics (LEFM) and cohesive zone approach.

The fibre/matrix debonding was investigated experimentally in 2D and in 3D in specimens containing a single fibre embedded in matrix subjected to a transverse stress. 2D *in situ* observations in the scanning electron microscope (SEM) allowed for an early detection of the debonding initiation (at the free surface of the sample), and measurements of the debond angles and normal opening displacements as functions of applied stress. The same fracture tests were carried out at the synchrotron facility where the debonding initiation and propagation were observed in 3D using X-ray tomography. The debonding was found to initiate at the free surface of the sample and subsequently it propagated into the sample along the fibre. Once the debond depth exceeded the length of two fibre diameters, the unstable crack growth (tunnelling) occurred.

The measurements obtained from testing conducted in the SEM linked with the numerical results available in the literature led to the determination of the mixed mode fracture energy of the glass fibre/matrix interface by LEFM analysis. The fracture energy for nominal Mode I was found to be ~0.2 J/m^2 and ~0.4 J/m^2 for the interfacial crack arrest and crack propagation respectively; for nominal Mode II they were found to be ~2 J/m^2 and ~3 J/m^2 respectively.

Numerical modelling of the fibre/matrix debonding was conducted by the cohesive zone approach using augmented finite element method (A-FEM). Model predictions coupled with the experimental measurements from tests carried out in the SEM allowed for the mixed mode cohesive law parameters identification and mixed mode fracture energy determination for the glass fibre/matrix interface. The Mode I cohesive peak stress and critical opening displacement have been found to be in the range of 0.75-5 MPa and <0.2 μm respectively. The Mode I fracture energy of the glass fibre/matrix interface was estimated to be ~0.1 J/m^2. The interface Mode II fracture energy is found to be ~4 times of the fracture energy for Mode I. From the model results it was found, that the interfacial debonding initiation and propagation does not depend only on the fracture

energy of the interface but is also sensitive to the cohesive law parameters within the range explored in this study.

The fibre/matrix interfacial crack kinking was analysed by coupled experimental (in 2D and in 3D) and numerical approach (in 2D). It was shown by the SEM observations of the free-edge of the sample that the kinking occurs when the debond reaches characteristic angle ~60° with respect to the applied stress direction. 3D observations by X-ray tomography supported that hypothesis showing kinking occurrence only close to the sample free-edge, where the debond angle characteristic for kinking has been reached. 2D numerical simulations of the interfacial crack kinking into the matrix carried out by cohesive zone approach showed that the strength of the matrix affected the position of the crack kinking.

RESUMÉ

Da vindmøller udvikles i stadig voksende størrelse, er det afgørende at opnå vægtbesparelse uden at pålideligheden nedsættes. Pålideligheden af vindmøllevinger kan øges ved at forbedre designregler og de materialemodeller der beskriver materialernes mekaniske egenskaber. Mere pålidelige materialermodeller kan udvikles, hvis viden om mikroskala skade - det første trin i materialesvigt - øges. Derfor er det vigtigt at karakterisere materialernes mikrostrukturer samt initiering og vækst af mikrorevner.

Mikrostrukturen i fiberkompositter, det mest anvendte materiale i vindmøllevinger, har vist sig at have en styrende rolle for de mekaniske egneskaber af fiberkompositter. Derfor har karakterisering af fiber/matrix grænsefladen fået betydelig opmærksomhed i forskningen. Hidtil har de fleste undersøgelser af fiber/matrix -grænsefladen haft fokus på grænsefladen under tværspændinger i retning parallelt med fiberretningen. Fiber/matrix- grænsefladen er blevet karakteriseret i form af en kritisk tværspænding (styrke) eller en Mode II brudenergi. Men for fibre der er vinklet i forhold til den største hovedspændingsretning opstår fiber/matrix debonding under blandet mode (Mode I og Mode II). Debonding under mixed mode har ikke været til genstand for mange undersøgelser. Det er dog velkendt, at brudenergien af grænseflade mellem forskellige materialer afhænger af mode mixity ved revnenspidsen. Det er derfor nødvendigt at karakterisere fiber/matrix debonding ved brudenergien som funktion af mode mixity. Dette kan gøres gennem eksperimentel undersøgelse som skal give pålidelige data som kan benyttes i mikromekaniske modeller til forudsigelse af kompositterne makroskopiske styrke.

Den nuværende ph.d.-studium beskæftiger sig med initiering og udbredelse i mkrorevner glasfiber kompositter med det formål at måle de input parametre, der kræves til mikromekanisk modellering. Specifikt bestemmes brudmekaniske parametre for glasfiber/matrix debonding og revneudbredelse i den omliggende matrix. Der anvendes to forskellige tilgange til karakterisering af debonding, lineære elastisk brudmekanik (LEFM) og kohæsiv zone modellering.

Fiber/matrix debonding blev undersøgt eksperimentelt i 2D og3D i emner bestående af en enkelt fiber indestøbt i matrix udsat for normalspænding på tværs af fiberretningen.

2D in situ observationer ved den frie overflade ved forsøg udført i scanning elektron mikroskop (SEM) blev brugt til måling af debond vinkler og normalåbninger (forskydninger) som funktion af påført trækspænding. Lignende forsøg blev udført ved en synkrotronfacilitet, hvorved debond initiering og vækst blev karakteriseret i 3D ved hjælp af røntgentomografi. Det blev fundet at debonding starter ved den frie overflade og derefter vokser stabilt ind i prøven langs fiberen. Når debond dybde revnen har nået en længde svarende til ca. to fiberdiametre skifter revnevæksten til ustabilt revnevækst (tunneling).

De eksperimentelle data fra test udført i SEM blev brugt til at bestemmelsen af brudenergien af glasfiber/matrix grænsefladen gennem en LEFM model fra litteraturen. Brudenergi for nominel Mode I blev fundet at være ca. 0,2 J/m^2 og ca. 0,4 J/m^2 for henholdsvis "arrest" og vækst af debond revnen. For nominelt Mode II blev de bestemt til at være ca. 2 J/m^2 og ca. 3 J/m^2.

Numerisk modellering af fiber/matrix debonding blev foretaget med kohæsiv zone modellering ved brug af augmented finite element metoden (A-FEM). Modelberegninger kombineret med de eksperimentelle målinger fra forsøg udført i SEM muliggjorde bestemmelse af kohæsiv love parametre for glasfiber/matrix grænsefladen. For den kohæsive lov under Mode I blev styrken bestemt til at ligge i intervallet fra 0,75 til 5 MPa og den kritiske separation blev bestemt til at være mindre end 0,2 μm. Mode I brudenergien for glasfiber/matrix grænsefladen blev bestemt til at være ca. 0,1 J/m^2. Mode II brudenergien blev fundet at være ca. 4 gange højere end Mode I brudenergien. Fra modelresultater blev det fundet, at for det undersøgte parameterområde er initiering og udbredelse af debond revner ikke kun afhængig af brudenergien, men er også følsom over for kohæsive lov parametre (maksimale spænding og kritiske separation).

Initiering og udbredelse af en revne fra debond revnen ud i det omliggende matrixmateriale blev undersøgt gennem et koblet eksperimentelt/model studium. SEM observationer af den frie overflade viste at revnen vokser ud i matrix materialet når debond vinklen får en karakteristisk vinkel (ca. 60°) i forhold til retningen af den påførte spænding. 3D undersøgelserne viste at revneafbøjningen ud i matrixmaterialet kun forekommer kun tæt på den frie kant, hvor den karakteristisk debond vinkel er nået.

Simuleringer af viste, at værdien af matrix materialets styrke påvirker den kritiske vinkel hvor revnen drejer ud i matrixmaterialet.

Contents

1 INTRODUCTION

1.1 MOTIVATION

Trends in wind energy

The general trend observed recently in the wind energy sector is the development of larger wind turbines, mostly for the offshore market. The offshore technology is dominated by large turbines with rotor blades up to ~75m long. The amount of energy harvested from wind resources is expected to grow in the future. In order to increase efficiency of the process, the trend of increasing turbine size is expected to continue as schematically shown in Figure 1.1.

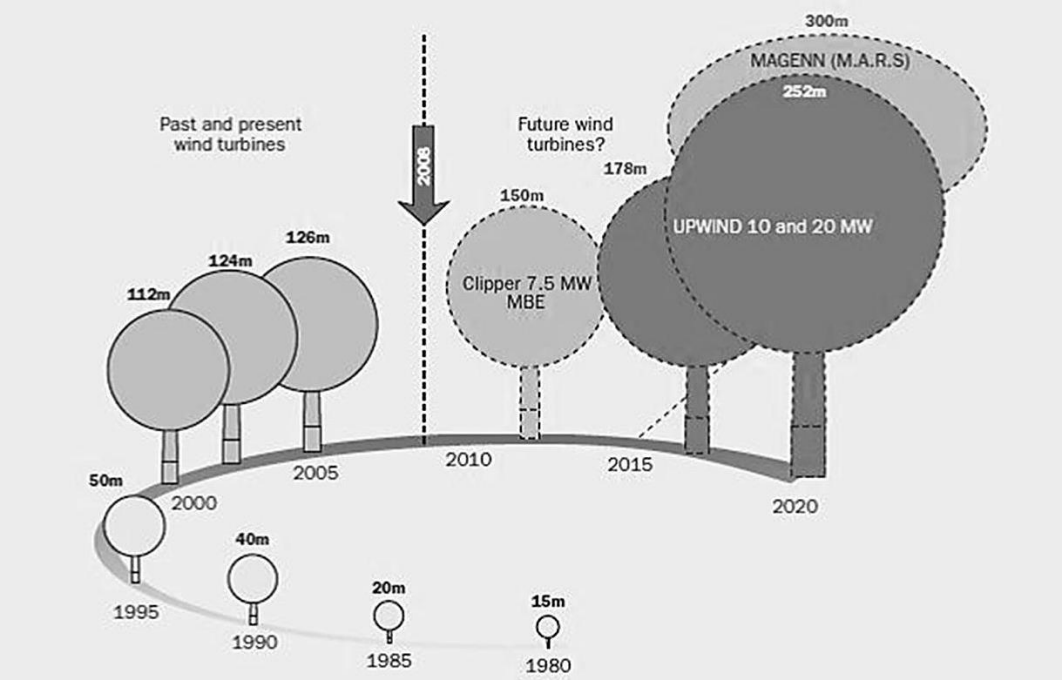

Figure 1.1. An increasing growth in wind turbine size over time [1].

The weight of rotor blades increases with their length, giving a power law with an exponent of ~2.6 [2]. Consequently, the blades of large turbines are subjected to the greater loads which originate from both wind and gravity. Therefore, reducing the weight of the blades is of great importance. It is essential that any weight saving methods do not compromise the reliability of the blades. The reliability of such large

structures can be increased by developing advanced damage-resistant materials, which can be achieved through a good understanding of the damage evolution and crack growth mechanisms.

Placing wind turbines off-shore provides limitations on accessibility and the inspection procedures. A difficult access to the turbines means that manual inspection of the rotor blades (usually the method for identifying damage) is very costly. Therefore, more reliable predictive models of the blade lifetime would be advantageous, so that accurate assessment of the detected damages is possible.

Materials for wind turbine blades

The most critical materials' properties required for a traditional wind turbine blade are low weight, high stiffness and long fatigue life time [2,3]. Such a criteria combination identifies the candidates for rotor blades manufacturing as composite materials [2]. E-glass fibre composites are most widely used, mainly because of their relatively low cost [2,4], and carbon fibres have also been used in a hybrid combination with glass fibres [3]. The glass fibres, which are usually 10-20μm thick, are produced by drawing/spinning of molten glass. The fibre surface are coated with a polymer sizing which protects them against surface damages during handling, as well as improves the bonding between the fibre surface and the matrix [2]. The composites used for wind turbine blades are mainly polymer-based, where typically thermosetting or thermoplastic resins are used as the matrix. Currently, the most common resins used are polyester, epoxy and vinylester [3]. More details about materials used for wind turbine blades manufacturing can be found in [2,3].

Multi-scale approach for composite structures

Due to the complexity of the design and materials used for large wind turbine blades, an understanding of the structural and materials behaviour at different length scales is required [3]. The blade reliability is potentially affected by changes made at any length scale as schematically shown in Figure 1.2. Therefore, a multi-scale approach is required in order to develop more reliable wind turbine blades.

An understanding of the structural behaviour of a wind turbine blade requires understanding of the behaviour of its components, which in fact depends on the material

properties. Composite materials, due to their architecture require an analogue multi-scale approach for detailed characterization. They can be considered at different structural levels including: the molecular level, interaction between fibres and matrix (microlevel), the mesolevel (distribution of the fibres in the matrix, volume fraction, porosity etc.) and the macro level which characterizes the composite as a bulk material.
It was shown that the macroscopic behaviour of a composite depends on the micro-scale properties [5–7]. Therefore, it should be noted that development of advanced damage-resistant materials requires detailed characterization on the small length scales, e.g. on the scale of a single fibre. The concept of this multi-scale approach seems to be appropriate for both experimental investigations and numerical simulations. The experimental characterization of the microscale properties of composites results in the understanding of their macro-scale behaviour. Moreover, micromechanical testing must be conducted in order to provide reliable parameters for micromechanical models which are used in the predictions of the materials macro-scale parameters. Thereby, reliable modelling tools can be developed.

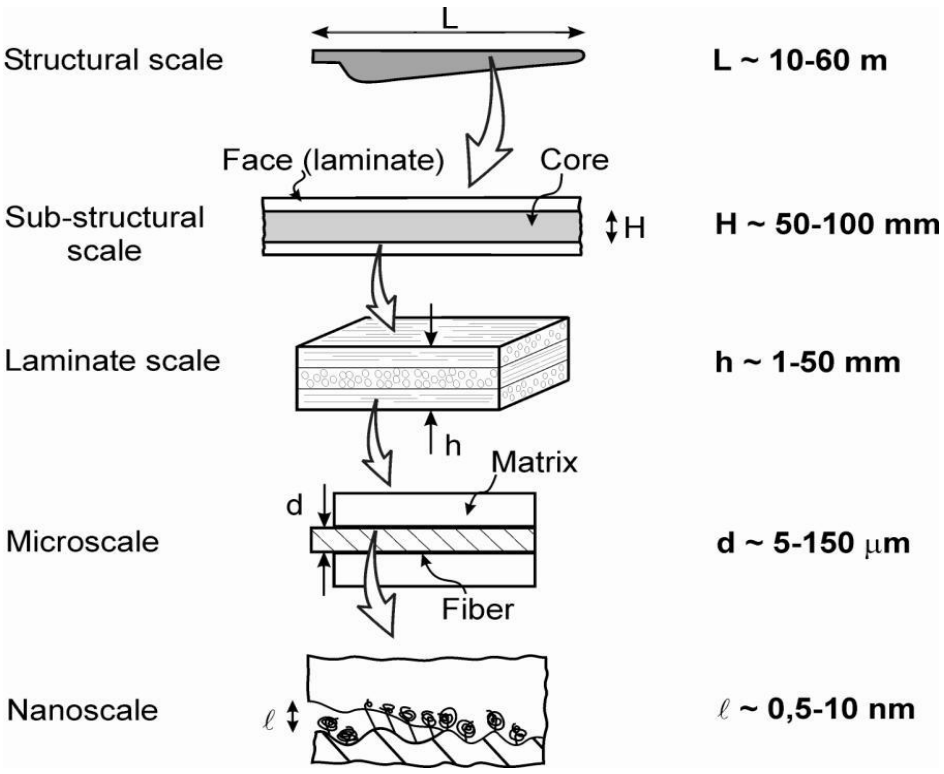

Figure 1.2. Multiscale characterization of wind turbine blade [3].

Microstructure of fibre reinforced composites

The overall behaviour of fibre reinforced composites is controlled by the properties of each constituent, fibres and matrix, and their interaction which is controlled by the fibre/matrix interface [8]. The mechanical properties of the fibres and the matrix can be rather easily determined by standard mechanical testing. Therefore, the properties of these two constituents required for e.g. micromechanical modelling can be easily obtained. Conversely, the fibre/matrix interface properties and the methods for their accurate determination are still a subject to improvements.

1.2 OBJECTIVES

The overall objectives of this study are:

- To investigate the microscale damage in glass fibre composites in relation to the fibre/matrix interface,
- To aid the development of the micromechanical modelling of glass fibres composites by providing input parameters determined from suitable experiments.

The aim of this thesis is to develop suitable experimental methods for the micro-scale characterization of composites with a focus on the fibre/matrix interface. Determination of the interface fracture parameters is addressed by a coupled experimental and numerical approach.

1.3 SCOPE AND LIMITATIONS

Materials systems

The present study concerns micromechanical characterization of fibre composites used for the manufacture of wind turbine blades. Glass-fibre composites were selected, as they are the most common and representative type of composites used in this application. An epoxy resin was selected as the matrix material in this study, as it is widely applied due to its superior chemical resistance, good adhesion, low cure shrinkage and high mechanical strength [4]. The micromechanical characterization is

focused on the fibre/matrix interface whose properties are controlled to some extent by the sizing applied to the surface of the fibres [2]. In this study, only one type of fibre sizing is considered and hence the fibre/matrix interface in all samples studied here is assumed to be alike. Although, the common glass fibres used in the composite manufacturing have a diameter of ~10-20μm [2], thicker fibres with diameter of ~50μm were used in this study in order to facilitate the visual observations of the micro-damage.

Scientific tools

A large volume of literature has been published documenting the methods for determining interface parameters, considering mainly shear stresses along the interface. The methods for determination of the interfacial shear strength, τ_{max} or the fibre/matrix debonding energy for fracture Mode II have been reported and applied in the research [9,10]. However, when multidirectional composites are considered for e.g. wind turbine blades, the shear parameters of the interface are not sufficient for the complete material characterization. The knowledge of a fibre/matrix debonding initiation and propagation due to different loading conditions is very limited.

Recently, a single fibre embedded in an infinite matrix being subjected to a transverse load studied by the Linear Elastic Fracture Mechanics (LEFM) approach was introduced for interface fracture parameters determination [11]. Thereby, fracture parameters of the fibre/matrix bonding as an interface of dissimilar materials were shown to be dependent on the relative contributions of fracture Mode I and Mode II at the crack tip (Mode I: normal opening of the crack faces; Mode II: sliding of the crack faces). Analogue dependency of fracture energy on the mode mixty of the crack tip was found for other interfaces between two dissimilar materials [12,13]. The fracture of the interfaces of dissimilar materials was also studied using cohesive-zone approach (e.g. a fibre/matrix interface [14]), introduced first by Dugdale in the 1960s [15]. In the present work the fibre/matrix interface will be studied applying both: the LEFM and the cohesive-zone approaches.

Moreover, the research related to a fibre/matrix debonding initiation and evolution has been extended and the subsequent interfacial crack kinking out of the interface into the

matrix has been studied [11]. In this thesis both problems are studied: the fibre/matrix interface debonding initiation and propagation as well as the interfacial kinking into the matrix applying the LEFM and the cohesive-zone approach. Only the initiation of a crack kinking is considered here and the further propagation into the matrix is out of the scope of this thesis.

Experimental work

Experimental observations of the fibre/matrix interface debonding and subsequent crack kinking into the matrix have been carried out. For characterization of the fibre/matrix interface and for determination of the interfacial fracture parameters, a tensile specimen consisting of a matrix with a single fibre oriented perpendicular to the loading direction was tested. A suitable specimen for *in situ* testing was developed and manufactured. Thereby, the *in situ* observations of the interfacial debonding initiation and propagation were possible in 2D and 3D using advanced experimental techniques. Free surface (2D) observations were carried out in the chamber of the scanning electron microscope (SEM) and 3D studies were conducted using X-ray microtomography. The kinking phenomenon is studied experimentally only in 2D, in the SEM experiments.

Numerical methods

A fibre/matrix interface subjected to a transverse load was studied numerically using the LEFM approach [11]. The same approach was applied for numerical studies of interfacial crack kinking phenomenon [11]. In the current work, the experimental measurements are compared with the numerical results obtained by LEFM available in [11]. Moreover, a novel numerical method for composites cracking simulations, an Augmented Finite Element Method (AFEM) [16] was utilized in the cohesive-zone modelling. The numerical modelling includes both the fibre/matrix interface cracking and the interfacial crack kinking into the matrix. Only the initiation of kinking is considered though. Although, the experimental observations deal with both, 2D and 3D studies, the numerical modelling reported in this work is limited to 2D.

1.4 OUTLINE OF THE THESIS

The thesis consists of four chapters. The first presents the motivation and general objective of the work. Chapter two introduces the theoretical background and the state of the art of the characterization of a fibre/matrix interface and the interfacial crack kinking towards the matrix. The experimental and numerical methods for the interface characterization used in this thesis are presented in chapter three. In chapter four the main findings of the work are summarized and compared with results available in the literature. Main conclusions from this thesis are summarized in chapter five. Three scientific papers resulting from the work undertaken during this doctorate project are included in the appendix for reference.

2 BACKGROUND AND RELATED WORK

2.1 COMPOSITE MATERIALS PERFORMANCE AND FIBRE/MATRIX INTERFACE PROPERTIES

The fibre/matrix interface plays a critical role in the load transfer between the matrix and the fibres which controls the performance of the fibre-reinforced composite materials [8]. Therefore, an overall response of the composite material is affected by the fibre/matrix interface properties. In the case of carbon fibre composites, the crack initiation has been shown to be influenced by the fibre/matrix interface properties [5]. In tests which had to initiate cracks in specimens without any externally induced damage (e.g. impact or edge delamination), the macroscopic material properties were highly sensitive to the fibre/matrix interface properties. Elsewhere, it has been shown that e.g. the first micro-failure which leads to a macro-failure in transverse plies of a fibre reinforced composites is the fibre/matrix interface debonding, the subsequent interfacial crack kinks and eventually their coalescence (example in Figure 2.1) [7]. In [6] the shear strength of glass fibre composites was shown to be dependent on the fibre/matrix interface properties which were controlled by the sizing applied on the glass fibres. Canal et al. [17] found that the fracture toughness of composites mainly dependents on the fibre/matrix interface strength and toughness while the matrix properties play a secondary role. The study in [17] is also a classic example of the numerical modelling of the composite behaviour using random fracture parameters of the fibre/matrix interface. This is obviously due to the lack of sources for those parameters.

Based on the examples discussed above, it should be noticed that understanding, characterization and determination of the mechanical and fracture properties of the interface are of high importance for the development of advanced materials and reliable modelling tools.

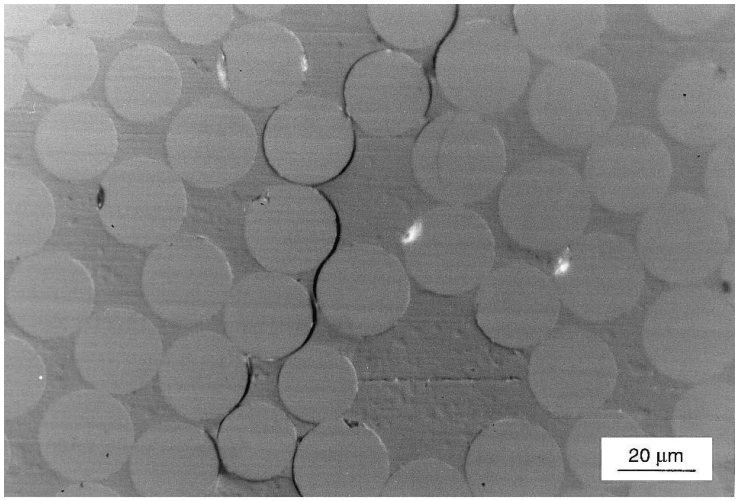

(a)

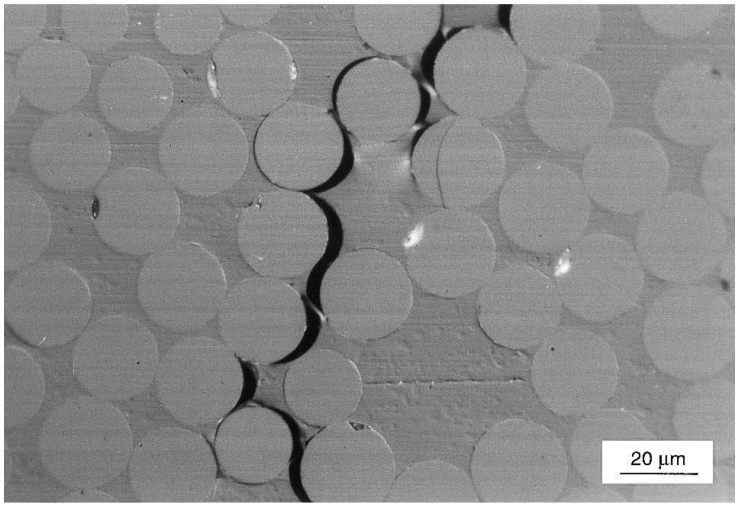

(b)

Figure 2.1. An example of microcracking leading to macrocracking in a transversally loaded ply of the composite materials [7]; (a) fibre/matrix debondings and and their kinking into the matrix, (b) propagation of the coalesced cracks.

2.2 FRACTURE MECHANICS OF A FIBRE/MATRIX INTERFACE: THEORETICAL BACKGROUND

A fibre/matrix interface is essentially one of the constituents of fibre reinforced composites. The characterization of the fracture of such interface can be therefore based on different criteria which are in principle related to the materials strength criteria. Therefore, in the following a brief introduction to the materials strength analysis is

given. Subsequently, an introduction to the fracture mechanics of the interface of dissimilar materials is given with the intention to provide the theoretical background related to the appended papers.

2.2.1 Strength of materials

The first criterion introduced in the materials strength analysis is the stress criterion proposed by Galileo in 1638 [18]. The criterion is applicable for ductile materials. In the case of brittle materials, the application of the stress criterion results in a large scatter in the strength values.

In 1921 Griffith formulated an energy-based crack growth criterion [19]: crack growth will occur only if the released potential energy per cracked area is larger than or equals the energy needed for crack growth (the so called fracture energy, denoted as G_c). This indicates, that if the energy release rate reaches a critical energy (the fracture energy), the crack growth will occur.

During the Second World War, George R. Irwin became interested in the fracture of steel penetrated by ammunition. His work led in 1957 to the development of fundamentals of linear elastic fracture mechanics [20]. Irwin showed that the stress field near the crack tip could be described mathematically by a so-called *K*-field which is a universal singular stress field dominating near the crack tip. The crucial conditions must be met so the LEFM approach can be applied: the crack tip fracture process zone (FPT) and the plastic zone must be small. With this approach, the critical value of the stress intensity factor, (termed usually as K_c), is then a measure of the materials toughness, i.e. the material can withstand crack tip stress intensities up to K_c. A crack growth criterion based on the critical stress intensity was shown to be equivalent to the Griffith energy balance criterion [21].

Each of the model concepts and fracture criterion (ultimate stress criterion, critical energy release rate and critical stress intensity factor), relates to a material property which is associated with the specific loading conditions [22] (see Figure 2.2).

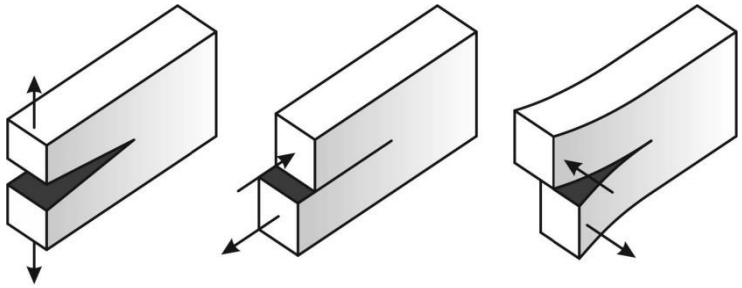

Figure 2.2. Three modes of cracking; from the left to the right: Mode I (opening mode), Mode II (in-plane shear mode) and Mode III (out-of-plane tearing) [22].

In the case of fracture analysis of fibre reinforced composites, the LEFM approach is found not always to be applicable, due to the large-scale process zone which often develops during e.g. delamination of composites [23]. The cohesive-zone approach overcomes this issue and allows for fracture analysis of cracks whose process zone is large compared to the relevant specimen dimensions.

The concept of cohesive stresses, introduced first by Barenblatt [24] and Dugdale [15], can represent several fracture mechanisms typical for composites, e.g. fibre bridging or plasticity. An example of a cohesive law (often called a traction-separation law), is shown in Figure 2.3 [23]. The figure illustrates the physical problem with the development of the fracture process zone ahead of the macroscopic crack (Figure 2.3a), the stress ahead of the main crack tip (Figure 2.3b), and the mathematical representation of the fracture process zone (Figure 2.3c and d). In the cohesive-zone approach the crack is assumed to start to propagate when the stress at the crack tip reaches the cohesive strength, ($\hat{\sigma}_n$ in Figure 2.3d). When the crack growth process occurs, two new surfaces are created. Before complete separation, these two new surfaces are held by the traction forces. The traction is a function of the relative displacement, $\sigma_n = \sigma_n(\delta_n)$, ($\delta_n$ in Figure 2.3d). Therefore, when the crack opens the stress does not fall to zero immediately, but rather decreases as the crack opening increases. The stress falls to zero when the critical opening has been reached (δ_n^0 in Figure 2.3d). The area under the curve of the cohesive law equals the cohesive fracture energy, (Figure 2.3d).

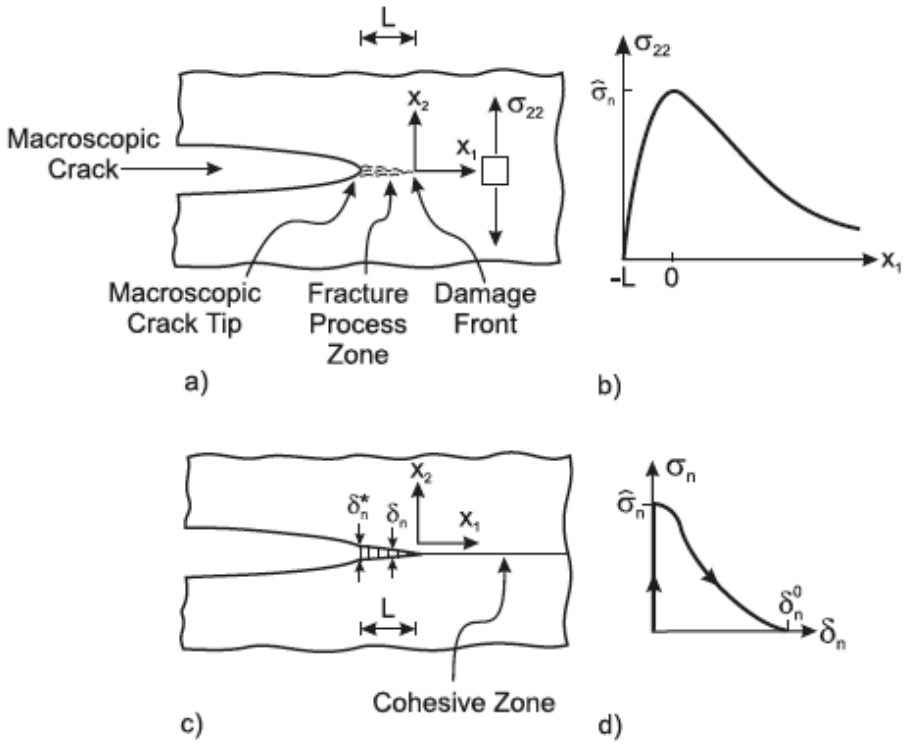

Figure 2.3. Illustration of a cohesive law (traction-separation law) [23].

The cohesive law is usually mode dependent; each fracture mode shown in Figure 2.2 is characterized by a corresponding cohesive law. For analyzing mixed mode conditions (a cracking which involves different modes; an introduction to mode mixity conditions is given in detail in the following section in terms of interfacial cracking), two cohesive-zone approaches are used: an uncoupled and a coupled. In uncoupled cohesive laws the normal stress depends only on the normal opening displacement and it does not depend on the tangential crack opening displacement, and the shear stress depends only on the tangential crack opening displacement [23]. Uncoupled cohesive laws have been widely used in the research [25,26]. In coupled cohesive law, e.g. the one proposed by Tvergaard and Hutchinson [27], the normal and the shear stress both depend on both the normal and the tangential crack opening displacement. This specific coupled cohesive law of Tvergaard and Hutchinson gives the same fracture energy for all mode combinations. In all cases, idealized shapes, either linear softening or a trapezoidal shape are assumed [23].

Recently, the cohesive-zone approach has received a considerable attention in the research. The cohesive law has been shown to be a new material model related to strength and work of separation [23].
A comprehensive description of cohesive laws of materials is given by Sørensen [23].

2.2.2 Fracture mechanics of an interface of dissimilar materials

The analysis of cracking along interfaces between different materials is somewhat more complicated than cracking in homogenous, isotropic solids. While the latter ones crack usually under pure Mode I [12], the interfacial cracking occurs under a combination of fracture modes (shown in Figure 2.2), called mixed mode cracking [12]. Due to the elastic mismatch, the crack of the interface through joined solids (schematically shown in Figure 2.4), is not free to evolve in pure Mode I as it would be in an isotropic brittle solid.

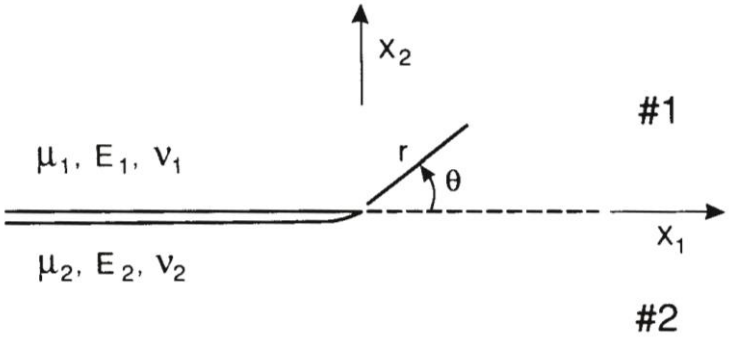

Figure 2.4. Geometry for the interface crack.

The elastic mismatch of the interface bonding two dissimilar materials, can be characterized by the two dimensionless Dundurs parameters [28]:

$$\alpha = \frac{\mu_1(\kappa_2+1) \quad \mu_2(\kappa_1+1)}{\mu_1(\kappa_2+1)+\mu_2(\kappa_1+1)} = \frac{\bar{E}_1 - \bar{E}_2}{\bar{E}_1 + \bar{E}_2} \qquad (1)$$

$$\beta = \frac{\mu_1(\kappa_2-1)-\mu_2(\kappa_1-1)}{\mu_1(\kappa_2+1)+\mu_2(\kappa_1+1)} \qquad (2)$$

where μ_i, E_i, and ν_i ($i=1,2$) are shear modulus, Young modulus, and Poisson's ratio of the respective materials, and κ_i is the Kolosov's constant: $\kappa_i = 3-4\nu$ for plane strain and $\kappa_i = (3-\nu)/(1+\nu)$ for plane stress, $\bar{E}_i = E/(1-\nu_i^2)$ in plane strain and $\bar{E}_i = E_i$ in plane stress; material #1 and 2# in Figure 2.4 are distinguished by the subscripts in Eq. 1 and 2. α measures the mismatch in the plane tensile modulus across the interface and it approaches +1 when material 1 is extremely stiff in comparison with material 2, and it approaches -1 when material 1 is compliant. β is a measure of the mismatch in the in-plane bulk modulus. Both α and β vanish when there is no mismatch [12,29].

The growth of an interfacial crack is governed by a combination of Mode I and Mode II fracture parameters which is described by the mode mixity, ψ defined as [8]:

$$\psi = \tan^{-1}\left\{ \frac{I_m\{ Kl^{i\varepsilon} \}}{Re\{ Kl^{i\varepsilon} \}} \right\} \tag{3}$$

where $K = K_I + iK_{II}$ is the complex stress intensity factor with real, $Re\{ Kl^{i\varepsilon} \}$, and imaginary, $I_m\{ Kl^{i\varepsilon} \}$, parts of $Kl^{i\varepsilon}$, l is a length scale, and ε is the oscillation index which depends on β according to [31]

$$\varepsilon = \frac{1}{2\pi} \ln\left(\frac{1-\beta}{1+\beta}\right) \tag{4}$$

For Dundurs parameter $\beta = 0$, and thereby $\varepsilon = 0$ the real and the imaginary part of stress intensity factor in Eq. 3, are identified as the stress intensity factors for pure Mode I and Mode II, (K_I and K_{II}) respectively. Therefore, for $\beta = 0$, the mode mixity can be defined as the presence of both normal and shear stresses ahead of an interface crack tip, and the occurrence of both opening and shear displacements on the crack faces behind the crack tip (schematically shown in Figure 2.5.)

For $\beta = 0$ the mode mixity in Eq. 3 corresponds to pure Mode I when $\psi = 0°$ and to pure Mode II when $\psi = 90°$ [31].

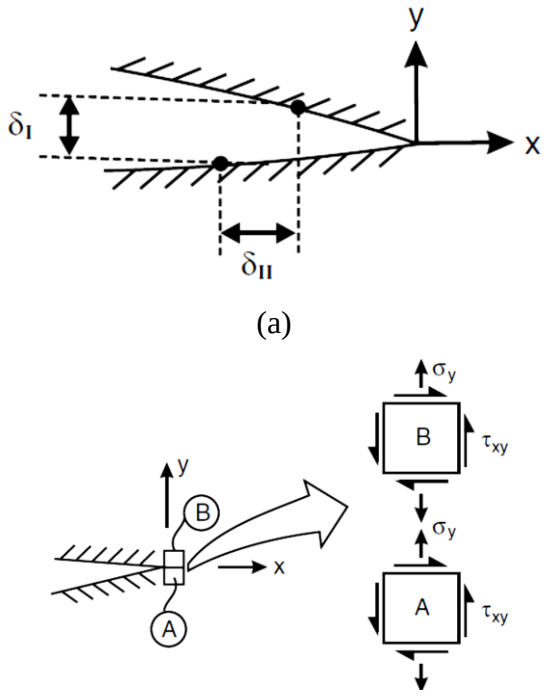

Figure 2.5. Mixed mode conditions of the interfacial crack tip [32], a) the displacements behind the crack tip, b) the stresses ahead of the crack tip.

For $\beta \neq 0$ and equivalently for $\varepsilon \neq 0$, the stress intensity factors, K_I and K_{II} are no longer associated with pure Mode I and Mode II. No separation of fracture modes is possible [12]. Moreover, the oscillatory singularities in the stress field at the interfacial crack tip for $\beta \neq 0$ have been recognized. Comninou [33] introduced the contact model for an interface crack analysis (the model which assumes that the crack faces are in frictionless contact near the tips), which is more realistic than the oscillatory solution.

The fracture energy, G_c as a function of mode mixity, $G_c(\psi)$ of bi-material interfaces was studied experimentally, e.g. by Liechti and Chai, and by Cao and Evans, [34,35]. In both cases a wide range of fracture mode mixities was obtained by varying loading combinations. The fracture energy has been found to increase significantly with an increasing amount of tangential crack opening displacement. Therefore, the fracture

energy of an interface is not a property itself, but rather a function of the mode mixity of the crack tip;

$$G_c = G_c(\psi) \tag{5}$$

Thus, when characterizing an interface of dissimilar materials, the fracture energy must be determined as a function of mode mixity.
Since the fibre/matrix interface is a bonding of a stiff fibre with relatively soft matrix, the mode mixity conditions of the interfacial cracking must be recognized.

2.2.3 Interfacial crack kinking

When analysing cracking along an interface between dissimilar materials, the competition between the crack advancing in the interface and crack kinking out to the adjoining material should be taken into account.
The interfacial crack kinking phenomenon has been studied mainly by an energy-based approach. It was shown that the interfacial cracking path is defined by the relation between the fracture energy of the interface, Γ_i, the material toward which the crack kinks, Γ_s and by the phase angle, $\psi(\alpha,\beta)$ of the interfacial crack tip [36,37]. Trends in the occurrence of interfacial crack kinking reported by Evans et al. [36] show, that the interfacial crack kinking is the most plausible to occur when $\psi = 70°$ and moreover, the crack tends to kink towards the lower modulus material.
More recently, a similar problem of crack deflection at an interface has been studied by the cohesive-zone approach (see Figure 2.6) [38]. Although, the problem is slightly different than the interfacial crack kinking out of the interface (the crack propagates along one of the adjoining materials and then deflects to the interface, Figure 2.6c), some analogy can be noticed. Parmigiani and Thouless [38] studied the role of the interfacial strength, the interfacial toughness, the substrate strength and the substrate toughness, and the relation of all of these parameters on the crack deflection (the problem of the crack deflection is shown in Figure 2.6c). It was shown that the crack propagation path is controlled by the ratio of substrate to interface cohesive strength more than by their toughness.

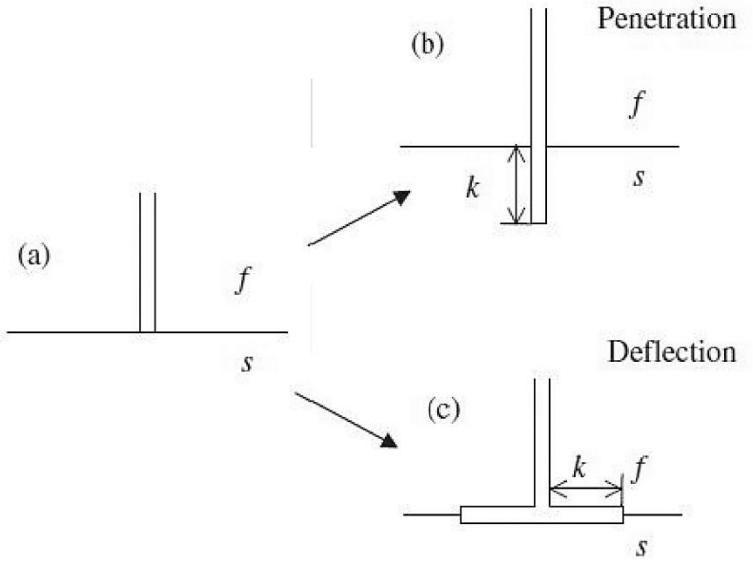

Figure 2.6. The crack deflection problem analyzed by cohesive-zone approach by Parmigiani and Thouless [38].

To summarize, the crack kinking can be thought of as being controlled by relative fracture energy or cohesive strengths of the bonded materials.

2.2.4 Free-edge effect and the interfacial cracking

While the interfacial fracture mechanics introduced in Sec. 2.2.2 deals with the crack propagation, it does not address the associated problem of the debonding initiation at a free-edge. A stress singularity existing at the free surface of bonded materials subjected to external or residual stresses is a well-known phenomenon [39,40]. Therefore, when studying the interfacial debonding, it is expected that due to the complex stress state existing at the free-edge of the material, the debonding is expected to initiate at this location and then will propagate into the material. This implies that the debonding observed at the free-edge might not be representative for the in-bulk behaviour. Therefore, the free-edge effect should be taken into account when characterizing the interface fracture parameters. Thus, the interfacial cracking in the materials should ideally be studied in 3D.

One of the peculiar problems observed in the materials' cracking which is 3D in nature, is steady-state cracking. The steady-state cracking is typically observed in layered materials and is reached when the crack grows long compared with the layer thickness [12]. In this scenario, the crack opening maintains its shape as it advances. In other words the crack propagates with a constant crack width. The phenomena of steady-state crack tunnelling in layered materials is schematically shown in Figure 2.7

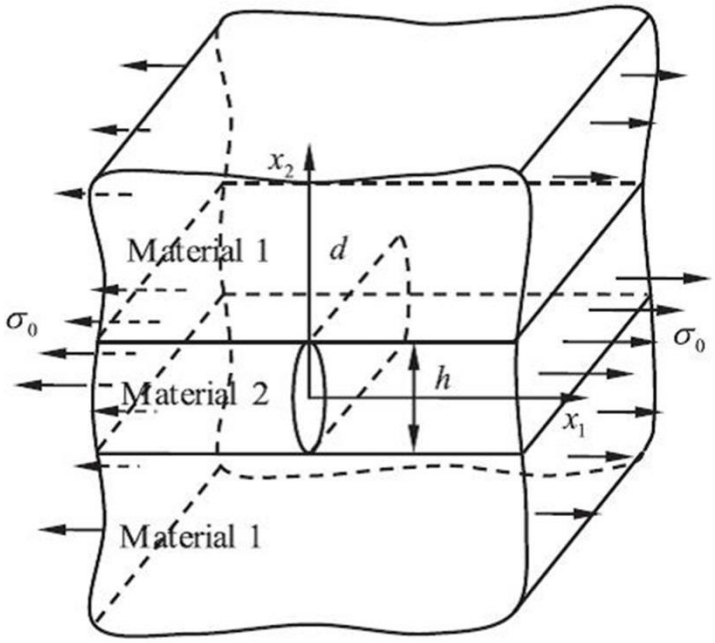

Figure 2.7. Tunnelling crack in layered materials with a tunnel length *d* [41].

Although, the steady state theory has been established for many years, it has been mainly studied by numerical and analytical methods rather than by experimental observations.

2.3 FIBRE/MATRIX INTERFACE FRACTURE PROPERTIES DETERMINATION: STATE OF THE ART

The numerical and the experimental characterization of a fibre/matrix interface fracture properties has been the object of several micromechanical studies. A number of experimental methods have been developed in which an external load is applied directly

to the fibre. Methods like pull out and push out test (Figure 2.8) [42] have been well established and are extensively used in the research for the interface Mode II fracture parameters determination.

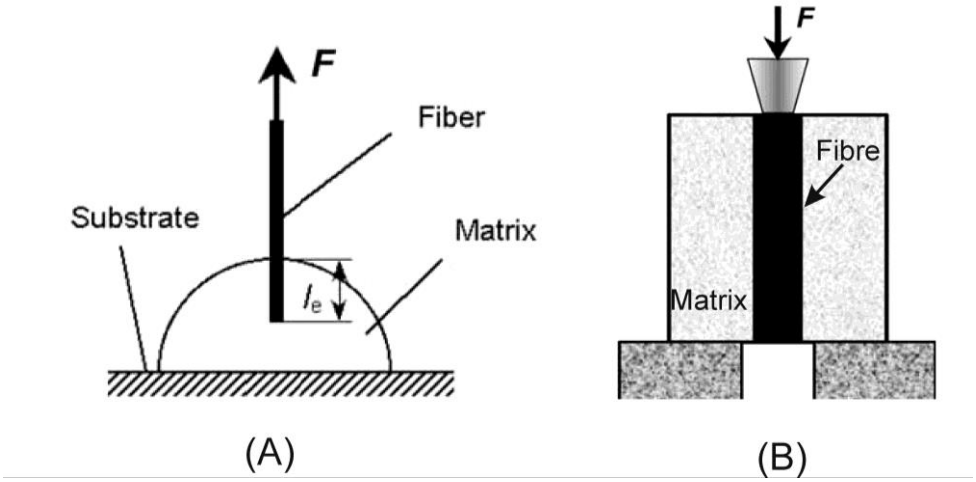

Figure 2.8. Single fibre test methods, (a) pull out, (b) push out [43].

Another group of testing methods for the characterization of the interface parameters includes tests in which the load is applied to the matrix, such as single fibre fragmentation test [44] and Broutman test [45] (Figure 2.9).

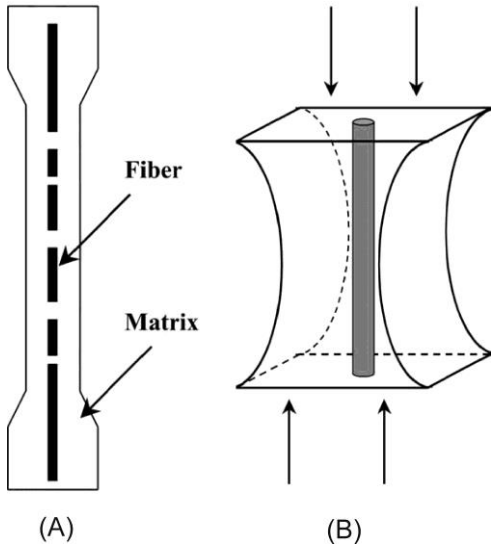

Figure 2.9. Single fibre test methods, (a) fragmentation test, (b) Broutman test [43].

Most of these methods which in fact focus on the interface subjected to shear stresses (except of Broutman test), have been considered convenient for estimating the fibre/matrix interface properties, like the interface shear strength or the Mode II interface fracture energy. There are many discussions however, regarding the reliability of all the methods whose results are often barely comparable. Nevertheless, the issue of reliability of these testing methods is out of the scope of this thesis.

The most traditional characterization of a fibre/matrix interface is the determination of the ultimate shear strength. By the micro-bond method (a kind of pull out test method described in [46]), for the E-glass fibre-epoxy system this strength was found to be $\tau \sim 33MPa$ [46]. The interface shear strength determined by applying a single fibre pull out test for the same material system was found by Chua and Piggott [47] to be in the range of 9-14MPa depending on the curing procedure. The value for the Mode II fracture energy for the same kind of the interface, determined by the same testing method varied from 140J/m^2 to 300 J/m^2 [48]. Analysing the same test method, Hampe and Marotzke [47] determined an interface Mode II fracture energy for the glass fibre/polycarbonate matrix to be in the range of 70-130 J/m^2. The single fibre fragmentation test in [49] resulted in the Mode II fracture energy of a glass fibre/matrix interface being the in the range of 60-230J/m^2 depending on the fibre /matrix bonding quality.

All testing methods discussed above are designed for the characterisation of the interfacial properties in terms of the interfacial shear strength or a Mode II interface fracture energy. There are very few reported attempts where a single fibre specimen is subjected to a transverse load and thereby e.g. a normal strength of a fibre/matrix interface is estimated. One of them is the Broutman test mentioned before and illustrated in Figure 2.9b which coupled together with numerical simulations revealed the normal strength of the glass fibre/matrix to be in the range of 10-13MPa.

With regards to the mode mixity conditions of the interfacial crack tip described in Sec.2.2.2, it is noted that these techniques do not provide means for determination of all the parameters required for a complete interface characterization. Therefore, more recently the interfacial fracture energy was considered as a function of mode mixity of

the interfacial crack tip, $G_c = G_c(\psi)$. A single fibre specimen subjected to a transverse load was introduced in the research (Figure 2.10).

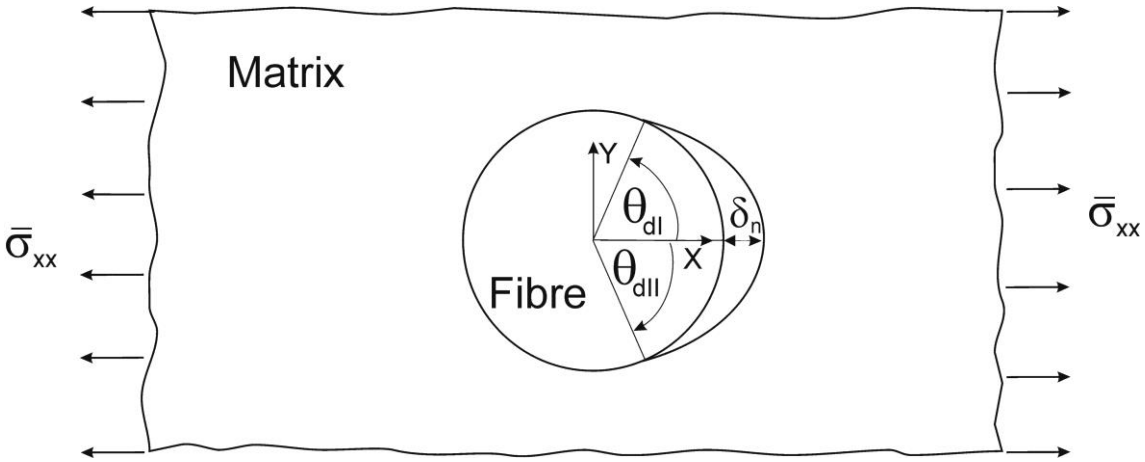

Figure 2.10. A single fibre under transverse load.

By studying a fibre/matrix interface debonding initiation and propagation in a single fibre specimen subjected to a transverse load, the whole range of mode mixity, i.e. from nominal Mode I ($\psi = 0°$) to nominal Mode II ($\psi = 90°$) can be studied. In Figure 2.10 it can be seen, that the mode mixity of the interfacial crack tip changes with debonding angle, θ_d, from dominant normal opening (Mode I) at $\theta_d = 0°$ and $\theta_d = 180°$ with respect to the applied load, approaching tangential-dominant opening (Mode II) at $\theta_d = 90°$. It can be therefore recognized that in case of a single fibre under transverse load, the mode mixity, ψ evolves with the debond angle, $\psi = \psi(\theta_d)$, (see Figure 2.10). Since the fracture energy of the interfacial crack tip depends on the mode mixity, $G_c = G_c(\psi)$ as discussed before, the fracture energy of the debond crack tip in Figure 2.10 also varies with the debond angle, $G_c = G_c(\theta_d)$.

Numerically, the energy release rate and the mode mixity were found as functions of the debond angle for both tensile and compression loads applied transversally to the fibre direction, $G = f(\theta_d)$, $\psi = \psi(\theta_d)$, applying the LEFM approach [11]. For the tensile load, the results reveal an unstable debonding from $\theta_d = 0°$ up to $\theta_d = 60° - 70°$,

followed by a stable crack evolution under Mode II or an interfacial crack kinking towards the matrix. The damage sequence obtained in the numerical predictions by París et al. [11] is shown in Figure 2.11.

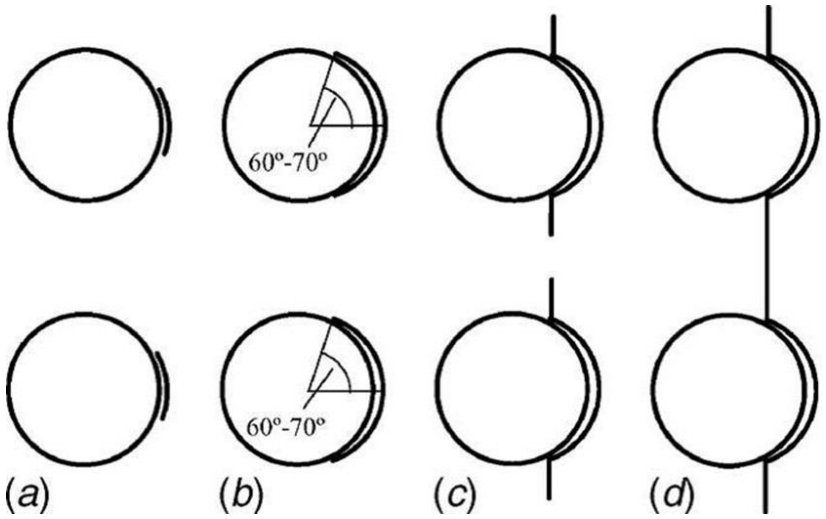

Figure 2.11. Damage sequence in the microscale of the composite subjected to a transverse load predicted by París et al. [11]; (a) a fibre/matrix interface debonding initiation caused by radial stress, (b) unstable debond growth, (c) interfacial crack kinking, and (d) unstable growth of the kinked cracks and their coalescence.

The debond angles obtained from the simulations by París et al. [11] are in good agreement with the experimental observations by Zhang et al. [50]. The experimental results by Zhang et al. [50] were also linked with the numerical predictions by Varna [51] and co-workers. Thereby, the interfacial fracture parameters were determined for both, fracture under nominal Mode I and nominal Mode II (in [50,51] the nominal Mode I is considered for the crack tip at $\theta_d \rightarrow 0°$ and the nominal Mode II for the crack tip at $\theta_d \rightarrow 57°$). The fracture energy of a glass fibre/matrix interface for nominal Mode I was found to be $G_{Ic} = 2J/m^2$ for the fibres without any sizing and $G_{cI} = 10J/m^2$ for the fibres with a sizing. The fracture energy for nominal Mode II was found to be several times higher than for Mode I, $G_{IIc} = 6J/m^2$ and $G_{IIc} = 25J/m^2$ for the fibres without and with sizing respectively. Zhang et al. [50] utilized optical microscopy for

the investigations of a single fibre under transverse load. The debonding observations were carried out using a viewing direction perpendicular to the fibre direction as shown in Figure 2.12 [14,30,52]. This viewing direction allows for the precise debond observations along the fibre but is not well suited for the precise measurement of the debonding angle, θ_d (defined in Figure 2.10).

Figure 2.12. Partially debonded fibre caused by the transverse load (applied in the direction perpendicular to the fibre) [7]. The viewing direction parallel to the fibre direction is not suited for the precise debond angle measurements.

2.4 EXPERIMENTAL METHODS

2.4.1 A single fibre specimen for the interface mixed mode fracture energy determination and studies of the interfacial crack kinking phenomenon

As discussed in the previous section, a single fibre specimen subjected to a transverse load can be used for the determination of the fibre/matrix interface fracture energy as a function of mode mixity, $G_c = G_c(\psi)$. It can be obtained by applying Toya's solution.

Toya [53] developed an analytical solution of the energy release rate as a function of the debond angle for a circular inclusion embedded in the infinite solid.
The energy release rate for the interfacial debonding derived by the use of the Irwin's virtual crack closure technique [21] can be written as [11]:

$$G = g * \pi \frac{(1 - \nu_f^2)\bar{\sigma}_{xx}^2 a}{E_f} \qquad (6)$$

where $\bar{\sigma}_{xx}$ is the applied stress, E_f and ν_f are the fibre Young's modulus and the Poission's ratio respectively, a is the fibre radius and $g*$ is a non-dimensional parameter that depends on the debond angle, θ_d and the Dundurs bi-material mismatch parameters, α, β [18, 22],

$$g^* = g^*(\theta_d, \alpha, \beta) \qquad (7)$$

From Eq. (6), the fracture energy of the interface can be calculated from simultaneous measurements of the debond angle and the applied stress.

The mode mixity of the crack tip of the interfacial glass fibre/matrix debonding is available in the literature as a function of the debond angle, $\psi = \psi(\theta_d)$ (e.g. in [11]). Therefore, by linking the experimental measurements of the debond angle, θ_d with the available numerical results for $\psi = \psi(\theta_d)$, the mode mixity for an experimentally measured crack tip can be obtained.

The same test set up of a single fibre specimen subjected to a transverse load shown in Figure 2.10 can be used in studies of interfacial kinking which has been shown to be the first micro-crack leading to the macro-cracks in the transverse plies of the composites. París et al. [11] has shown that the kinking phenomenon is related to the crack tip location (in other words to the interfacial debond angle). The results of the numerical predictions of interfacial crack kinking by París et al. [11] are shown schematically in Figure 2.11.

2.4.2 SEM for *in situ* observations of damage in composite materials

The scanning electron microscopy technique was first invented in 1935 and since then its basic principle has remained the same, whereas the ability has significantly changed over the past years.

Scanning electron microscopy (SEM) employs a focused electron beam to examine an object on a very fine scale [55]. The interaction of the beam electrons with the atoms of the specimen is the physical basis for the SEM imaging. Depending on this interaction, different out coming electrons can be used for the imaging: secondary electrons (SE, low energy electrons ejected from the atoms of the specimen; high resolution can be obtained) or back scattered electrons (BSE, high energy electrons which are beam electrons back-scattered out of the specimen; lower resolution obtained than with SE signals). The SEM is primarily used to study the surface or near surface of the specimen. When comparing with an optical microscopy, the SEM allows for much better spatial resolution of the images as well as for better depth of field. Therefore, SEM has greatly contributed to our understanding of fracture processes of the materials by providing a means of examining fracture surfaces at high resolution.

The specimen should be conductive for SEM imaging, and electrically grounded to prevent accumulation of electrical charge at the surface of the scanned specimen [55]. Therefore, metal objects require little preparation for SEM. Whereas non-conductive specimens, like e.g. polymer based composites tend to charge when scanned by the electron beam. This problem has been overcome, however, by introducing environmental scanning electron microscopes (ESEM) or by coating non-conductive specimen with conductive thin layers like e.g. carbon or gold [55]. Moreover, due to the difference in the energy between SE and BSE, the latter ones are less influenced by the charging and thereby they are more suitable for non-conductive composites imaging. For more details on SEM principles one should refer to a common SEM hand book e.g. [55].

Since the non-conductivity issue has been overcome, SEM has been extensively used in microscale characterization of polymer-based composite materials. In the field of fracture of composites, the technique has been mostly used for characterization of the fracture surfaces of samples which were tested prior to the scanning. More recently, *in situ* fracture testing of composite materials have been carried out in the chamber of the

SEM. Sørensen et al. [56] developed the method for *in situ* fracture toughness measurement in the chamber of SEM. A special loading fixture for a double-cantilever beam (DCB) specimen was designed and allowed for *in situ* observations of the fracture process zone and toughening mechanism along with fracture resistance measurements.

In more advanced *in situ* testing of polymer-based composites in the chamber of SEM a modern deformation measurements technique, Digital Image Correlation (DIC) has been utilized. DIC is a robust experimental technique which allows for real time displacement measurements on the surface of a specimen (or in the interior) which is subjected to an external load [57]. The displacement measurements are based on tracking the distribution of grey scale intensity on the specimen surface in images acquired before and after deformation. Therefore, the application of DIC technique requires a proper speckle pattern on the scanned surface. Since the DIC does not possess an inherent length scale, it can be applied in different length scales including microscale. The accuracy of the correlation between recorded images depends on the quality of the speckle pattern and image resolution. Different speckle patterns for microscale displacements measurements have been proposed and applied in the research [58]. The details of the DIC technique can be found in [57].

For the microscale *in situ* deformation measurements of polymer-based composites studied in the chamber of the SEM several different speckle patterns have been proposed.

At first, it should be noticed that the size of the speckles have to be adjusted to the image magnification and the pixel size of the image [30,32]. The adjustment procedure for the micrographs acquired in the SEM is described in [59]. The methods for pattern application are available in the literature as well, e.g. in [58]. It has been shown that with high resolution images acquired using SEM during *in situ* testing of composites displacements with sub pixel resolution can be obtained. Canal et al. [60] has proposed alumina particles for fibre-reinforced composites testing in SEM. The contrast provided by this speckle pattern was sufficient for DIC measurements. The displacement measurements obtained from DIC were compared with the numerical predictions. DIC was shown to be able to accurately capture the displacement fields throughout the region of interest. Thereby, the technique seems to be promising for displacement

measurements during *in situ* testing of composite materials conducted in a SEM allowing for sub pixel resolution measurements.

2.4.3 X-ray tomography for 3D *in situ* observations of damage in composite materials

The X-rays discovered in the 19th century were at first extensively used in the medical field and life-sciences [61]. Recently, X-ray tomography has received considerable attention as a technique for the materials characterization. A very brief description of the X-ray tomography technique is given in this work, so that the key concepts used further in this thesis are introduced.

In the X-ray tomography scanning, an X-ray beam passes through the specimen. Due to the different attenuation coefficients of different materials, the X-ray image of the sample is a 2D grey scale map in which the grey scale values correspond to the materials X-ray attenuation coefficients [61]. Although several variations of X-ray tomography setups exist, the basic principles of the technique remain the same. The X-rays are sent through the sample which is mounted on a rotating sample stage. The sample stage is rotated with very small increments and a 2D radiograph is acquired at each angle increment. This series of 2D radiographs is then reconstructed to produce a 3D image. Each volumetric pixel (a voxel) of such an image corresponds to the linear X-ray attenuation coefficient at that point [62]. The principle of X-ray tomography scanning is schematically shown in Figure 2.13.

The X-ray scanning can be carried out at the laboratory or a synchrotron facility [61]. At the first ones, the radiation is obtained from the X-ray tubes. The X-ray tubes consist of a filament which acts as a cathode and headed it emits electrons. These electrons are accelerated by an electric field towards an anode. The anode, often made of copper, decelerates the incoming electrons, where the energy is released. The X-rays beam obtained from the lab source has low intensity and is not parallel [61].

A synchrotron facility consists of a large circular ring, in which electrons are accelerated nearly to the speed of the light [61]. The synchrotron radiation results from the bending of electron beam by the magnetic field [62]. The X-ray beam is parallel and

narrow and it has higher intensity than a beam obtained from the X-ray tubes. Therefore, by far the best results are obtained using X-ray beams produced by synchrotron emitters.

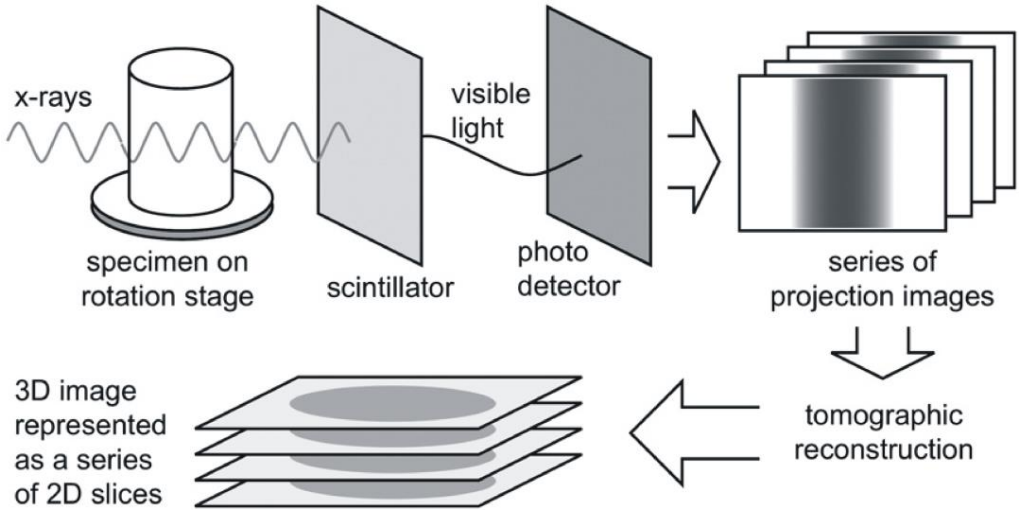

Figure 2.13. Schematic illustration of X-ray tomography data acquisition and reconstruction procedure [62].

X-ray tomography has previously been successfully applied to a variety of 3D studies of fracture of composites. As an example, Wright et al. [63] studied the damage onset and growth in carbon fibre-epoxy composite samples loaded in uniaxial tension by means of X-ray tomography. Experimentally measured crack opening displacements obtained from X-ray *in situ* testing allowed subsequently the numerical model to be validated for the loading conditions of interest. Schilling with co-workers [64] studied samples with a variety of damage types and geometries. Results demonstrate that the X-ray tomography technique is a powerful tool in the characterization of the internal geometry of voids, matrix cracking and delamination in fibre-reinforced polymer laminates. Rask et al. [65] studied the damage initiation and propagation in natural fibre composites. Three dominating damage mechanisms were identified: interface splitting cracks at the interfaces of bundles of unseparated fibres, matrix shear cracks and fibre failures seen at fibres defects. The experimental set up proposed in [65] is also used in the current work (Figure 2.14).

Recently, X-ray tomography has also been utilized for *in situ* measurements of deformations. Using the same principle for the deformation measurements as the one

presented in the previous section for 2D strain measurements (DIC technique), the 3D deformation measurements can be obtained using X-ray tomography images. The 3D strain measurements can be obtained using as markers either the features of the internal structure of the scanned materials which can be e.g. pores (Toda et al. [66]) or by introducing external markers to the scanned samples as it was done for aluminum deformation measurements proposed by Nielsen et al. [67]. Recently, a similar method for 3D deformations measurements of the laminated carbon/epoxy composite materials has been proposed by Brault et al. [68]. The copper particles were introduced to the composite so that a good contrast of grey level distribution in X-ray tomography images was obtained. Similar method of introducing inclusions to the matrix of the glass-fibre epoxy composite was proposed by Haldrup et al. [69]. The glass particles added to the epoxy of the tested composites gave a sufficient contrast in the tomographic images.

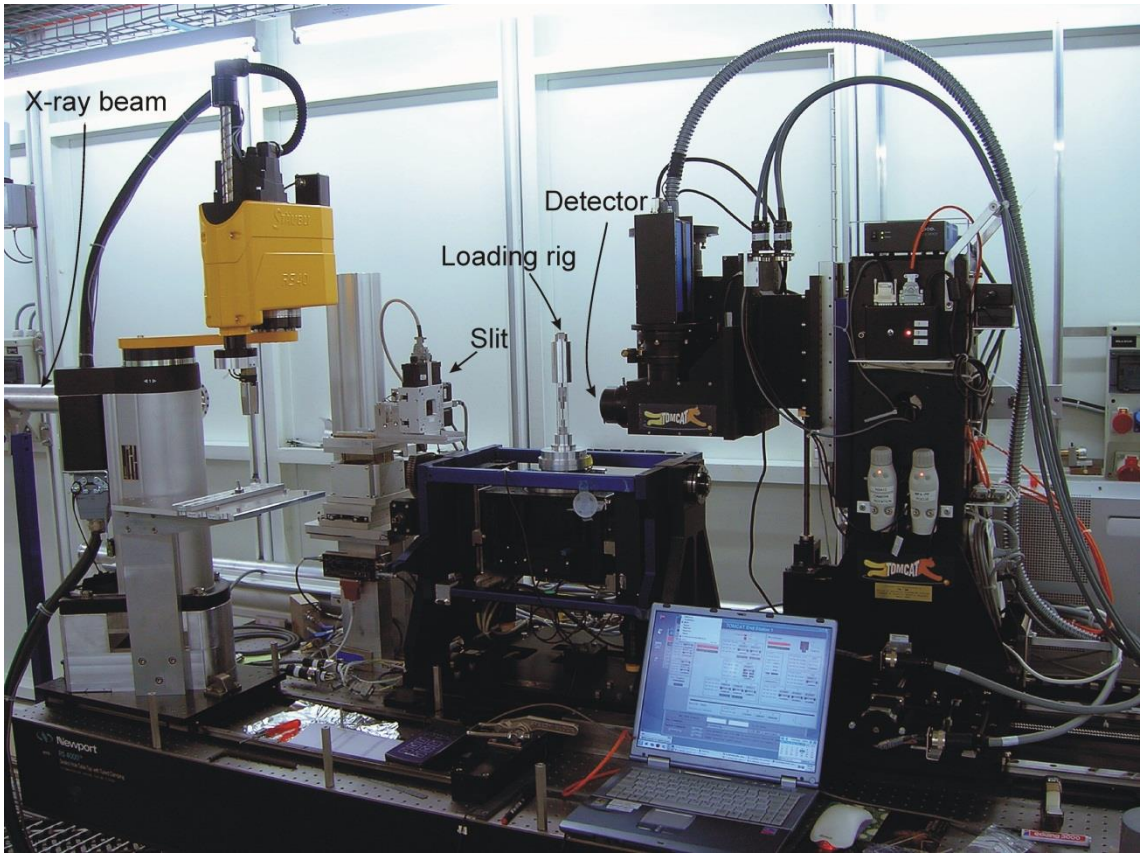

Figure 2.14. Experimental test set up for in situ tensile testing at the SLS synchrotron facility by Rask et al. [65,70]. The same set up was also applied in the current thesis.

2.5 NUMERICAL METHODS: COHESIVE ZONE MODELLING

The concept of cohesive zone was introduced in Sec. 2.1. As described in Sec.2.1, cohesive zone approach is particularly useful when the fracture process zone of a crack is large compared with relevant specimen dimensions; in other words when LEFM is not applicable. In the modelling of the crack whose direction is known in advance due to e.g. the structure of the material as it is e.g. in laminated composites the cohesive zone modelling can be made rather straightforward using cohesive elements implemented in standard commercial finite element (FE) packages. The finite element mesh along the crack path is then replaced with the cohesive zone elements whose damage is described by the cohesive laws discussed in Sec.2.1.

Cohesive zone modelling has been successfully applied in the fracture analysis of composites, particularly in the delamination analysis [71,72]. However, the biggest limitation of cohesive zone modelling is related to the crack path which has to be known in advance.

The promising solution for dealing with the crack propagation without a priori crack path specification is extended finite element method (X-FEM) introduced by Belytschko et al. [73]. However, the analysis of the complex fracture process consisting of multiple cracks (which is often the case when dealing with fracture of composite materials), becomes often challenging and time consuming when using X-FEM. The analysis of the interaction of fibre/matrix debonding and subsequent interfacial crack kinking into the adjoining matrix is computationally heavy and time consuming. Therefore, in the current study, A-FEM which has been shown to be promising tool when dealing with the interactive cohesive cracks was used [16]. The method does not require the crack path specification a priori and allows for efficient and accurate analysis of multiple, intraelemental discontinuities [16].

3 MATERIALS AND METHODS

3.1 A SINGLE FIBRE SPECIMEN MANUFACTURING

In the present work a single fibre specimen was tested. Since the fibre is supposed to be subjected to a transverse load, the sample with the geometry shown in Figure 3.1 was manufactured.

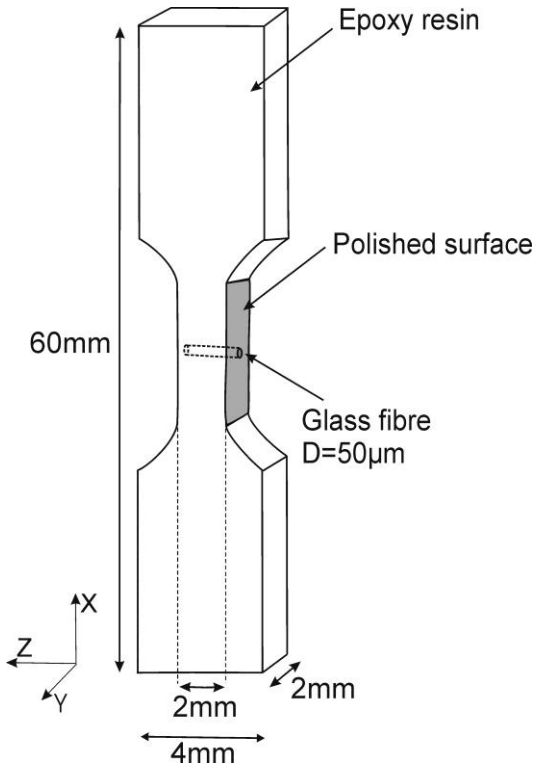

Figure 3.1. Single fibre specimen. The sample is loaded with a tensile force in the *x*-direction.

For the *in situ* observations of the fibre/matrix debonding, an interfacial bonding must have been obtained. Therefore, the residual stresses which arise due to the thermal expansion mismatch between constituent phases and chemical shrinkage of the resin [74,75], must be accounted for. The residual stresses have been shown to have a significant influence on the measured value of the fracture energy of a fibre/matrix

interface as e.g. in [76]. The residual stresses were minimized in the samples by pre-straining the fibres as proposed in [76,77] and so the pre-existing debonds were minimized. An example of such debond observed in a specimen manufactured without fibre pre-straining (and thereby most likely caused by the process-induced stresses) is shown in Figure 3.2.

The samples preparation procedure including the fibres pre-straining and the specimen polishing is described in detail in [A2].

For different testing methods the specimens shown in Figure 3.1 must meet special requirements and they must be adjusted for the loading equipment which was different for different testing techniques. The details of the samples preparation for 2D observations in SEM are given in [A2], and for 3D *in situ* testing using X-ray tomography in [A1].

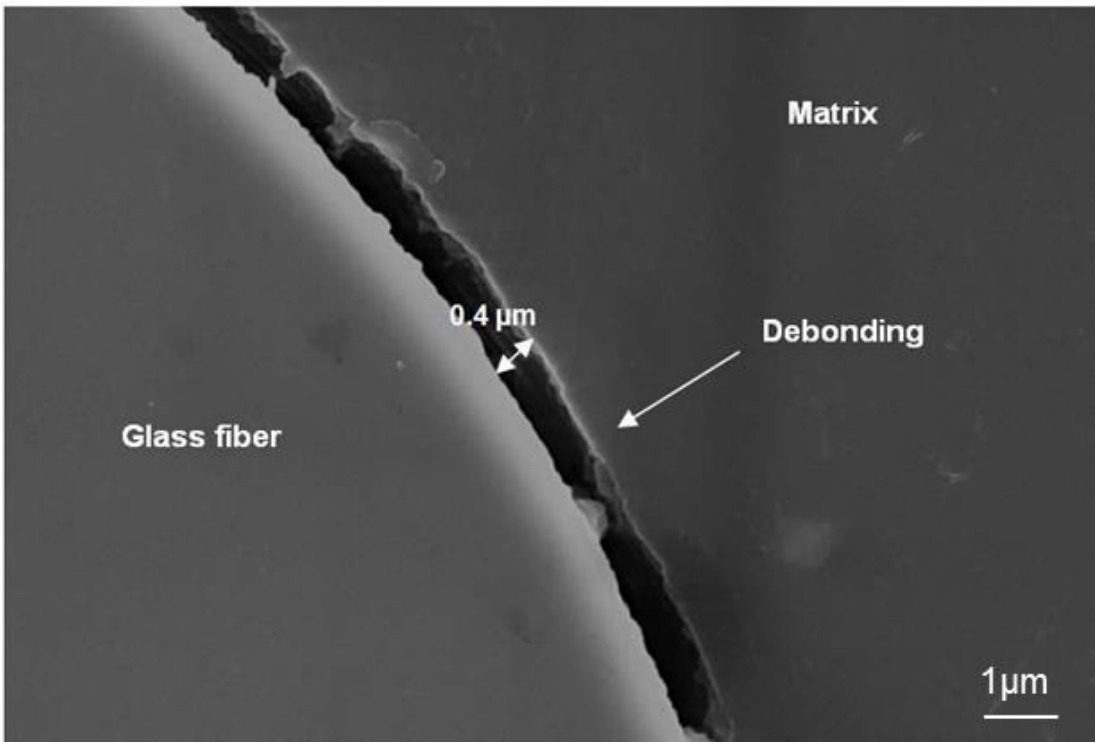

Figure 3.2. Pre-existing fibre/matrix debond observed in the samples. The debond is most likely caused by the residual stresses.

However, some attempts of the sample preparation for 3D strain measurements were made. Since this part of the sample preparation procedure is not included in any appended publication, it is described in the following section.

3.1.1 Specimen fabrication for 3D strain mapping by means of X-ray tomography

For some specimens, marker particles were dispersed in the matrix for 3D strain mapping. Based on the previous studies by Haldrup [78], glass particles were chosen. The composition of the used E-glass particles (type: SCS 350 14) is listed in Table 1.

The glass particles were grinded using a ball mill in order to decrease their size. Subsequently, the particles were sieved so that the desired minimum size of the particles was obtained. The particles size distribution was analyzed using a laser particle size analyzer. A particles diameter distribution is shown in Figure 3.3.

An important issue to consider when using non-native internal markers to measure strain distribution in the sample is the markers influence on the mechanical properties of the material. It was shown by Ochi et al. [79] that for addition of 1% volume fraction small particles, the effects on the elastic properties of the host material are negligible in the elastic regime.

Once the desired particle size distribution was obtained, they were added to the resin and mixed together. Following the results from [79], in all samples, powder was mixed with the resin to produce a volume fraction of ~1%. Subsequently, the resin was degassed in vacuum in order to remove air bubbles. Next the resin was injected into the rubber moulds.

In order to obtain an even distribution of the markers, it was necessary to prevent the particles from sinking due to gravity during the curing process. Therefore, the moulds filled with the resin, were placed in vacuumed bags before curing and were then rotated during the curing process at room temperature. The rest of the sample preparation process was the same as in the case of the samples without glass particles (see appendix [A1]).

Table 1. Composition of E glass particles used for 3D strain mapping.

Element	Content [wt %]
SiO_2	53
CaO, MgO	21
Al_2O_3	13
B_2O_3	11
Na_2O, K_2O	<2

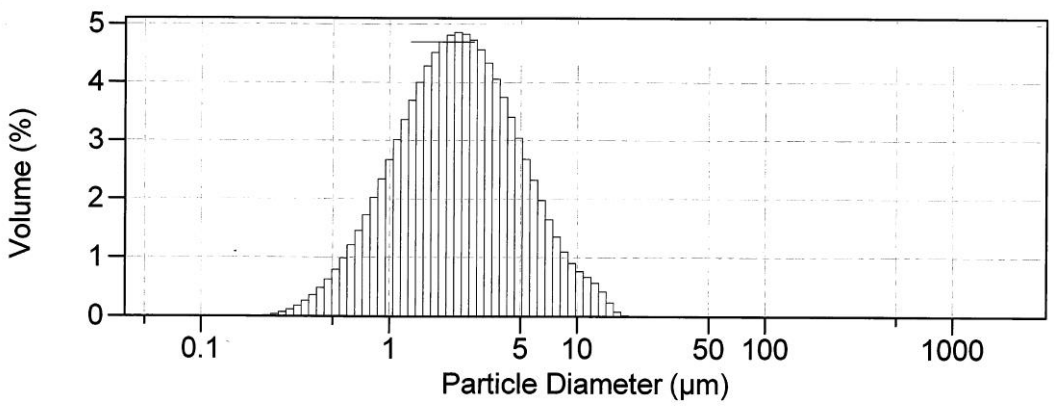

Figure 3.3. The particles size distribution of the glass powder used in the samples for 3D strain mapping.

3.2 EXPERIMENTAL TESTING

The fibre/matrix debonding was investigated experimentally using two techniques which allow for *in situ* fracture observations. These were: SEM and X-ray microtomography for 2D and 3D studies respectively. SEM testing was conducted at the facility at DTU, Risø Campus, Department of Wind Energy and 3D observations were carried out at the synchrotron facility at the TOMCAT beamline of the Swiss Light Source, Switzerland.

For each of the testing methods a special loading device built in house was used (Figure 3.4). In both methods the test set up and the approach was alike: the load was applied

transversally to the fibre direction in increments. In case of tomography tests, in order to allow for high resolution imaging of the fibre/matrix interface, local tomography was utilized (only part of the entire cross section of the sample was scanned). Thus, a volume of 1.5 mm ×1.5 mm ×1.5 mm was scanned. This corresponds to approximately half of the sample thickness in the *z*-direction. The scanned volume is marked with red lines in Figure 3.5.

Moreover, in both cases an acoustic emission (AE) sensor was placed on the sample so any damage initiation or propagation could be potentially detected before it becomes visible in the images. Zhuang et al. [80] have shown that the low amplitude AE events (30-45dB) are generated by the fibre/matrix debonding. Therefore, the threshold of the AE system was set to 30 dB.

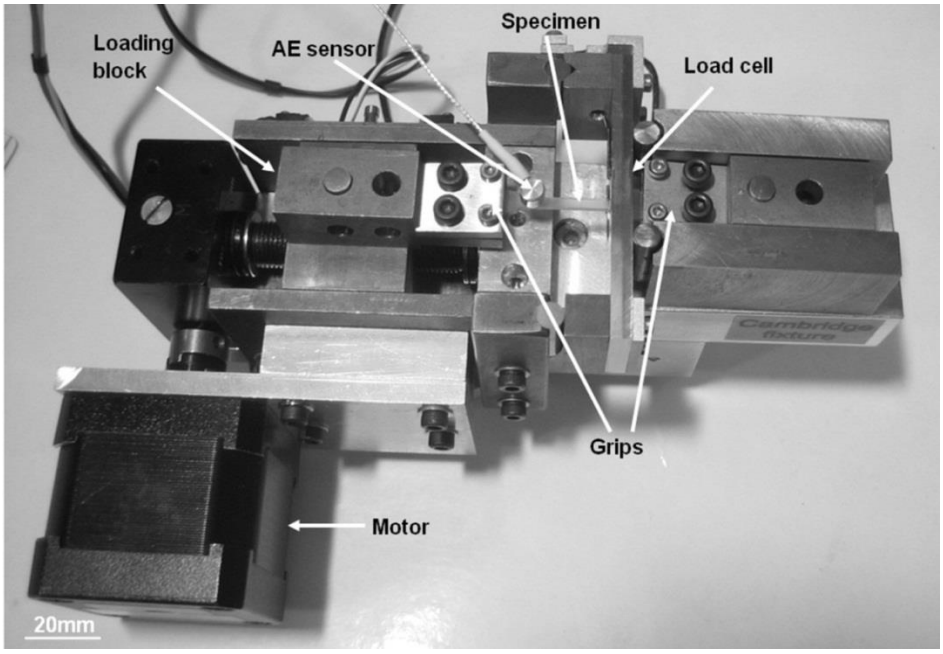

(a)

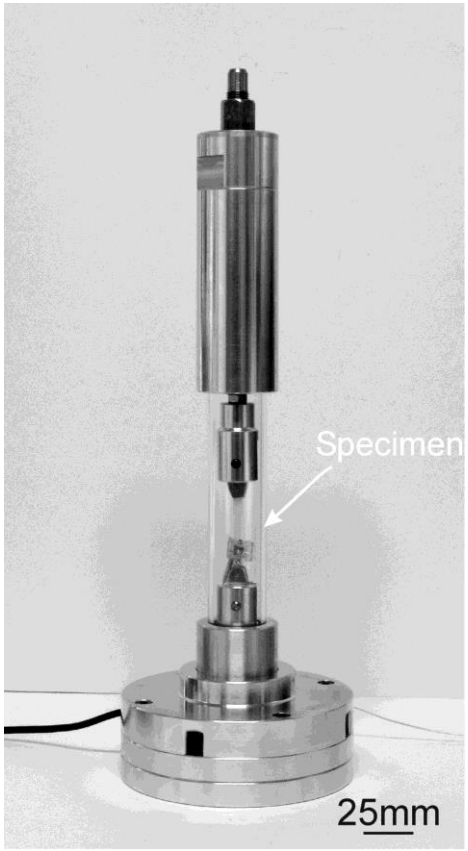

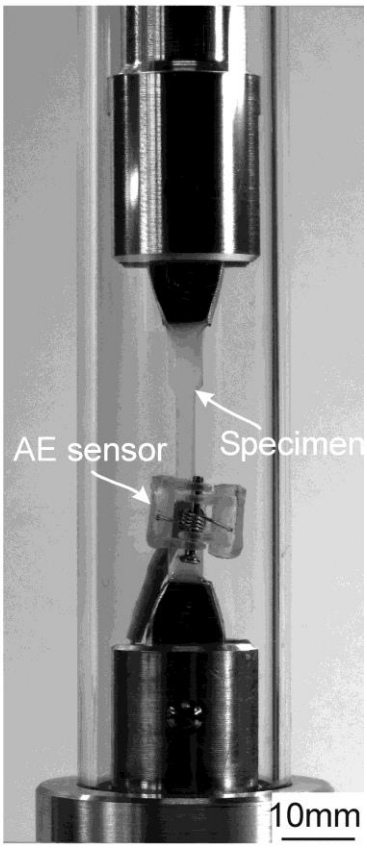

(b)

Figure 3.4. The loading fixture for *in situ* testing (a) in SEM [A2] and (b) at synchrotron facility [A1].

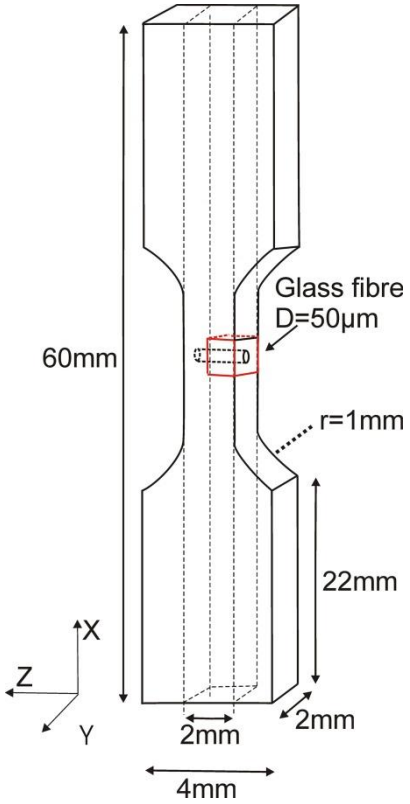

Figure 3.5. The X-ray tomography sample with marked scanned volume.

After each load step the sample was unloaded by ~30% so that any possible material creeping or relaxation during the imaging time was minimized. The step-wise loading is schematically shown in Figure 3.6. The load was measured during the experiments and the fibre/matrix debonds were documented at each load step in the images. Two features of debonds were measured: the debond angle, θ_d and the normal opening, δ_n as defined in Figure 2.10. Moreover, in the case of 3D observations the debond depth, L_d was also measured, and the debond angle and normal openings were measurable not only on the surface but also inside the sample (along the fibre). The features measured in 3D observations are defined in Figure 3.7.

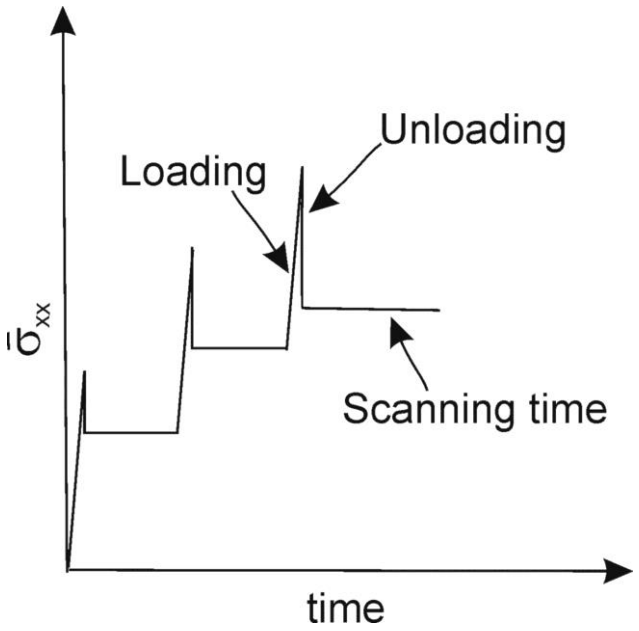

Figure 3.6. Step-wise loading applied in the experiments.

At first the fibre/matrix debonding on the free surface of the samples was investigated in the *in situ* fracture tests which were conducted in the chamber of SEM [A2]. Subsequently, the same problem was studied using X-ray tomography which allows for fracture observations inside the sample [A1].

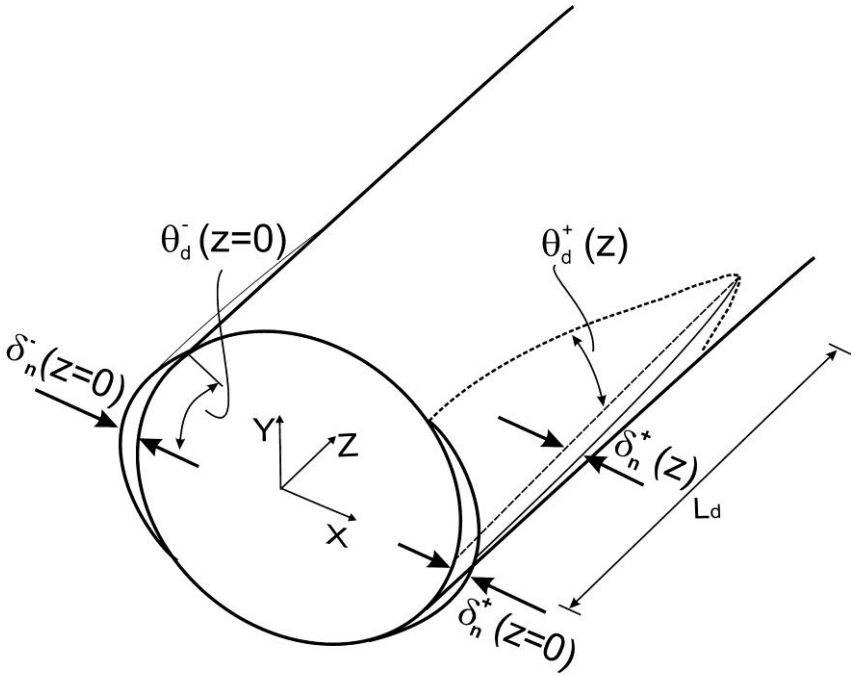

Figure 3.7. Nomenclature used in the 3D debond measurements.

3.3 MICROMECHANICAL MODELLING

Micromechanical modeling was conducted using AFEM [16]. The fibre/matrix debonding initiation and propagation, including the interfacial crack kinking into the matrix was simulated using a cohesive-zone approach. A 2D unit cell, representing the part of the sample tested in experiments (marked in Figure 3.8) was analysed. The domain shown in Figure 3.9a was meshed with 4-nodal, plane strain elements. The same domain was used in several different models: an elastic model, a cohesive-zone model of interfacial debonding and a cohesive-zone model which includes the interfacial crack kinking to the matrix. All details about each of the numerical model are given in [A3].

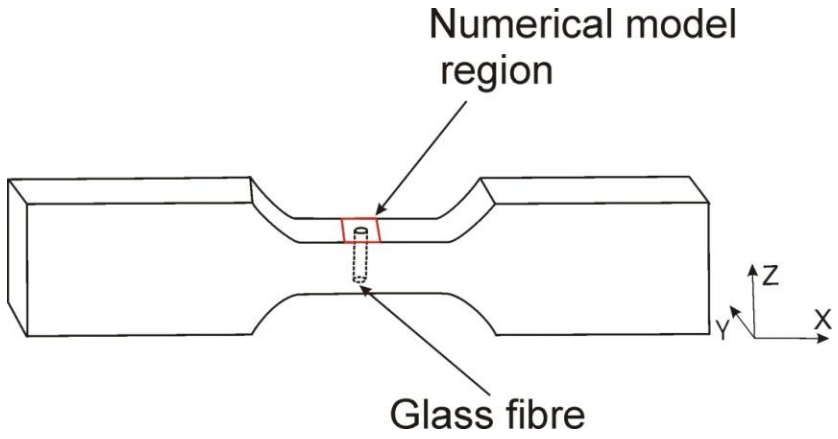

Figure 3.8. Sample tested in the experiments and numerical model region.

For the fibre/matrix interface and the interfacial crack kinking simulations, a mixed mode cohesive law with assumed triangular traction-separation relation for Mode I and Mode II fracture was used (Figure 3.10).

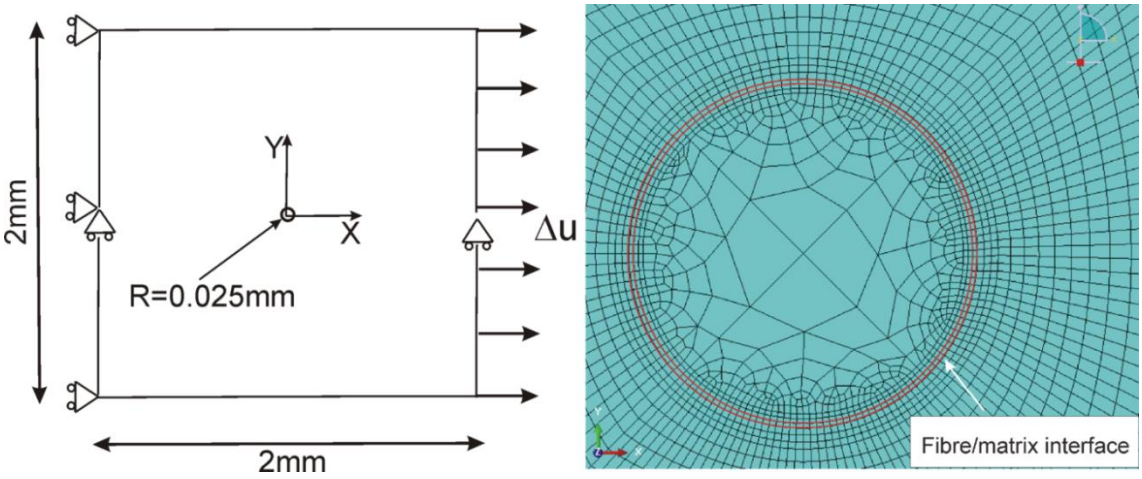

Figure 3.9. A-FEM model: a) model scheme, b) a magnified view of meshed model (the fibre surrounding area); the ring of elements marked in red around the fibre represents the fibre/matrix interface domain.

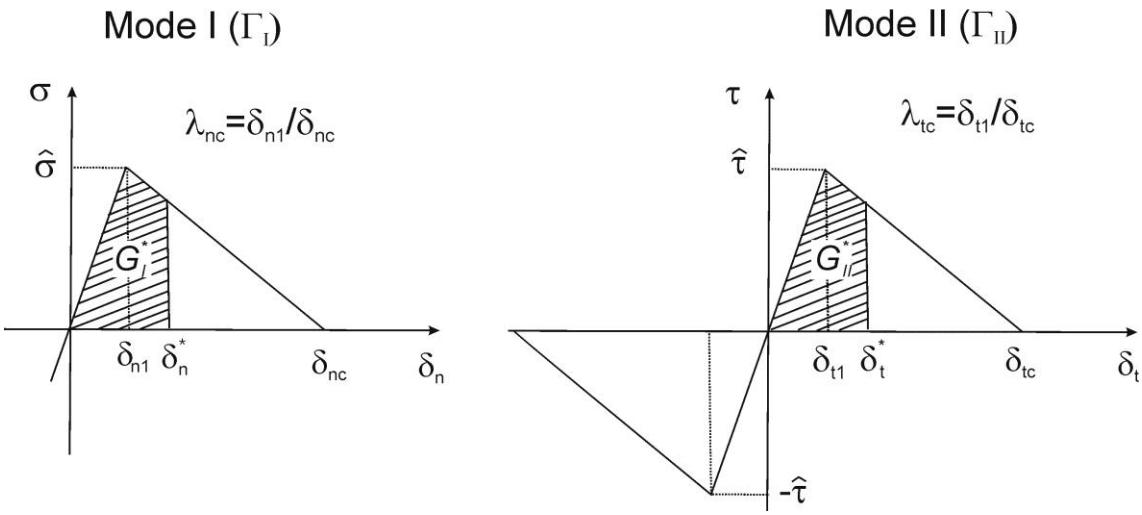

Figure 3.10. Mixed mode cohesive laws used in this study.

Following Yang & Thouless [20], it is recognized that the total traction-separation work absorbed during fracture process, G^*, can be separated into the opening and shear components, G_I^* and G_{II}^* respectively,

$$G^* = G_I^* + G_{II}^* \tag{7}$$

where G_I^* and G_{II}^*, represent the work of the cohesive tractions per unit area which can be calculated by integration of the Mode I and Mode II traction-separation curves shown in Figure 3.10 [20],

$$G_I^* = \int_0^{\delta_n^*} \sigma(\delta_n) d\delta_n \tag{8}$$

$$G_{II}^* = \int_0^{\delta_t^*} \tau(\delta_t) d\delta_t \tag{9}$$

where δ_n, δ_t denote the Mode I and Mode II displacement respectively, σ, τ corresponding to normal and shear cohesive tractions, and δ_n^* and δ_t^* are end-opening and end-sliding of the cohesive zone (see Figure 3.10). The critical normal and shear displacements are denoted as δ_{nc} and δ_{tc}, respectively. The Mode I and Mode II fracture energy can be obtained with $\delta_n^* = \delta_{nc}$ and $\delta_t^* = \delta_{tc}$ as $\Gamma_I = \hat{\sigma}\delta_{nc}/2$ and $\Gamma_{II} = \hat{\tau}\delta_{tc}/2$ respectively.

The opening and shear traction-separation laws are uncoupled and related by a failure criterion [81]:

$$G_I^*/\Gamma_I + G_{II}^*/\Gamma_{II} = 1 \tag{10}$$

where, Γ_I and Γ_{II} are Mode I and Mode II toughness respectively, represented by the total areas given by the traction-separations curves for each mode. The failure criterion in Eq. (10) is required to specify the conditions for separation (failure). In this study it is assumed that a separation occurs when $G_I^*/\Gamma_I + G_{II}^*/\Gamma_{II} > 0.96$.

Once the fibre/matrix interface cohesive laws parameters had been estimated (the procedure of the cohesive law parameters determination will be given in the following

section), the interfacial crack kinking was included in the simulations. Since the whole model was meshed with A-FEM elements, a study of the multiple intra-element discontinuity was possible [16]. The kinking crack simulations required allowing a secondary crack into the matrix when the principle stress in the matrix meets a maximum stress criterion. The same triangular cohesive laws as in Figure 3.10 were assumed for the matrix domain.

3.4 COUPLED EXPERIMENTAL AND NUMERICAL APPROACH FOR THE FIBRE/MATRIX INTERFACE FRACTURE PARAMETERS IDENTIFICATION

A coupled experimental and numerical approach was used for the fibre/matrix interface fracture parameters determination. The free surface debond measurements obtained in SEM testing were used to estimate the interface parameters through the numerical simulations.

The cohesive laws in Figure 3.10 require in total four parameters for the mixed mode fracture process as described in previous section (see Eq. (8) and Eq. (9)). These parameters were determined by a parametric study that compares the results from numerical simulations with the experimental results obtained in the SEM experiments. The parameters which are compared are the debond angles, θ_d and the normal openings, δ_n defined in Figure 2.10.

4 RESULTS AND FINDINGS

In the following sections, the main findings from this study are summarised and compared with the results available in the literature. Sec. 4.1 reports the experimental observations of the fibre/matrix interface debonding initiation and propagation at the free-edge as well as inside the sample. Sec. 4.2 presents results of the fracture energy determination obtained by the LEFM approach, by linking the experimental observations from Sec. 4.1 with the model results available in the literature. Sec. 4.3 deals with the numerical simulations of the fibre/matrix interfacial debonding by the cohesive-zone approach. These model predictions coupled with the experimental observations from Sec. 4.1, led to the mixed mode cohesive law parameters identification (results included in Sec. 4.3). Findings regarding the interfacial kinking phenomenon obtained from experimental and numerical studies are summarized in Sec. 4.4. In Sec. 4.5 complications related to the *in situ* mechanical testing of polymer-based composites by means of X-ray tomography are listed.

4.1 *IN SITU* OBSERVATIONS OF THE FIBRE/MATRIX DEBONDING

4.1.1 Free surface debonding (SEM observations)

As explained in Sec. 2.2.4, the fibre/matrix debonding initiation is most likely to occur at the free-edge of the sample. Therefore, in order to investigate the debonding initiation *in situ*, in Paper [A2] fracture tests are conducted in SEM. The sample surface (presented schematically in Figure 2.10) is observed during loading.

The SEM images of the free surface of the sample were acquired with a magnification of ~1000× which allowed for the viewing the entire fibre with the pixel size of ~128±5nm. Thereby, the damage detection was possible at a very early stage. The interface damage initiation occurred at angle $\theta_d = 0°$ with respect to the applied stress direction (see Figure 2.10 for notation) and propagated unstably along the fibre/matrix interface. An example of the general sequence of the fibre/matrix debonding initiation and propagation is shown in Figure 4.1. In each test the debond angle, θ_d, and the normal opening, δ_n, were measured as a function of the applied stress, $\bar{\sigma}_{xx}$ (Figure 4.2).

It was found that the debonding initiation occurs in the nominal stress range of $\bar{\sigma}_{xx} = 3\text{-}5MPa$ (marked as dashed area in Figure 4.2). The normal opening at the debonding initiation stage reached $\delta_n \sim 0.17\mu m$ and the debonding angle $\theta_d = 50° \pm 15°$.

The unstable debond crack propagation is in good agreement with the numerical model results of París et al. [11], who found that the debonding of an undamaged interface starts at $\theta_d = 0°$ with respect to the applied stress direction. It was assumed that the deboning initiation occurs when the normal stress reaches the tensile strength of the interface at $\theta_d = 0°$. The first debond associated with the damage initiation is predicted to reach $\theta_d = 10°$ (or more), starting from which the interface fracture mechanics is applicable for further crack propagation. Thereby, in [11] the debonding is predicted to initiate at $\theta_d = 0°$ and propagate unstably to the interval of 60°-70° which is in relatively good agreement with experimental observations presented in Figure 4.1 and Figure 4.2.

At the subsequent load steps during SEM testing, the debond crack propagated along the interface (in other words the debond angle became larger). However, at some of the load steps, the debond crack did not propagate (see Figure 4.2a).

Only one to two debond crack propagations/arrests were observed in each sample before crack kinking occurred (more details on crack kinking will be given in Sec. 4.4.).

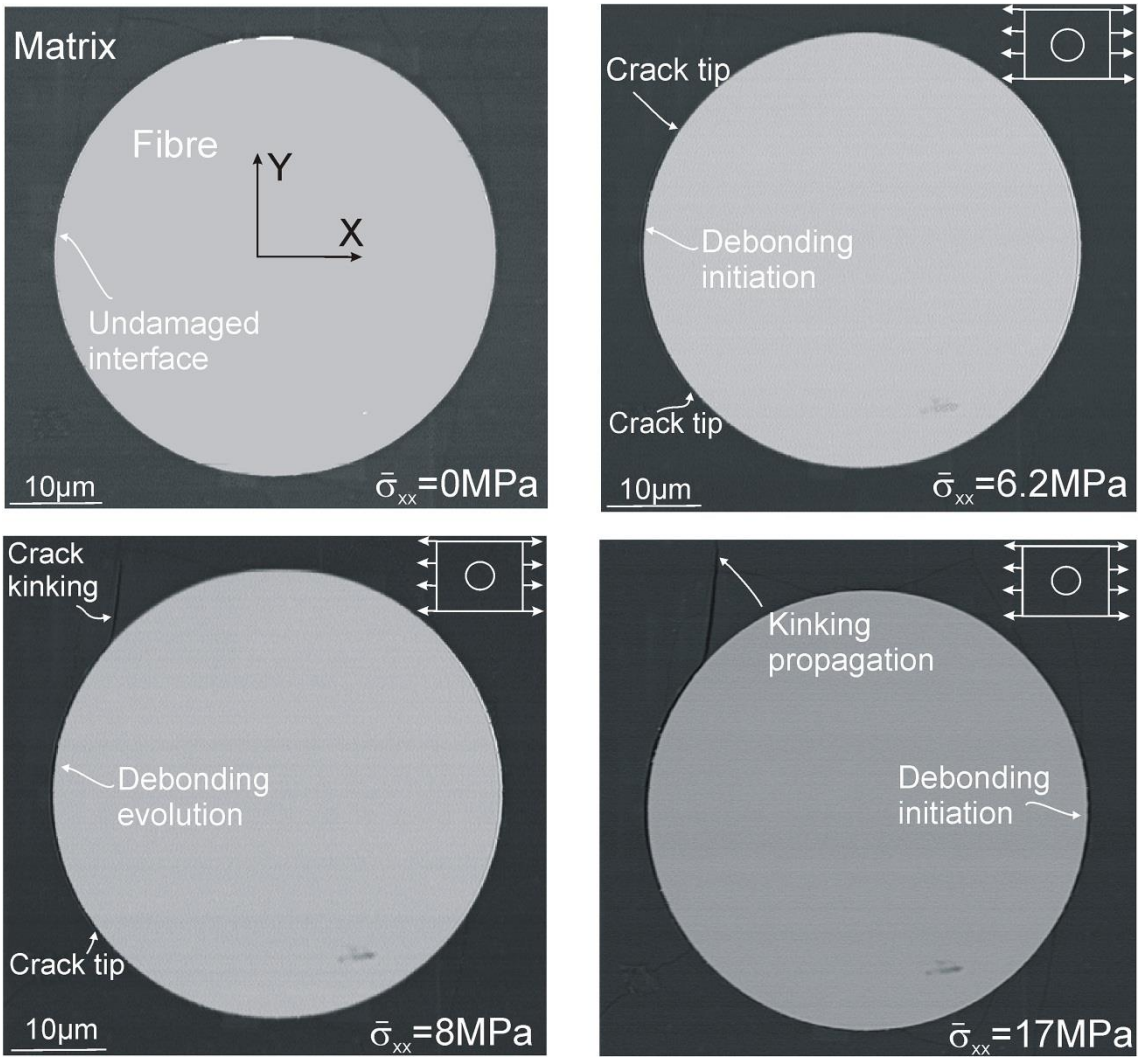

Figure 4.1. *In situ* debonding observed at the free surface of a single fibre specimen under transverse load [A2].

A further load increase caused the further propagation of both the debond crack and the matrix crack, and eventually the debonding initiation on the other side of the fibre (at $\theta_d = 180°$ in Figure 2.10; see example in Figure 4.1).

No fracture process zone was identified in the acquired images. Only in some cases AE activity was detected when the damage initiation/propagation also seen in the SEM micrographs. Otherwise, the damage initiation/propagation visible in the SEM micrographs was not detected by AE system.

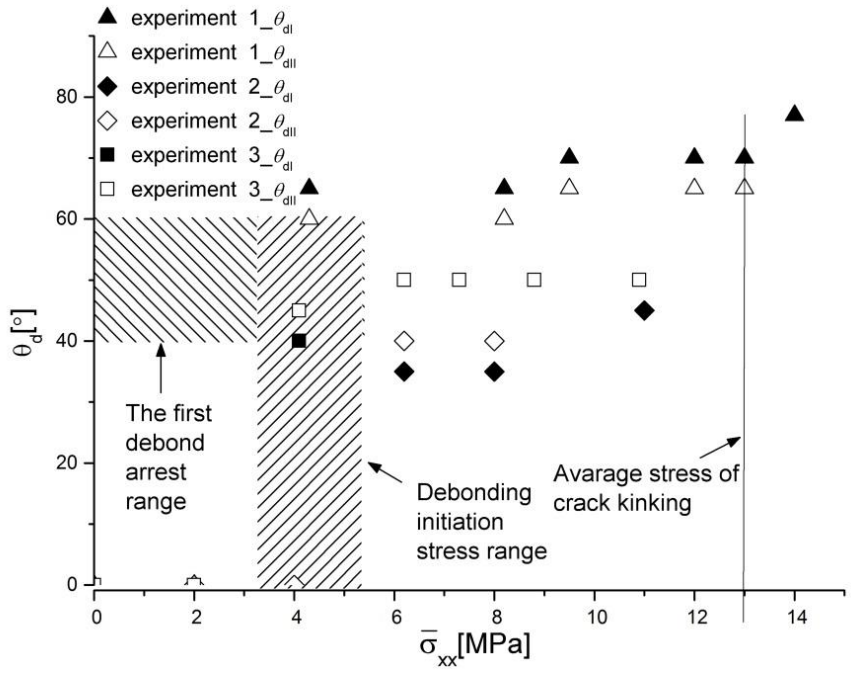

(a)

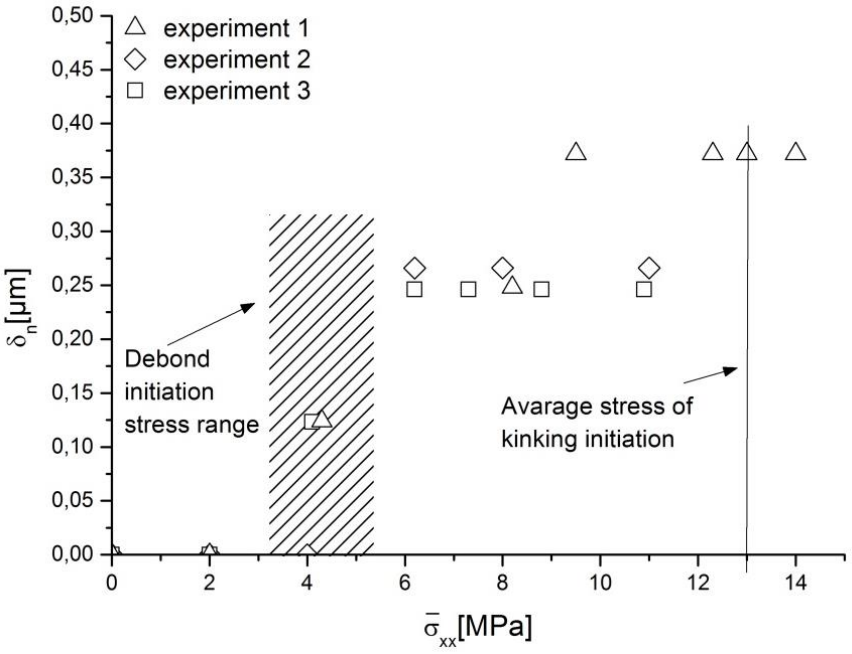

(b)

Figure 4.2. Experimental results for debonds as functions of applied stress: a) debond angle, b) normal opening [A2].

4.1.2 3D debonding (X-ray tomography observations)

As mentioned in the theoretical background, due to the free-edge effect the fibre/matrix debonding is expected to initiate at the free-edge of the sample and then propagate inside the sample. Therefore, in Paper [A1] the debonding mechanism is studied by means of X-ray tomography which allows for 3D observations of the damage and thereby, the free-edge effect can be studied.

In the study in Paper [A1], a spatial resolution of 0.74×0.74×0.74μm^3/voxel was obtained. Due to the high resolution it was possible to distinguish very small features including fibre/matrix debonding.

Based on 3D volumes, 2D slices can be extracted and made in any desired plane. Thereby, the debond crack can be observed at any position inside the sample.

The fibre/matrix debonding was observed to initiate at the free surface and subsequently propagated inside the sample, along the fibre (in *z*-direction in Figure 3.7) as shown in Figure 4.3. The debond angle, $2\theta_d(z)$, (which corresponds to two debond angles measured in SEM observations, $2\times\theta_d$; see notation for tomography results in Figure 3.7) and normal openings, $\delta_n(z)$ can be measured along the fibre (results in details in Paper [A1]). It was observed that, once the debond depth (L_d in Figure 3.7) exceeded ~100μm, an unstable crack propagation occurred along the fibre throughout the entire volume scanned in the experiment. Figure 4.4 shows the transition to the unstable cracking and visible crack front which remained the same after the transition. The transition from stable interfacial crack growth to unstable crack growth is known from cracking of constrained layers as steady-state crack tunnelling [82]. Modelling has shown that for crack tunnelling in plane layers the energy release rate attains a steady-state value after the tunnel length exceeds a few times the layer thickness [82,83]. Since L_d=100μm corresponds to two fibre diameters ($2\times D$), it can be concluded that the observed phenomenon of a curved tunnelling crack is consistent with the theory for straight tunnelling cracks [82]. For further investigation of this phenomenon, a variety of fibres with different diameters could be tested to study the influence of fibre diameter on the energy release rate. It is expected that debonding should occur at a lower applied stress for the thicker fibre diameter, since energy release rate scales linearly with the fibre diameter, (see Eq. 6) [11].

Based on the *in situ* 3D observations, the entire debonding process is schematically shown in Figure 4.5. Figure 4.6 shows the 3D visualisation of the three final load steps including the transition to the unstable cracking along the fibre.

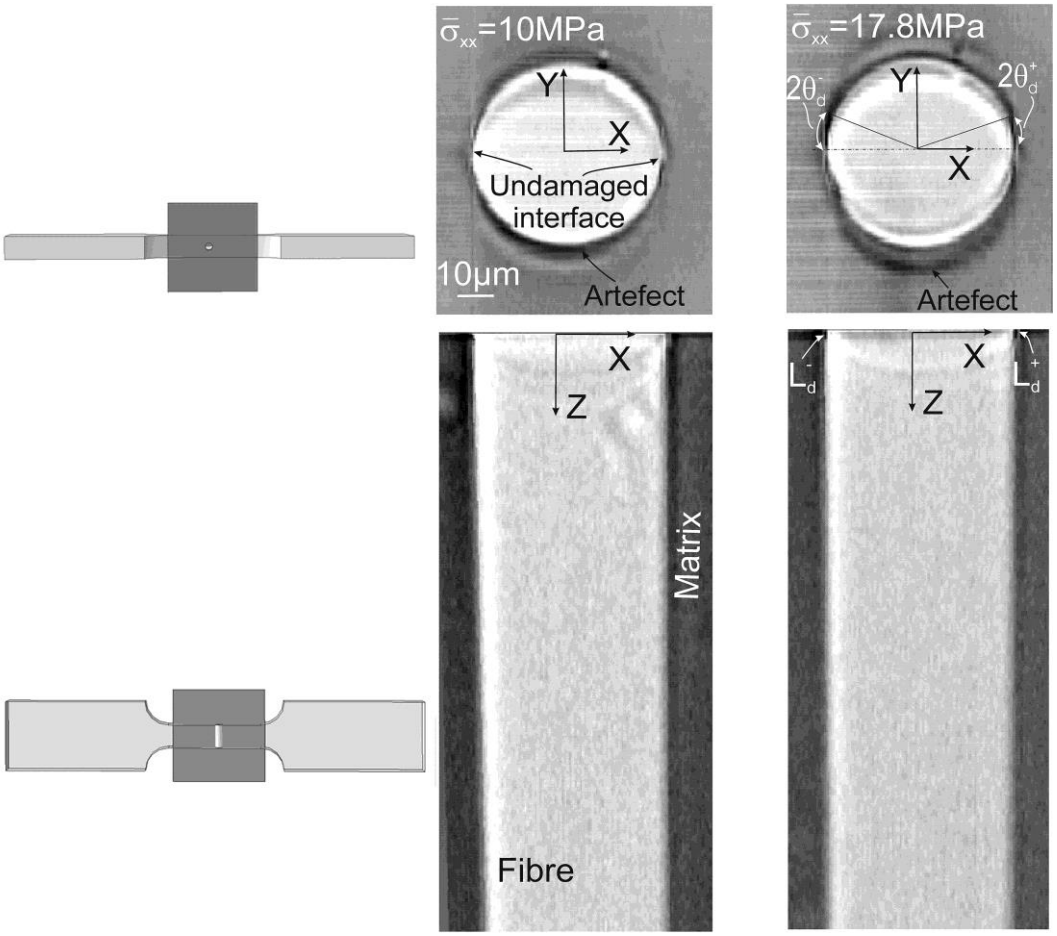

Figure 4.3. Internal *x, z*-plane presenting the fibre/matrix interface debonding at the free surface [A1].

Relatively large amount of research has been reported on the application of X-ray tomography for studying the internal damage and flaws in the polymer-based composites considering them at the mesoscale, meaning including a large number of fibres distributed in the matrix [63,64]. With the present study it has been shown that the technique of X-ray tomography is a very powerful tool not only when considering the mesolevel of composites but also when studying a microlevel (the level of a single fibre) of the damage including e.g. a fibre/matrix interfacial debonding. The ability of the X-ray tomography to provide data for 3D micromechanical modelling has been

documented in the present work. The detailed parameters obtained in Paper [A1] show that the technique is a promising tool to aid the developments of the micromechanical modelling of composites.

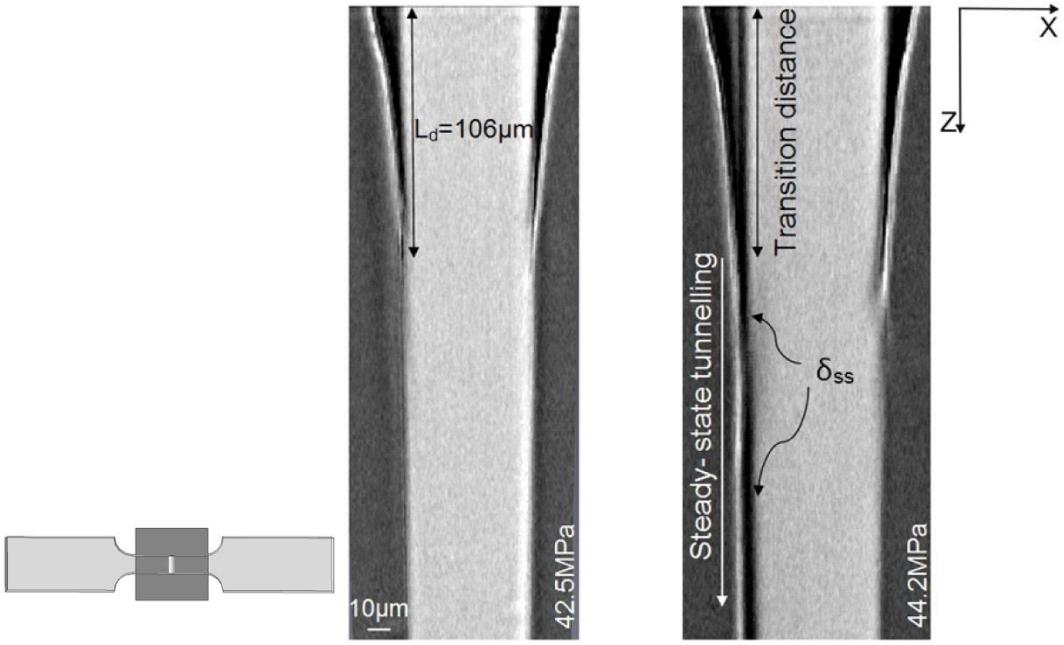

Figure 4.4. Steady-state interfacial crack tunnelling- transition from stable crack growth to steady- state crack tunnelling; *x*, *z*- plane corresponds to the internal plane along $\theta_d = 0° - \theta_d = 180°$ normal to *x*, *y*-plane as indicated in Figure 3.7 [A1].

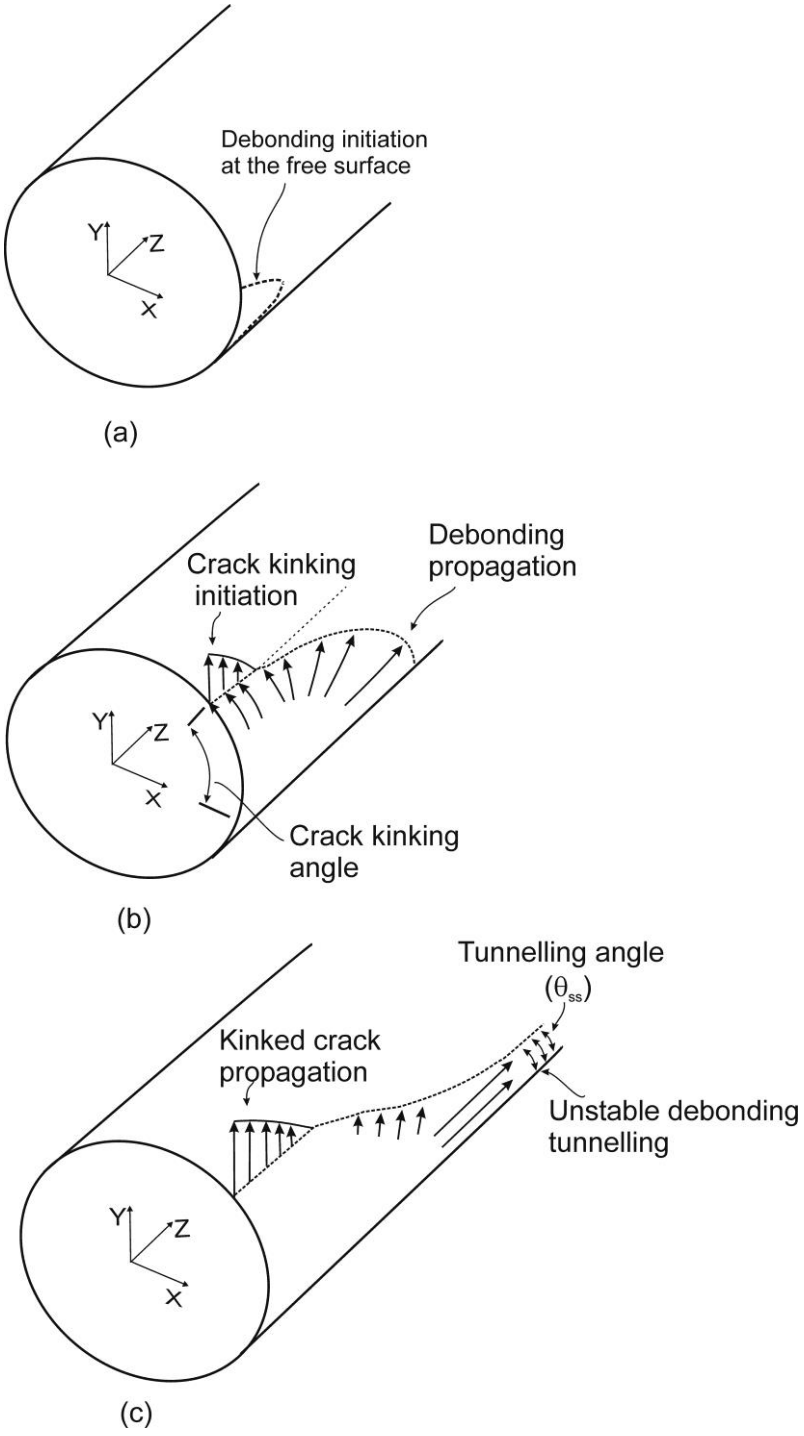

Figure 4.5. Schematics of the 3D debonding propagation observed *in situ* in the tomography tests [A1].

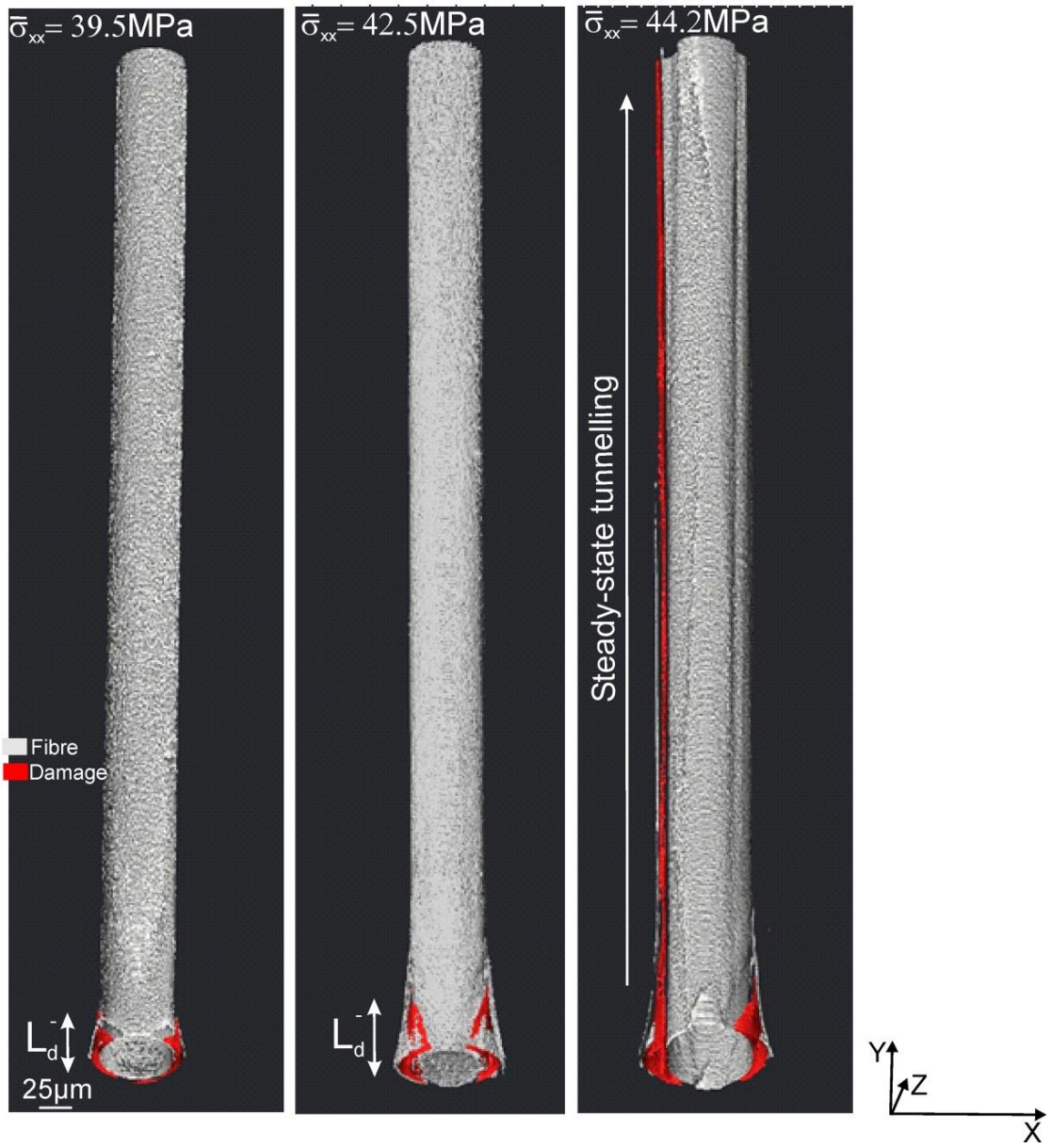

Figure 4.6. 3D visualization of the debonding propagation and the transition to the steady-state tunneling [A1].

4.2 Mixed mode fracture energy of the fibre/matrix interface (LEFM approach)

As illustrated in Figure 2.10 (Sec. 2.3) and described in Sec.2.4.1, a single fibre specimen subjected to a transverse tensile load can be used for the fibre/matrix interface fracture properties determination with the account for the mixed mode conditions at the

interfacial crack tip (by applying the LEFM approach). Therefore, in Paper [A2] the mixed mode fracture energy, $G_c = G_c(\psi)$ of the glass fibre/matrix interface is determined using the experimental measurements from the current study. $G_c = G_c(\psi)$ is obtained by linking the experimental measurements with the numerical predictions available in the literature by París et al. [11]. The procedure is described in detail in Paper [A2].

As mentioned before, the debond angle did not increase at each applied load step (see results in Figure 4.2a). It is therefore appropriate to characterize the cracking behaviour in terms of two parameters, G_c^p corresponding to the onset of the crack propagation, and to the crack arrest, G_c^a corresponding to the arrest of crack growth. G_c^p was calculated using $\bar{\sigma}_{xx}$ and the debond angle θ_d measured prior to cracking, and G_c^a using $\bar{\sigma}_{xx}$ and θ_d after the crack arrest. For the stationary crack tip (meaning, the crack tip which did not increase although the load was increased), no fracture energy is determined.
The fracture energy of the glass fibre/matrix interface for the crack arrest, $G_c^a(\psi)$ and for the crack propagation, $G_c^p(\psi)$ obtained in Paper [A2] is presented in Figure 4.7.

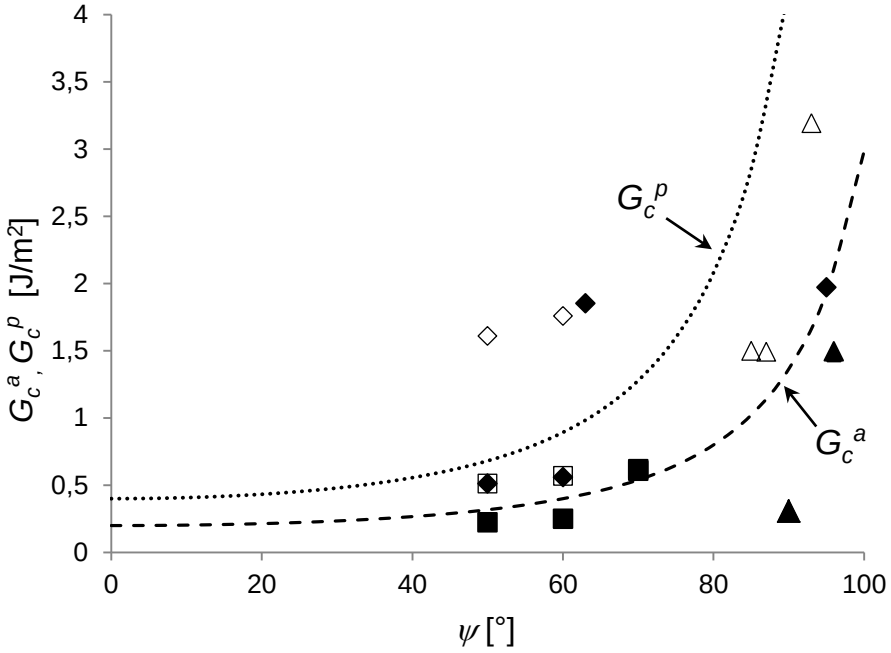

Figure 4.7. Experimentally determined fracture energy for the crack propagation and crack arrest (distinguished by red and black respectively) as a function of phase angle. Symbols are experimental values; curves are fits.

Due to the unstable debond propagation observed in the experiments (Figure 4.2), the fracture energy for mode mixity $\psi < 50°$ could not be measured. However, for $\psi > 50°$ the fracture energy increases with increase of the mode mixity for both $G_c^a(\psi)$ and $G_c^p(\psi)$. The fracture energy determined for $\psi \approx 90°$ is several times that for $\psi \approx 50°$. This is consistent with earlier experimental studies of mixed mode fracture of bi-material interfaces which shown that the fracture energy increases significantly with increasing mode mixity [12,34].

The function [12]

$$G_c(\psi) = G_I^c\{1+\tan^2[(1-\Lambda)\psi]\} \tag{8}$$

was used to fit the data. G_I^c is the value of G_I at $\psi = 0°$ and Λ is a dimensionless constant. Two different fitting curves for crack arrest and crack propagation are plotted

using the function in Eq. 8. The parameters used in fitting the curves to the experimental data points are listed in Table 2.

Table 2. Fitting parameters for G_c^a and G_c^p.

Fitting parameter	Value
$G_c^a\left[J/m^2\right]$	0.2
$\Lambda_a[-]$	0.25
$G_c^p\left[J/m^2\right]$	0.4
$\Lambda_p[-]$	0.2

The fracture energy for mode mixity extrapolated to $\psi \sim 0°$ is found to be $G_c^a(\psi = 0°) \sim 0.2J/m^2$ and $G_c^p(\psi = 0°) \sim 0.4J/m^2$ for crack arrest and crack propagation respectively; for $\psi \sim 90°$ the fracture energy is in the range of $G_c^a(\psi = 90°) \sim 2J/m^2$ and $G_c^p(\psi = 90°) \sim 3J/m^2$.

The determined fracture energy of the interface is relatively low in comparison with the literature; the fracture energy for the similar materials system was determined to be in the range of 2-10J/m^2 and 6-25J/m^2 for $\psi = 0°$ and $\psi = 90°$ respectively [50,51]. The difference might be related to the experimental procedure applied in [49]. The results presented in [50,51] are based on the experimental observations carried out using pre-existing debonds obtained in the previous pull out tests. Moreover, the experimental measurements of the debonds in [50] used in the fracture energy calculations are based on the debonding observations conducted in the optical microscope which does not allow for the precise debond angles measurements (the viewing direction is perpendicular to the fibre orientation, unlike proposed in Figure 2.10).

The fracture energy obtained in the current study for $\psi \sim 90°$ (corresponding to the nominal Mode II, $G_c^a(\psi = 90°) \sim 2J/m^2$ and $G_c^p(\psi = 90°) \sim 3J/m^2$ for crack arrest and

crack propagation respectively), is obviously much lower than the fracture energy obtained for the same materials system by any of the methods described in the background, e.g. pull out or push out tests. It should be noted however, that the fracture energy determined by those methods might be influenced by the frictional sliding which is an issue broadly discussed in the research.

Furthermore, it should be noted that the method proposed in the current study allows for an early detection of cracking by direct observations of the free-edge of the sample (where the debonding initiation occurs), with very high resolution obtained by SEM. The distinction between the fracture energy of the crack arrest and the crack propagation observed in this study has been reported before for other materials e.g. the silicon/epoxy interface cracking [84] or cracking of ceramics [85].

Based on the 3D results presented in Paper [A3], the steady-state energy release rate of a debond tunneling was estimated in Paper [A2] and found to be $G_{ss} = 0.79 J/m^2$. The value of G_{ss} lies within the range of the fracture energy of a debond crack propagation determined using the free surface observations from the SEM, G_c^p for $\psi \approx$ 50 -60° (see Figure 4.7). This strongly supports the hypothesis that the fracture energy values determined from the 2D SEM observations are representative of the fibre/matrix interface along the entire fibre. Thus the approach of using 2D surface observations for the determination of the mixed mode fracture energy of the fibre/matrix interface is then appropriate.

It is noted that the mechanical properties of the materials used in the experimental measurements in the current study are slightly different from those in [11]. It can be seen that in Eq.6 and 7 (Sec. 2.4) that the fracture energy of the fibre/matrix interface depends on the elastic properties of both fibre and the matrix. However, as shown in [11] the geometrical features of the problem play more important role in the fracture process than the elastic properties of involved materials. Therefore, it is believed that the experimental observations presented in Paper [A2] can be linked with model results in [11].

4.3 MIXED MODE COHESIVE LAW FOR THE FIBRE/MATRIX INTERFACE

In Paper [A3] numerical simulations of the fibre/matrix interface debonding were carried out using A-FEM and the model predictions were compared with the experimental observations from SEM presented in Sec.4.1.1.

Three numerical models were analysed. The geometry of the model is the same in all cases (Figure 3.9a). They are meshed with different elements though (elastic or cohesive ones), depending on the studied problem. In the model used for the cohesive law parameters estimation, the domain in Figure 3.9a was meshed with ABAQUS 6.12 continuum elements. In the mode-dependent cohesive-zone model used for the debonding simulations, all elements were replaced by user-defined augmented elements. The mixed mode cohesive law used in this model are described in Sec.3.3 (p. 39).

Several numerical analyses were carried out. By comparing experimental measurements from SEM (debond angles, θ_d and normal openings, δ_n as functions of applied stress, see notation in Figure 2.10 and the experimental results in Figure 4.2), with those obtained in the numerical simulations using A-FEM, the mixed mode fracture energy and the cohesive law parameters of the glass fibre/matrix interface were estimated. An influence of different cohesive law parameters on the debonding process was shown in Paper [A3] by performing several numerical analyses and varying different cohesive law parameters. The main findings from those analyses can be summarized as follows.

The Mode I cohesive strength and critical opening displacement of the glass fibre/matrix interface were found to be $5MPa > \hat{\sigma}_i > 0.75MPa$ and $\delta_{nc\,i} < 0.2\mu m$ respectively. The Mode I and Mode II fracture energy were found to be $\Gamma_{I\,i} \sim 0.1J/m^2$ (see Paper [B3]) and $\Gamma_{II\,i} > 0.4J/m^2$ respectively. The fibre/matrix interfacial debonding was shown to be sensitive to the cohesive law parameters in the range which has been explored in the current study. An example showing the interface strength influence on the debonding initiation and propagation for the constant fracture energy is shown in Figure 4.8. It is clear that the debonding initiation and propagation do not depend only on the fracture energy but are also sensitive to the cohesive peak stress.

The analysis shows that the numerical predictions for debond angle and normal opening as functions of applied stress are in the best agreement with the SEM experimental measurements for $\hat{\tau}_i / \hat{\sigma}_i > 2$. Details about the cohesive law parameters influence on the debonding process can be found in Paper [A3].

The fracture energy found by cohesive-zone approach (Paper [A3]), $\Gamma_{I\,i} \sim 0.1 J/m^2$ is relatively close to the values found by LEFM approach in Paper [A2] ($G_c^a(\psi = 0°) \sim 0.2 J/m^2$ and $G_c^p(\psi = 0°) \sim 0.4 J/m^2$ for crack arrest and crack propagation respectively). It should be noted, that in the numerical simulations included in this study, the stationary crack tip observed in the experiments (and recognized in the fracture energy determination by LEFM approach in Paper [A2]), is not taken into account. It can possibly be the reason for the slight differences of the interface fracture energy determined for $\psi = 0°$ by LEFM approach and by the cohesive-zone approach.

The fibre/matrix interface fracture energy determined in Paper [A3] for $\psi = 0°$ is also much lower in comparison with the values available in the literature, e.g. in [50,51], where fracture energy for nominal Mode I ($\psi = 0°$) is found to be in the range of 2-10J/m^2. The possible reasons for this difference related to the experimental approach in [49] have been discussed before (Sec.4.2).

The fracture energy for the fracture Mode II determined in Paper [A3], $\Gamma_{II\,i} > 0.4 J/m^2$ is also low in comparison with the fracture energy determined by the LEFM approach before in Paper [A2], ($G_c^a(\psi = 90°) \sim 2 J/m^2$ and $G_c^p(\psi = 90°) \sim 3 J/m^2$ for the crack arrest and crack propagation respectively) and much lower than the fracture energy for nominal Mode II reported by Zhang et al. and Varna et al. [50,51], $G_{II} = 6 - 25 J/m^2$. It should be noted, however, that in Paper [A3] the debonding initiation and propagation (described in terms of the debond crack angle and normal opening displacement), were shown to be sensitive to the cohesive law parameters in the range explored in the current study.

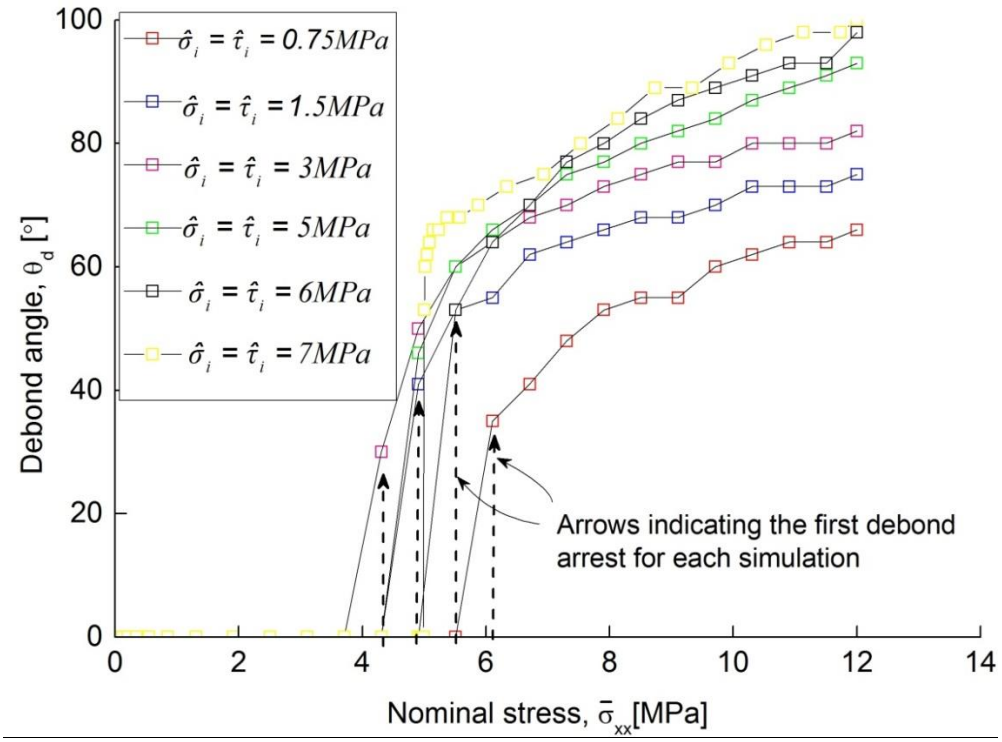

(a)

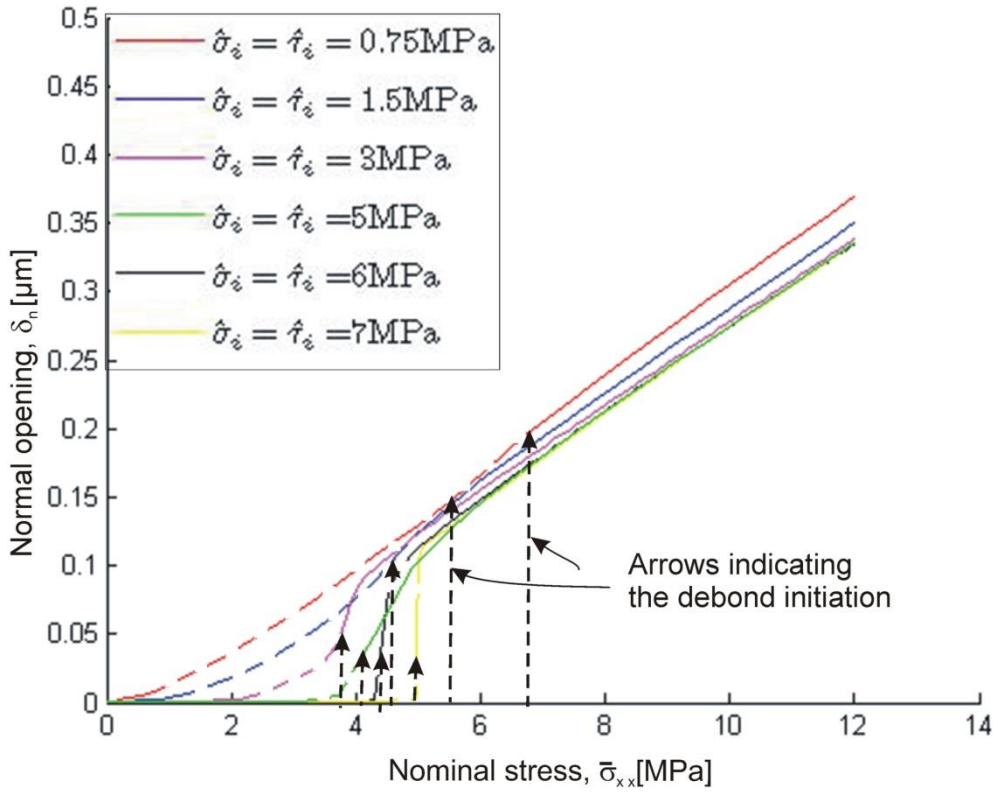

(b)

Figure 4.8. Cohesive strength influence on the debond propagation; a) debond angles, and b) normal openings as functions of applied stress- numerical predictions.

Table 3. Cohesive law parameters used in parametric study for cohesive strength.

$\hat{\sigma}_i = \hat{\tau}_i$ [MPa]	$\delta_{nc\,i}$ [μm]	$\delta_{tc\,i}$ [μm]	$\Gamma_{II\,i} / \Gamma_{I\,i}$ [-]	$\Gamma_{I\,i}$ [J/m^2]
0.75	0.2	0.8	4	0.075
1.5	0.1	0.4	4	0.075
3	0.05	0.2	4	0.075
5	0.03	0.12	4	0.075
6	0.025	0.1	4	0.075
7	0.0214	0.0857	4	0.075

The interfacial shear strength is found to be around two times the tensile strength, $\hat{\tau}_i / \hat{\sigma}_i > 2$. The ratio found to be $\hat{\tau}_i / \hat{\sigma}_i > 2$ is slightly larger than the one found for the same material system studied by the cohesive-zone approach in [14], $\hat{\tau}_i / \hat{\sigma}_i > 0.7 - 1.2$. However, the results in [14] are obtained by using experimental observations of the debonding carried out in the optical microscope, with the view perpendicular to the fibre direction. The test set up proposed in the current study, utilizing high SEM images resolution and viewing the free-edge of the sample where the debonding initiation is expected to occur, allows possibly for an earlier damage detection and thereby can be considered as the method allowing for more precise measurements.

4.4 FIBRE/MATRIX INTERFACIAL CRACK KINKING

As described in the section of theoretical background (Sec.2.2.3), when analysing an interfacial debonding between dissimilar materials, the competition between the crack propagating along the interface and its kinking out to the adjoining material should be taken into account. Therefore, in the current study the fibre/matrix interfacial crack

kinking phenomenon was investigated experimentally (in 2D and in 3D) and numerically (in 2D).

In Paper [A2] the fibre/matrix interfacial crack kinking was observed *in situ* during the fracture testing in SEM. The kinking occurred at the average stress of $\bar{\sigma}_{xx} \sim 13MPa$ and at the debond angle $\theta_d = 60° \pm 14°$ (example shown in Figure 4.9). It can be seen in Figure 4.9 that in case of different samples, the crack kinked at different angles. The value of $\theta_d = 60° \pm 14°$ is an average of the angle of kinking based on different experiments. The kinked crack propagated unstably in the matrix, in the direction nearly perpendicular to the applied stress.

The crack kinking observed in the experiments is in good agreement with the numerical predictions obtained by the LEFM analysis by París et al. [11], whose results indicate that the interfacial crack kinking occurs in the interval $\theta_d = 60° - 70°$.

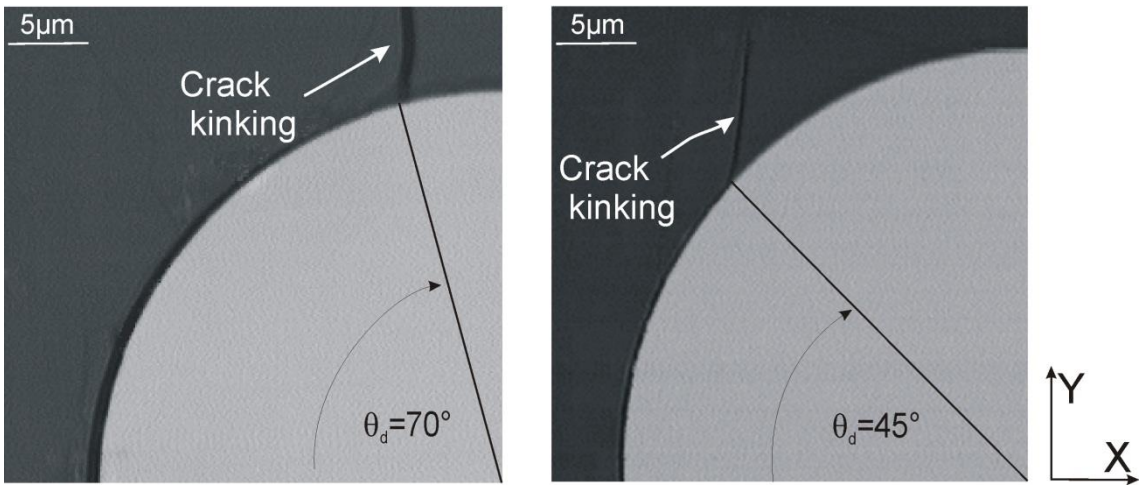

Figure 4.9. Examples of the interfacial crack kinking observed in SEM testing. The stress is applied in *x*-direction.

The experimental observations of the crack kinking are also in agreement with results reported by Evans et al. [36] who also studied the path of a crack kinking out of an interface between dissimilar materials by LEFM approach. Evans et al. [36] shown that in general, the preferred path of the crack is influenced by the magnitude of the mode mixity, ψ at the crack tip, in a way that the interfacial crack kinking occurs most likely

when $\psi \approx 70°$. By linking the experimental observations presented in the current study, with the model results from [11], the debonding angle $\theta_d = 60° \pm 14°$ which is the angle of observed kinking initiation, corresponds to a mode mixity of $\psi(\theta_d \approx 60°) \sim 80°$ (details in Paper [A2]). Moreover, in [36] the crack was shown to kink into the material with the lowest Young's modulus as observed in the experiments presented in the current study.

In Paper [A1] where the interfacial debonding was observed in 3D by means of X-ray tomography, the kinked cracks were visible only at the final load steps, ($\bar{\sigma}_{xx} > 42.5MPa$, example shown in Figure 4.10.) Moreover, the crack kinking was observable only down to *z*~10µm (*z* axis according to the notation in Figure 3.7). As discussed before in [11] it was predicted that crack kinking is most likely to occur at the debond angle of $\theta_d = 60° - 70°$. In other words, the kinking phenomenon is related to a critical debond angle. Since inside the specimen, for *z* >10µm the debond did not reach the critical angle of $\theta_d = 60° - 70°$, it makes good sense that the crack kinking did not occur. This hypothesis could be possibly checked by a 3D numerical modelling of the problem.

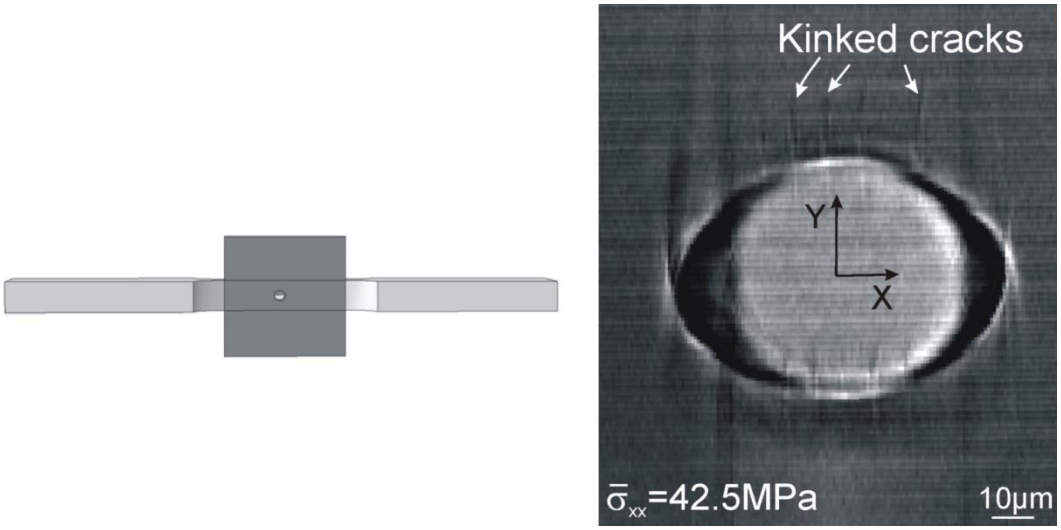

Figure 4.10. Tomography slice presenting the free surface of the sample with visible kinked cracks at high applied stress level. The load is applied in *x*-direction.

In Paper [A3] the fibre/matrix interfacial crack kinking phenomenon was studied by numerical modelling applying the cohesive-zone approach. It was found that kinking occurrence is controlled by the strength of the matrix, $\hat{\sigma}_m, \hat{\tau}_m$ and is independent of the matrix toughness, $\Gamma_{I\,m}$, $\Gamma_{II\,m}$. Figure 4.11 shows the numerical predictions for kinking obtained for a wide range of matrix toughness but for the same matrix cohesive strength. It can be noticed, that the predicted kinking position is exactly the same in all cases for the same matrix strength, $\hat{\sigma}_m = \hat{\tau}_m = 39MPa$. The finding that the crack kinking is controlled more by the cohesive strength than by the fracture energy is similar to the results of the analysis of the interface crack penetration into the substrate in [38] where the crack penetration into the substrate or its deflection into the interface was shown to be controlled by the substrate to the interface strength ratio rather than by their toughness ratio.

Further studies of the toughness/strength role on the interfacial crack kinking phenomenon are required, so the results presented in Paper [A3] can be confirmed.

In Paper [A3] for $\hat{\sigma}_m = \hat{\tau}_m = 39MPa$ the kinking was predicted to occur at the angle of $\theta_d \sim 60°$ which is in good agreement with the experimental observations shown in this study (Sec. 4.1) and with the numerical predictions obtained by LEFM by París et al. [11]. For $\hat{\sigma}_m < 39$, the angle of kinking decreases as shown in Figure 4.12. The range of experimentally measured kinking angle is marked as grey area. For $20MPa < \hat{\sigma}_m < 39MPa$, the kinking angle obtained from the numerical model is in a good agreement with experimental measurements. This suggests that the matrix strength, $\hat{\sigma}_m$ is within this range.

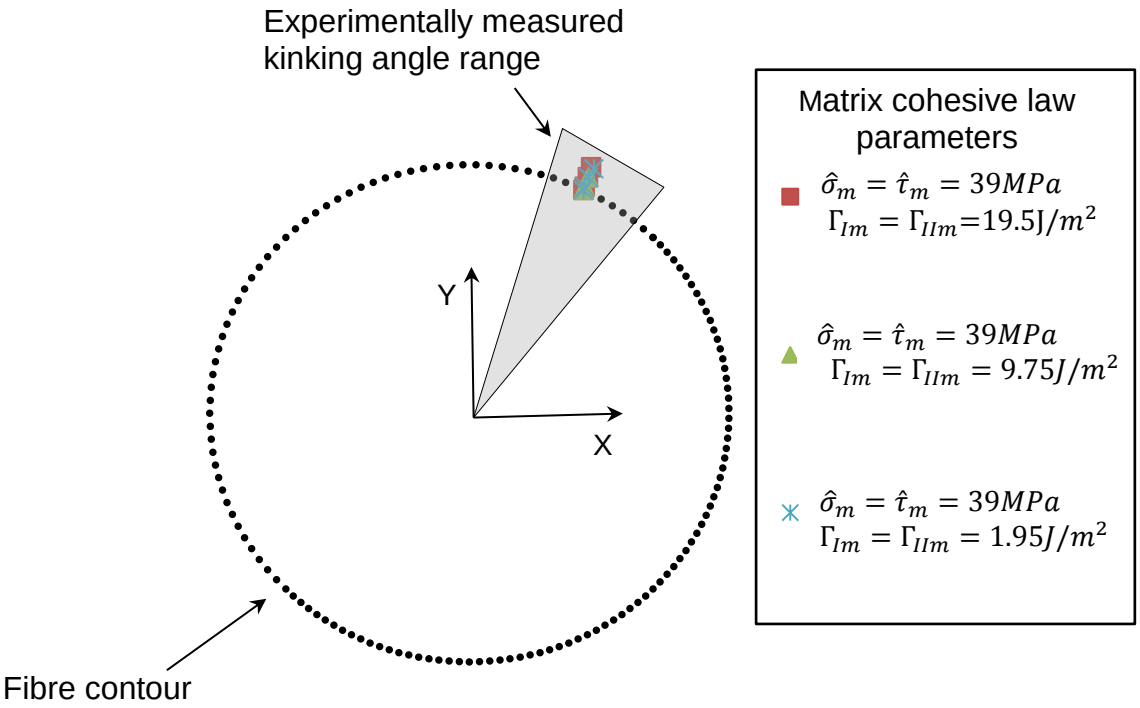

Figure 4.11. Numerical predictions for the crack kinking initiation obtained for the same matrix strength, $\hat{\sigma}_m = \hat{\tau}_m = 39MPa$ and different interface toughness values, $\Gamma_{I\,m} = \Gamma_{II\,m}$. The area marked with grey colour indicates the kinking angle determined in SEM observations.

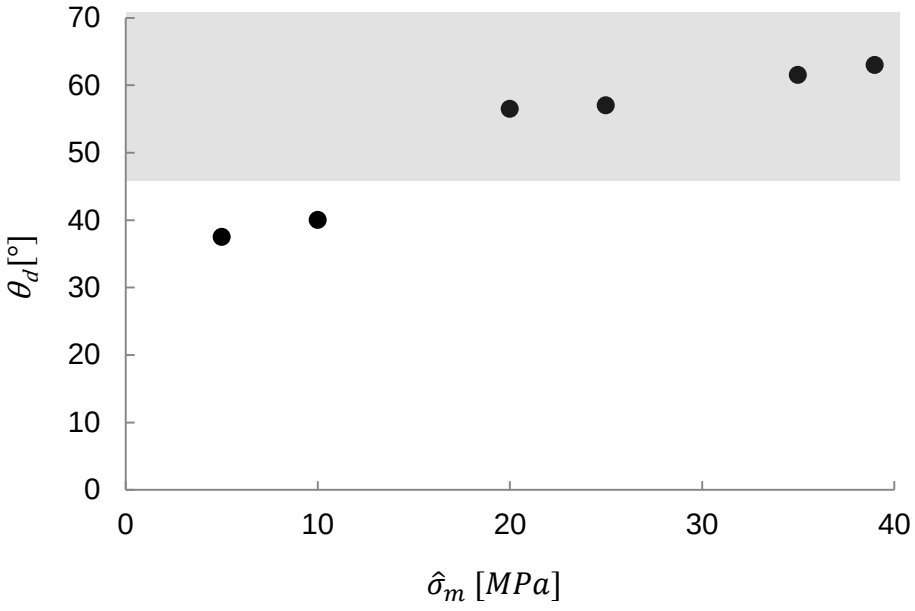

Figure 4.12. Finite element results for the kinking angle as a function of matrix strength. The grey area indicates the angle of the crack kinking determined in the experiments.

4.5 TOMOGRAPHY ARTIFACTS AND COMPLICATIONS

Based on previous studies on composite materials it was initially assumed that X-ray tomography as a non-destructive testing method does not have significant influence on the materials properties. However, some observations of the current study indicate that the X-rays may damage the polymer-based samples subjected to the external load. This suspicion is based on the following observations.

The fibre protrusion (described in details in Paper [A1]), observed after the final load steps (from $\bar{\sigma}_{xx} = 39.5MPa$ to $\bar{\sigma}_{xx} = 44.2MPa$), seems to be larger than protrusion observed after the previous loading steps. Moreover, after the scanning, the local shape/colour changes in the scanned volumes of the samples were visible to the naked eye. Those changes seem to be related to the exposure time in a way that the samples that had been exposed to the X-rays for longer time were found to have more intensive colour/shape change of the scanned volume than those with shorter scanning times.

At scanning of the specimen containing the glass marker particles by means of X-ray tomography, unexpected artifacts that caused the outline of the particles to be blurred were observed. Since the artifacts did not allow for the intended 3D strain mapping and due to the lack of any reported difficulties for similar studies, it was found to be worth describing the problem observed in the current study.

The glass particles blended with the resin gave a sufficient contrast in the tomography images and they were found to be relatively evenly distributed in the samples as shown in Figure 4.13.

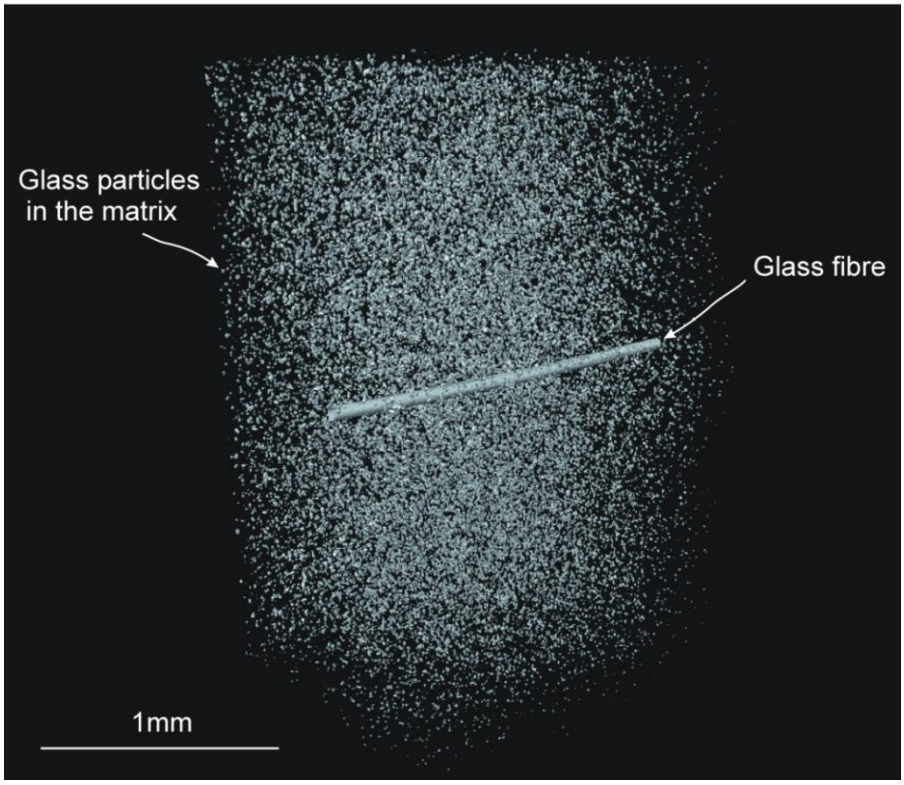

Figure 4.13. Tomography sub-set showing the glass particles distribution in the sample. The matrix is rendered invisible.

However, very severe type of artifacts were discovered in the reconstructed data. An example of blurred outline of the particles embedded in the matrix is shown in Figure 4.4 (in the previous section) and in Figure 4.15. In Figure 4.15 the intensity of the artifacts is shown to be related to the applied stress and/or to the exposure time of the

sample. It can be noticed, that the particles outline become more blurred with increasing the load which corresponds to the exposure time as well. This might indicate a similar dependency as observed in the case of the colour/shape change and the fibre protrusion described before. Therefore, the scanning time should be minimized during *in situ* mechanical testing of polymer-based composites by means of X-ray tomography in order to decrease the risk of radiation damage.

The artifacts observed in the current study, shown in Figure 4.15 and Figure 4.15 are somewhat similar to those reported by Haldrup [78] as the artifacts caused by the stage drifting during the scanning (Figure 4.16). However, the artifacts shown in Figure 4.4 and Figure 4.15 were observed in the data acquired from tests carried out at two different beamlines which makes it rather unlikely that exactly the same stage drifting was the problem at both facilities. Therefore, the problem should be further investigated.

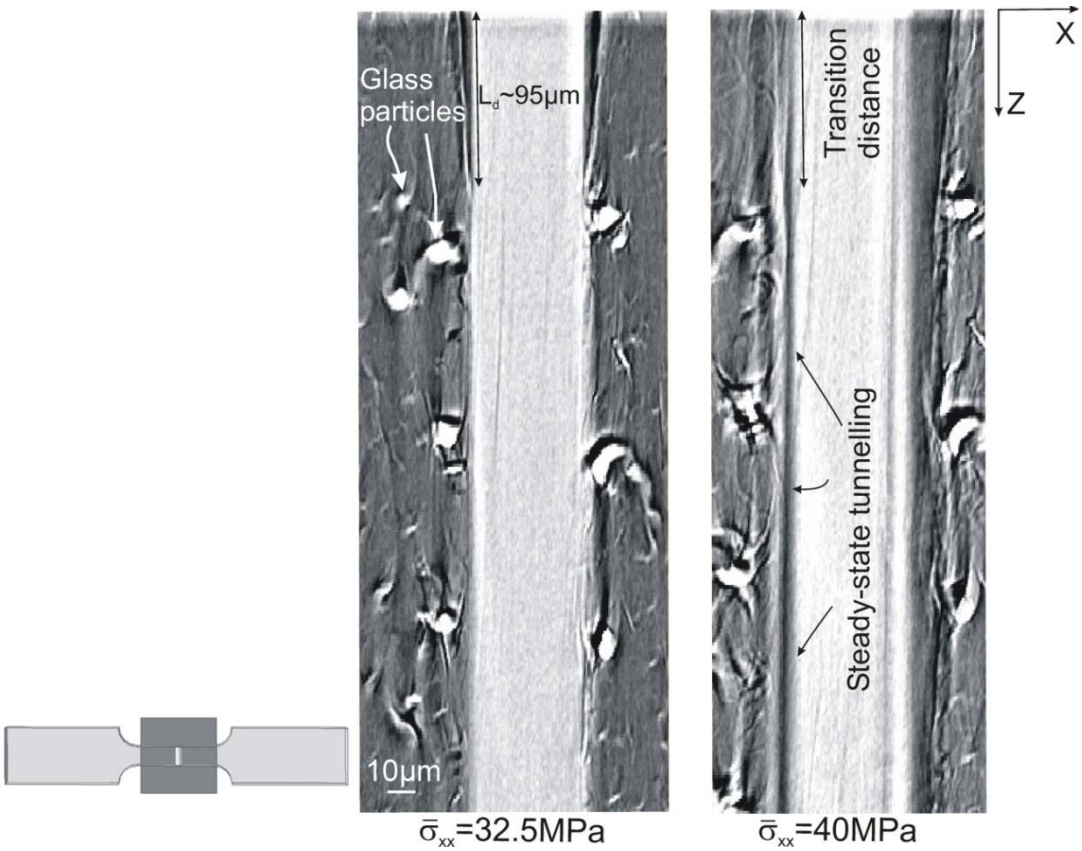

Figure 4.14. Artifacts visible in the X-ray tomography data (blurred outline of the glass particles).

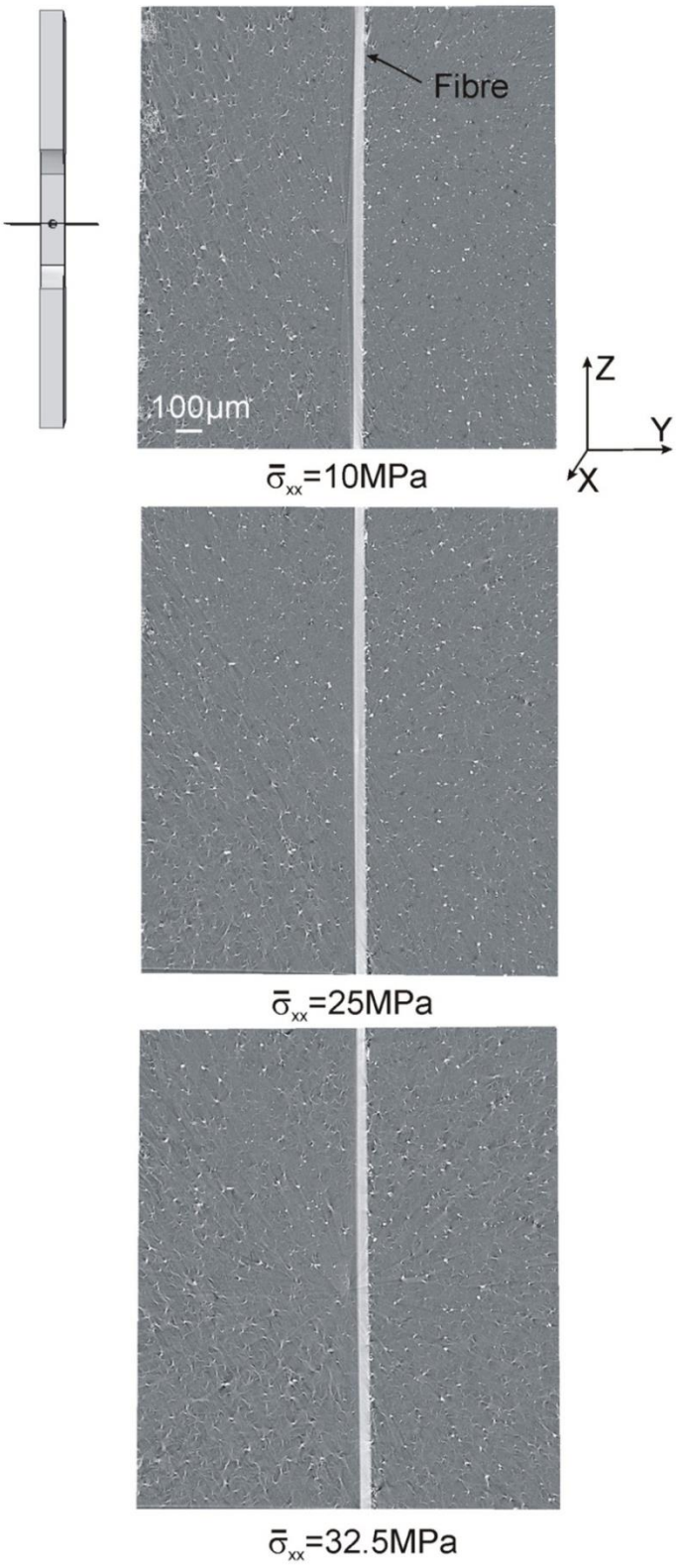

Figure 4.15. A reconstructed slice through the sample demonstrating the artifacts (blurred outline of the glass particles) observed in the images of the samples with the glass particles embedded in the matrix.

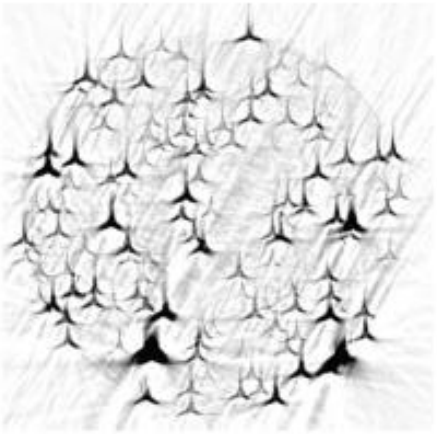

Figure 4.16. Artifacts caused by the stage drift by Haldrup [78]. The scanned sample was made of aluminum blended with the tungsten marker particles.

5 CONCLUSIONS

The main goal of this project has been to investigate the microscale damage in glass-fibre composites used for wind turbine rotor blades. Special focus has been put on the determination of fracture parameters for the fibre/matrix interface debonding and the subsequent interfacial crack kinking into the matrix. This section summarizes the main findings of this thesis.

Experimental investigation of a single fibre specimen subjected to a remote uniform tensile stress carried out in the SEM allowed for observations of a very early debonding initiation at the free surface and of the subsequent damage propagation. The *in situ* measurements of the debond angle and the normal opening as a function of the applied stress obtained in these experiments allowed for the determination of the mixed mode fracture energy of the interface. Two different approaches were applied for the fracture energy determination, LEFM and the cohesive-zone approach. The two approaches gave similar values for the mixed mode fracture energy of the glass fibre/matrix interface. By a coupled experimental and numerical study, applying A-FEM simulations, the fibre/matrix interface cohesive law parameters were identified. The results of the numerical simulations show that the interfacial debonding process is sensitive to the cohesive law parameters (peak stress and the critical opening displacements) within the range which has been explored in this thesis.

Images obtained from X-ray tomography data allowed for the study of the fibre/matrix debonding process in 3D. The fibre/matrix debonding is found to initiate at the free surface of the sample and propagate inside the sample. Once the debond depth exceeded z ~100μm which corresponds to two fibre diameters, the debond crack propagated unstably along the fibre (steady-state crack tunnelling). The debond angles and normal openings observed at the free-edge of the sample and those observed inside the material are shown to be significantly different.

X-ray tomography is shown to be very promising tool for 3D investigations of fracture of composite materials. The importance of 3D observations have been presented by showing the difference between the debond evolution at the free surface and that inside

the specimen. Disadvantages of the technique have been assessed. Observations of the specimens after scanning, indicate possible risk of radiation damage of polymer-based composites by X-rays during *in situ* mechanical testing. It is suggested that the scanning time should be minimized in order to decrease the risk of radiation damage.

The phenomenon of interfacial crack kinking into the matrix was studied by coupled experimental and numerical approach. Experimental investigations by SEM (2D) and by X-ray tomography (3D) support the hypothesis that the kinking phenomenon is related to the debond angle. The kinking cracks observed in this study is shown to be only a free-surface phenomenon. Simulations of the interfacial crack kinking indicate that the interfacial crack deflection to the adjoining materials is controlled by the tensile strength of the matrix and is independent on the matrix toughness.

All in all, this thesis has given a new insight on the fracture of a fibre/matrix interface and its further propagation. Its novelty is based on the experimental observations which take into account the mode mixity of the interfacial crack and provide a 3D picture of the fibre/matrix debonding process and the associated interfacial crack kinking. A coupled experimental and numerical approach enables the determination of fracture parameters that can be used for micromechanical modelling of a glass fibre/matrix interface debonding. These include the fracture energy as a function of mode mixity and mixed mode cohesive law parameters which so far often have been chosen quite arbitrarily in model studies, since no experimentally measured data were available.

6 FUTURE WORK

Further investigations of the fibre/matrix interface fracture parameters should be carried out in order to test the accuracy of the mixed mode fracture energy and cohesive law parameters determined in this thesis. Ideally, the parameters determined in this thesis should be applied in a micromechanical model consisting of several fibres. The response of the model compared with the experimental observations of the same problem would allow for verifying the parameters determined in the current study.

Due to the unstable fibre/matrix debond propagation (from $\theta_d = 0°$ to $\theta_d \sim 50°$) shown in Paper [A2], the fracture energy of the interface is determined only for the mode mixity higher than 50°. It is of high interest to obtain the fracture energy for the smaller debond angles such that it becomes possible to measure fracture energy for lower values of ψ. The debond growth could possibly be stabilize by another fibre placed in the neighbourhood; thereby the fracture energy for $\psi < 50°$ might be determined.

In the experimental set up presented in this thesis, only normal opening was measured in fact. The accuracy of the experimental measurements of the debonds in 2D and 3D observations could be possibly increased by applying Digital Image Correlation (DIC) technique, which has been proposed for microscopic displacement mapping using images acquired by SEM [57,59,86] and also for 3D strain mapping using tomography scanning [69,87]. DIC method would allow for the measurements of both the normal and tangential crack opening displacements [57]. Thereby, the critical tangential displacement of the fibre/matrix interface could potentially be determined. Such DIC investigations were planned as part of this thesis, but due to experimental difficulties, and eventually time constrains, this will rely on future studies.

3D *in situ* measurements of the debond angles and normal openings obtained from tests at synchrotron facility, can be used for the micromechanical modelling in similar manners to the 2D cohesive-zone modelling presented in Paper [A3]. By comparing the interior debonds from the experimental observations in Paper [A3] with those obtained

from the model predictions, the difference of the debonds observed at the free surface and inside the sample could be investigated.

In order to investigate the influence of the X-rays on the polymer-based composite materials subjected to an external load, a study with different combinations of radiation time, applied stress and energy of the X-ray beam should be performed.

BIBLIOGRAPHY

[1] The European Wind Energy Association. The economics of wind energy. 2009.

[2] Brøndsted P, Lilholt H, Lystrup A. Composite Materials for Wind Power Turbine Blades. Annual Review of Materials Research 2005;35:505–38.

[3] Sørensen BF, Holmes JW, Brøndsted P, K B. Blade Materials, Testing Methods and Structural Design. Wind Power Generation and Wind Turbine Design, 2010, pp. 417–60.

[4] Assesment of Research Needs For Wind Turbine Rotor Materials Technology. National Research Council; 1991.

[5] Lee SM. Influence of fiber/matrix interfacial adhesion on composite fracture behavior. Composites Science and Technology 1992;43:317–27.

[6] Larson BK, Drzal LT. Glass fibre sizing/matrix interphase formation in liquid composite moulding: effects on fibre/matrix adhesion and mechanical properties. Composites 1994;25:711–21.

[7] Gamstedt EK, Sjögren BA. Micromechanisms in tension-compression fatigue of composite laminates containing transverse plies. Composites Science and Technology 1999;59:167–78.

[8] Hull D, Clyne TW. An introduction to composite materials. Second Edi. Cambridge: Press Syndicate of the University of Cambridge; 1981.

[9] Zhandarov SF, Pisanova E V. The local bond strength and its determination by fragmentation and pull-out test. Composites Science and Technology 1997;57:957–64.

[10] Watson MC, Clyne TW. The tensioned push-out test for fibre-matrix interface characterisation under mixed mode loading. Materials Science and Engineering: A 1993;160:1–5.

[11] París F, Correa E, Mantič V. Kinking of Transversal Interface Cracks Between Fiber and Matrix. Journal of Applied Mechanics 2007;74:703–16.

[12] Hutchinson JW, Suo Z. Mixed Mode Cracking in Layered Materials. Advances in Applied Mechanics, 1992, pp. 63–191.

[13] Hutchinson JW. Mixed mode fracture mechanics of interfaces. Metal-Ceramics, Acta-Scripta Metallurgica Proceedings Series 1990;4:295–306.

[14] Koyanagi J, Shah PD, Kimura S, Ha SK, Kawada H. Mixed-Mode Interfacial Debonding Simulation in Single-Fiber Composite under a Transverse Load. Journal of Solid Mechanics and Materials Engineering 2009;3:796–806.

[15] Dugdale DS. Yielding of steel sheets containing slits. J. Mech. Phys. Solids 1953;8:100–4.

[16] Liu W, Yang QD, Mohammadizadeh S, Su XY, Ling DS. An Accurate and Efficient Augmented Finite Element Method for Arbitrary Crack Interactions. Journal of Applied Mechanics 2013;80.

[17] Canal LP, González C, Segurado J, LLorca J. Intraply fracture of fiber-reinforced composites: Microscopic mechanisms and modeling. Composites Science and Technology 2012;72:1223–32.

[18] Timoshenko SP. History of strength of materials. New York: Dover Publishing; 1953.

[19] Griffith A. The phenomena of rapture and flow in solids. Proceedings of the Royal Society A-Mathematics, Physics and engineering Sciences, vol. 221, 1921, pp. 163–98.

[20] Irwin GR, Kies JA, Smith HL. Fracture strength relative to onset and arrest of crack propagation. Proceedings of the American Society for Testing Materials, 1958.

[21] Irwin GR. Analysis of stress and strain near the end of a crack transversing a plate. Journal of Applied Mechanics 1957;24:361–4.

[22] Fischer-Cripps AC. Linear Elastic Fracture Mechanics. Introduction to Contact Mechanics, 2007, pp. 31–48.

[23] Sørensen BF. Cohesive laws for assessment of materials failure: Theory, experimental methods and application. 2010.

[24] Services A, Information T, Station AH. Barenblatt, G I. Advances in Applied Mechanics 1962;7:55–129.

[25] Li S, Thouless MD, Waas a. M, Schroeder J a., Zavattieri PD. Mixed-mode cohesive-zone models for fracture of an adhesively bonded polymer–matrix composite. Engineering Fracture Mechanics 2006;73:64–78.

[26] Yang QD, Thouless MD. Mixed-mode fracture analyses of plastically-deforming adhesive joints. International Journal of Fracture 2001;110:175–87.

[27] Tvergaard V, Hutchinson JW. The relation between crack growth resistance and fracture process parameters in elastic-plastic solids. Journal of the Mechanics and Physics of Solids 1992;40:1377–97.

[28] Dundurs J. Edge-bonded dissimilar orthogonal elastic wedges. Journal of Applied Mechanics 1969;36:650–2.

[29] Rice RJ. Elastic Fracture Mechanics Concepts for Interfacial Cracks. Journal of Applied Mechanics 1988;55:98–103.

[30] Correa E, Gamstedt EK, París F, Mantič V. Effects of the presence of compression in transverse cyclic loading on fibre–matrix debonding in unidirectional composite plies. Composites Part A: Applied Science and Manufacturing 2007;38:2260–9.

[31] Rice JR. Elastic Fracture Mechanics Concepts for Interfacial Cracks. Journal of Applied Mechanics 1988;110:98–103.

[32] Carlsson L, Matteson R, Aviles F, Loup D. Crack path in foam cored DCB sandwich fracture specimens. Composites Science and Technology 2005;65:2612–21.

[33] Comninou M. The Interface Crack. Journal of Applied Mechanics 2013;44:631–6.

[34] Liechti KM, Chai YS. Asymmetric Shielding in Interfacial Fracture Under In-Plane Shear. Journal of Applied Mechanics 1992;59:295–304.

[35] Cao HC, Evans AG. An experimental study of the fracture resistance of bimaterial interfaces. Mechanics of Materials 1989;7:295–304.

[36] Evans AG, Dalgleish M, He M, Hutchinson JW. On crack path selection and the interface fracture energy in bimaterial systems. Acta Metall. Mater 1989;37:3249–54.

[37] He M-Y, Hutchinson JW. Kinking of a Crack Out of an Interface. Journal of Applied Mechanics 1989;56:270–8.

[38] Parmigiani J, Thouless M. The roles of toughness and cohesive strength on crack deflection at interfaces. Journal of the Mechanics and Physics of Solids 2006;54:266–87.

[39] Bogy DB. Two Edge-Bonded Elastic Wedges of Different Materials and Wedge Angles Under Surface Tractions. Journal of Applied Mechanics 1971;38:377–86.

[40] Klingbeil NW, Beuth JL. On the design of debond-resistant bimaterials Part II : A comparison of free-edge and interface crack approaches. Engineering Fracture Mechanics 2000;66:111–28.

[41] Beom HG, Zhuo XR, Cui CB. Tunneling cracks in the adhesive layer of an orthotropic sandwich structure. International Journal of Engineering Science 2013;63:40–51.

[42] Kerans RJ, Parthasarathy TA. Theoretical Analysis of the Fiber Pullout and Pushout Tests. J. Am. Ceram. Soc. 1991;74:1585–96.

[43] Zhandarov S. Characterization of fiber/matrix interface strength: applicability of different tests, approaches and parameters. Composites Science and Technology 2005;65:149–60.

[44] Wagner HD, Nairn JA, Detassis M. Toughness of Interfaces from Initial Fiber-Matrix Debonding in a Single Fiber Composite Fragmentation Test. Applied Composite Materials 1995;2:107–17.

[45] Ageorges C, Friedrich K, Schüller T, Lauke B. Single-fibre Broutman test: fibre–matrix interface transverse debonding. Composites Part A: Applied Science and Manufacturing 1999;30:1423–34.

[46] Miller B, Muri P, Rebenfeld L. A microbond method for determination of the shear strength of a fiber/resin interface. Composites Science and Technology 1987;28:17–32.

[47] Hampe A, Marotzke C. The fracture toughness of glass fibre- polymer matrix interface: measurement and theoretical analysis. Proc. Third Int.Conf. Deformation and Fracture of Composites 1995:132.

[48] Chua PS, Piggott MR. The Glass Fibre-Polymer Interface : II Work of Fracture and Shear Stresses. Composites Science and Technology 1985;22:107–19.

[49] DiBenedetto AT. Measurement of the Thermomechanieal Stability of Interphases by the Embedded Single Fiber Test A. T. DiBenedetto. Composites Science and Technology 1991;42:103–23.

[50] Zhang H, Ericson ML, Varna J, Berglund LA. Transverse single-fibre test for interfacial debonding in composites: 1. Experimental observations. Composites Part A: Applied Science and Manufacturing 1997;28:309–15.

[51] Varna J, Berglund LA, Ericson ML. Transverse single-fibre test for interfacial debonding in composites:2. Modelling. Composites Part A: Applied Science and Manufacturing 1997;28A:317–26.

[52] Meurs PFM, Schrauwen BAG, Schreurs PJG, Peijs T. Determination of the interfacial normal strength using single fibre model composites. Composites Part A: Applied Science and Manufacturing 1998;29:1027–34.

[53] Toya M. A crack along the interface of a circural inclusion embedded in an infinite solid. J. Mech. Phys. Solids 1974;22:325–48.

[54] Mantič V. Interface crack onset at a circular cylindrical inclusion under a remote transverse tension. Application of a coupled stress and energy criterion. International Journal of Solids and Structures 2009;46:1287–304.

[55] Goodhew J P, Humphreys J, Beanland R. Electron Microscopy and Analysis. third. London: Taylor & Francis; 2001.

[56] Sørensen BF, Horsewell A, Jørgensen O, Kumar AN. Fracture Resistance Measurement Method for in situ Observation of Crack Mechanisms. J. Am. Ceram. Soc. 1998;81:661–9.

[57] Sutton MA, Orteu J, Schreier HW. Image Correlation for Shape, Motion and Deformation Measurements. 2009.

[58] Berfield T a., Patel JK, Shimmin RG, Braun P V., Lambros J, Sottos NR. Micro- and Nanoscale Deformation Measurement of Surface and Internal Planes via Digital Image Correlation. Experimental Mechanics 2007;47:51–62.

[59] Sutton MA, Li N, Garcia D, Cornille N, Orteu JJ, McNeill SR, Schreier HW, Li X, Reynolds a. P. Scanning Electron Microscopy for Quantitative Small and Large Deformation Measurements Part II: Experimental Validation for Magnifications from 200 to 10,000. Experimental Mechanics 2007;47:789–804.

[60] Canal LP, González C, Molina-Aldareguía JM, Segurado J, LLorca J. Application of digital image correlation at the microscale in fiber-reinforced composites. Composites Part A: Applied Science and Manufacturing 2012;43:1630–8.

[61] Als-Nielsen J, McMorrow D. Elements of Modern X-ray Physics. 2011.

[62] Landis EN, Keane DT. X-ray microtomography. Materials Characterization 2010;61:1305–16.

[63] Wright P, Moffat A, Sinclair I, Spearing S. High resolution tomographic imaging and modelling of notch tip damage in a laminated composite. Composites Science and Technology 2010;70:1444–52.

[64] Schilling PJ, Karedla BR, Tatiparthi AK, Verges M a., Herrington PD. X-ray computed microtomography of internal damage in fiber reinforced polymer matrix composites. Composites Science and Technology 2005;65:2071–8.

[65] Rask M, Madsen B, Sørensen BF, Fife JL, Martyniuk K, Lauridsen EM. In situ observations of microscale damage evolution in unidirectional natural fibre composites. Composites Part A: Applied Science and Manufacturing 2012;43:1639–49.

[66] Toda H. A 3D measurement procedure for internal local crack driving forces via synchrotron X-ray microtomography. Acta Materialia 2004;52:1305–17.

[67] Nielsen S., Poulsen H., Beckmann F, Thorning C, Wert J. Measurements of plastic displacement gradient components in three dimensions using marker particles and synchrotron X-ray absorption microtomography. Acta Materialia 2003;51:2407–15.

[68] Brault R, Germaneau a., Dupré JC, Doumalin P, Mistou S, Fazzini M. In-situ Analysis of Laminated Composite Materials by X-ray Micro-Computed Tomography and Digital Volume Correlation. Experimental Mechanics 2013;C.

[69] Haldrup K, Nielsen SF, Mishnaevsky, Jr. L, Beckmann F, Wert J a. 3-dimentional strain fields from tomographic measurements. In: Bonse U, editor. Developments in X-Ray Tomography V, 2006.

[70] Rask M. Microstructure and Mechanical Properties of Aligned Natural Fibre Composites. 2012.

[71] Yang Q, Cox B. Cohesive models for damage evolution in laminated composites. International Journal of Fracture 2005;133:107–37.

[72] Blackman BRK, Hadavinia H, Kinloch AJ, Williams JG. The use of cohesive zone morel to study the fracture of fibre composites and adhesively-bonded joints. International Journal of Fracture 2003;119:25–46.

[73] Belytschko T, Black T. Elastic Crack Growth in finite Elements with Minimal Remeshing. International Journal for Numerical Methods in Engineering 1999;45:601–20.

[74] Zhu Q, Geubelle PH, Li M, Tucker CL. Dimensional Accuracy of Thermoset Composites: Simulation of Process-Induced Residual Stresses. Journal of Composite Materials 2001;35:2171–205.

[75] Tanoglu M, Ziaee S, Mcknight SH. Investigation of properties of fiber / matrix interphase formed due to the glass fiber sizings. Journal of Materials Science 2001;36:3041–53.

[76] Wagner HD, Zhou X-F. A twin-fiber fragmentation experiment. Composites Part A: Applied Science and Manufacturing 1998;29A:331–5.

[77] Feih S, Wonsyld K, Minzari D, Westermann P, Lilholt H, Feih AS. Testing procedure for the single fiber fragmentation test. 2004.

[78] Haldrup K. Measurements of local plastic strain in the bulk of optically opaque materials by synchrotron X-ray micro-tomography. 2007.

[79] Ochi SC, Accorsi ML, Jordan E. Influence of embedded markers on the response of the host material. Journal of Testing and Evaluation 1995;23:196–202.

[80] Zhuang X, Yan X. Investigation of damage mechanisms in self-reinforced polyethylene composites by acoustic emission. Composites Science and Technology 2006;66:444–9.

[81] Wang J-S, Suo Z. Experimental Determination of Interfacial Toughness Curves Using Brazil-Nut-Sandwiches. Acta Metall. Mater 1990;38:1279–90.

[82] Ho S, Suo Z. Tunneling cracks in constrained layers. Journal of Applied Mechanics 1993;60:890–4.

[83] Nakamura T, Kamath MS. Three-dimentional effects in thin film fracture mechanics. Mechanics of Materials 1992;13:67–77.

[84] Gowrishankar S, Mei H, Liechti KM, Huang R. A comparison of direct and iterative methods for determining traction-separation relations. International Journal of Fracture 2012;177:109–28.

[85] Kumar AN, Sørensen BF. Fracture Resistance and Stable Crack-Growth Behavior of. J. Am. Ceram. Soc. 2000;83:1199–206.

[86] Kang J, Jain M, Wilkinson DS, Embury JD. Microscopic Strain Mapping Using Scanning Electron Microscopy Topography Image Correlation at Large Strain. The Journal of Strain Analysis for Engineering Design 2005;40:559–70.

[87] Haldrup, K, Nielsen, SF, Wert AJ. A General Methodology for Full-Field Plastic Strain Measurements Using X-ray Absorption Tomography and Internal Markers. Experimental Mechanics 2008;48:199–211.

PUBLICATIONS

[A1] 3D *in situ* observations of glass fibre/matrix interfacial debonding.
Karolina Martyniuk, Bent F. Sørensen, Peter Modregger, Erik M. Lauridsen.
Compos Part A 55 (2013):63–73.

[A2] *In situ* determination of mixed mode fracture energy of glass fibre/matrix interface.
Karolina Martyniuk, Bent F. Sørensen, Stergios Goutianos.
Submitted to Composites Part A

[A3] Mixed mode cohesive-zone model for identification of fracture properties of a fibre/matrix interface under transverse load.
Karolina Martyniuk, Bent F. Sørensen, Qingda Yang, Wei Liu.
To be submitted to Composites Part A

[B1] Mixed mode cohesive law for fibre/matrix interface- a coupled experimental and numerical study.
K. Martyniuk, B.F. Sørensen, Q. Yang, W. Liu.
Proceedings of 19th International Conference on Composite Materials (ICCM-19), July, 2013, Montreal, Canada.

APPENDIX A1

3D *in situ* observations of glass fibre/matrix interfacial debonding

Composites Part A 55 (2013):63–73.

Composites: Part A 55 (2013) 63–73

Contents lists available at ScienceDirect

Composites: Part A

journal homepage: www.elsevier.com/locate/compositesa

3D *in situ* observations of glass fibre/matrix interfacial debonding

Karolina Martyniuk [a,*], Bent F. Sørensen [a], Peter Modregger [b,c], Erik M. Lauridsen [d]

[a] Section of Composites and Materials Mechanics, Department of Wind Energy, Technical University of Denmark, Risø Campus, 4000 Roskilde, Denmark
[b] Swiss Light Source, Paul Scherrer Institut, 5232 Villigen, Switzerland
[c] School of Biology and Medicine, University of Lausanne, 1015 Lausanne, Switzerland
[d] Department of Energy Conversion and Storage, Technical University of Denmark, Risø Campus, 4000 Roskilde, Denmark

ARTICLE INFO

Article history:
Received 15 March 2013
Received in revised form 9 July 2013
Accepted 18 July 2013
Available online 11 August 2013

Keywords:
A. Glass fibres
B. Interface
B. Debonding
Synchrotron X-ray tomography

ABSTRACT

X-ray microtomography was used for 3D *in situ* observations of the evolution of fibre/matrix interfacial debonding. A specimen with a single fibre oriented perpendicular to the tensile direction was tested at a synchrotron facility using a special loading rig which allowed for applying a load transverse to the fibre. Three distinguishable damage stages were observed: (i) interfacial debond initiation at the free surface, (ii) debond propagation from the surface into the specimen and (iii) unstable debonding along the full length of the scanned volume. The high resolution microtomography provides both qualitative and quantitative 3D data of the debonding initiation and propagation. Thus, microtomography is demonstrated as a promising technique which can assist micromechanical model development.

1. Introduction

The properties of the fibre/matrix interface strongly affect the macroscopic behaviour of composite materials. Macroscopic material properties as e.g. the interlaminar shear strength of composites can be highly sensitive to the fibre/matrix interface properties [1]. Fibres in laminas that are not oriented parallel to the primary loading direction can develop fibre/matrix debonding, which subsequently leads to matrix cracking and delamination. Therefore, understanding and control of the interface properties is of high importance for the development of new, improved composite materials. Sizing applied on the fibres surface allows for control of interface properties through proper chemical and physical fibre/matrix adhesion [2]. Microstructural optimization also requires tools for the characterisation of the interface properties to be used as input in micromechanical models for the predictions of the macroscopic composite properties.

Experimental characterisation of the fibre/matrix interfaces has been the object of several micromechanical studies. Various methods such as single fibre fragmentation test [3], single fibre pull out [3,4] or push out tests [5] have been developed. These methods are designed for the characterisation of the interfacial properties in terms of interfacial shear strength or a Mode II interface fracture toughness. However, these techniques do not provide means for determination of all parameters required for a complete interface characterisation. Due to the elastic mismatch between two different materials along an interface, a crack tip along the fibre/matrix interface is preliminary under mixed mode conditions [6,7]. This implies the presence of both normal and shear stresses ahead of an interface crack tip, and occurrence of both opening and shear displacements on the crack faces behind the interface tip. Furthermore, it has been established that the fracture toughness, G_c of bi-material interfaces strongly depends on the mode mixity, ψ, $G_c = G_c(\psi)$ [8]. Thus, the mixed mode fracture toughness of the fibre/matrix interface must be determined experimentally as input parameters required for micromechanical modelling.

In principle, studies of interfacial debonding of a single fibre under transverse load (Fig. 1) allow for the determination of the interfacial toughness as a function of mode mixity, $G_c = G_c(\psi)$. The mode mixity of the interfacial crack tip changes with debonding angle θ_d (Fig. 1), from dominant normal opening (Mode I) at $\theta_d = 0°$ and $\theta_d = 180°$ with respect to the applied load, approaching tangential-dominant opening (Mode II) at $\theta_d = 90°$. In other words, the mode mixity varies as a function of the debonding angle, $\psi = \psi(\theta_d)$ (Fig. 1).

Debonding of a single fibre under transverse load has been widely studied by numerical simulations [9–12]. Energy release rate and mode mixity were found as a function of debonding angle for both tensile and compression loads applied transversally to the fibre [12]. For debond angles above 60°, the crack tip is closed (Mode II) and a contact zone will be present near the debond crack tip. Subsequently, the crack growth is stable under pure Mode II [12]. The crack kinking out of the fibre/matrix interface into the matrix was also studied by a numerical modelling [9]. It was found that the most plausible debonding angle where kinking occurs is between 60° and 70°.

* Corresponding author. Tel.: +45 46775825.
E-mail address: karm@dtu.dk (K. Martyniuk).

1359-835X/$ - see front matter © 2013 Elsevier Ltd. All rights reserved.
http://dx.doi.org/10.1016/j.compositesa.2013.07.012

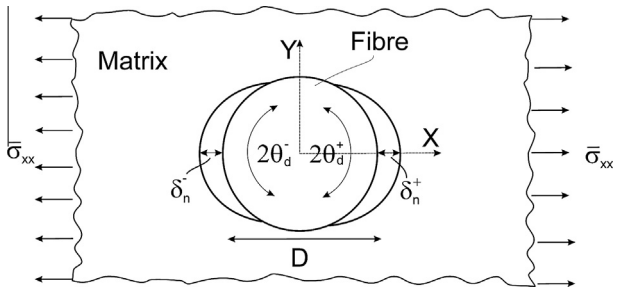

Fig. 1. Single fibre embedded in infinity matrix under transverse load (free-surface).

However, it appears that only few experimental studies have been conducted in order to verify the mode predictions presented above. Most of the reported experimental methods for investigation of a single-fibre under transverse load utilize optical microscopy for the debonding observations using a viewing direction perpendicular to the fibre direction [10,13,14]. This viewing direction is not well suited for the determination of the debonding angle, θ_d. Precise debonding angle measurements require the viewing from the fibre direction (Fig. 1). However, due to the complex stress state existing near the free surface of bi-material specimens [15], the crack is expected to initiate at this location and subsequently propagate along the fibre into the specimen. Therefore, in order to investigate whether the surface observations are representative for the behaviour further inside the specimen, it is necessary to study the initiation and evolution of the fibre/matrix debonding in 3D. Accurate measurements of debond angle, both at the free surface as well as inside the specimen, would allow not only for determination of the fracture toughness as a function of mode mixity, $G_c = G_c(\psi)$ but also for studies of the free edge effect.

In the present study, X-ray tomography is used to perform an investigation of the interfacial damage fracture process. X-ray tomography has been previously successfully applied to a variety of 3D studies of fracture of composites. As an example, Wright et al. [16] studied the damage onset and growth in carbon fibre-epoxy composite samples loaded in uniaxial tension by means of X-ray tomography. A similar set up to the one presented in the current paper was utilised by Rask et al. [17] for the study of damage initiation and propagation in natural fibre composites.

The purpose of the present study is to document the initiation and evolution of fibre/matrix interface debonding in 3D under transverse load and to investigate the potential of X-ray microtomography as a tool for providing quantitative data to be used in micromechanical modelling.

2. Materials and methods

2.1. Specimen manufacturing

Single fibre specimens were manufactured using E-glass fibres and epoxy resin (Epoxydharz HT 2, from Faserverbundwerkstoffe GmbH, Composite Technology). Glass fibres with diameter of ~50 μm were supplied by Ahlstrom Glassfibre, Finland. These fibres are significantly thicker than conventional glass fibres which typically have a diameter in the range of 10–20 μm [18], but the surface properties are expected to be the same. The thicker fibres were preferred in the present study in order to obtain larger crack openings.

The surfaces of the fibres were cleaned by tissue soaked in ethanol. Subsequently the fibres were positioned across rectangular rubber moulds. In order to reduce process-induced residual stresses each fibre was pre-strained by a weight of ~20 g [19,20]. The

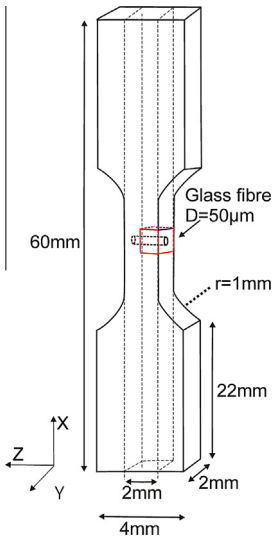

Fig. 2. A final sample geometry.

resin was degassed in vacuum in order to remove any air bubbles before being injected into the moulds. Curing was done at 40 °C for 24 h followed by a post-curing at 50 °C for 10 h. The sample surfaces of interest were polished, first manually using grinding paper SIC#1200 and SIC2400# (1 min each), then by automatic polishing using polishing cloths MD-Dac (applied force 55 N, suspensions: DP Blue and Dia Pro Dac 3 μm) and subsequently MD-Nap (50 N, DP Blue and Dia Pro Dac 1 μm). The total polishing time at each step was 5–15 min depending on the polished surface quality which was frequently checked using optical microscopy. Polished rectangular shaped samples (marked with dashed line in Fig. 2) were reshaped into dog-bone shaped tensile test specimens in order to facilitate subsequent mechanical testing. The reshaping was conducted by placing the rectangular samples in dog-bone shaped moulds and refilling the free space in the mould with the resin. In order to protect the polished surfaces, they were covered by tape before being placed into the dog-bone shaped moulds. Curing and post-curing processes were then repeated and the tape was removed from the polished surfaces. The final geometry of the sample is showed in Fig. 2. Eventually aluminium tabs were glued at each end of the specimen in order to facilitate mounting in the X-ray loading fixture (Fig. 3).

2.2. Preliminary tests

Preliminary tensile tests were performed prior to the synchrotron experiments in order to test if the specimens develop damage in the expected way and to identify suitable load steps for *in situ* tests at the synchrotron facility. Step wise tensile tests were conducted inside the chamber of a scanning electron microscope (SEM) (Zeiss, EVO60) using a custom made loading fixture [21]. The load was converted to a nominal stress, $\bar{\sigma}_{xx}$, calculated as the applied force divided by the cross sectional area of the specimen gauge section. At each load step (applied with an increment of ~2 MPa) the displacement was held fixed for 30 min (the expected time for scanning at the synchrotron facility). During the 30 min, the load decreased gradually to ~70% of the initial value, possibly due to creep in the polymer matrix. The debonding initiation was observed to occur at nominal stress of $\bar{\sigma}_{xx} \sim 5$ MPa. At this stress level the maximum normal opening in the tensile direction, δ_n (Fig. 1), was in the range of 1 pixel which in the acquired SEM micrographs corresponds to ~0.1 μm. The spatial resolution of the X-ray tomography images presented in the present paper is

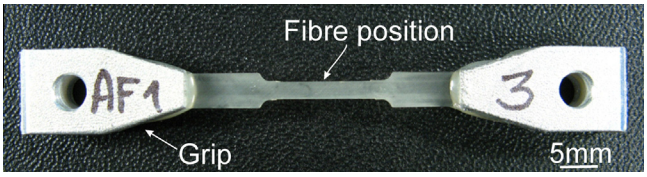

Fig. 3. The final test specimen. Aluminium tabs glued at the ends of the mode-composite to facilitate the loading of the specimen in the loading fixture.

limited to a voxel size of 0.74 μm. Thus, openings in the range of 0.1 μm are assumed to be undetectable by microtomography. It was therefore concluded, that the load which would cause the damage detectable by tomography images must be higher than the one which caused the visible debonding in the SEM observations.

During the preliminary SEM testing interfacial crack kinking into the matrix was observed at the stress level of $\bar{\sigma}_{xx} \sim 15$ MPa. The crack kinked at angle of $2\theta_d \sim 130°$ with respect to the applied load and propagated further in the matrix during subsequent load steps. The kinking evolution was accompanied by further interface debonding above the angle of kinking. After subsequent load steps more kinked cracks were observed around the interface. The debonding evolution and subsequent kinking phenomenon observed in the SEM testing is shown in Fig. 4.

2.3. Tensile test procedure

A custom-made loading rig for synchrotron *in situ* tensile tests was used in the experiments. Its design is similar to that of Wright et al. [16], with an additional assisting tower for sample mounting (Fig. 5). The tower allows for an easier mounting of the test specimen and enables the placing of an acoustic emission (AE) sensor on the specimen without inducing any load to the specimen (Fig. 5). The novel parts of the device are shown in Fig. 5. The remaining parts of the loading rig is as described by Wright et al. [16]. The weight of the entire rig is 1.5 kg. The rig has a built-in load cell with a capacity of 1.5 kN. The load is induced manually by turning a hex screw placed on the top of the fixture. The experiments were thus conducted under fixed grip condition. An AE sensor (Pico sensor, Physical Acoustic Corp., Princeton) was attached to the specimen by a small clip without applying any couplant. The AE system was used during some of tests to assist the detection of damage initiation/propagation. The threshold of the AE system was set to 30 dB. The loading was interrupted when AE events were recorded. Otherwise, the loading was increased stepwise with the increment of ~5–10 MPa scheduled based on the SEM observations in the preliminary tests. The load steps employed in the X-ray testing must have been bigger than those applied in SEM observations, so that the damage process could have been observed throughout all stages within the limited beam time. Besides, it was expected that due to the limited X-ray images resolution, the damage propagation caused by smaller load steps would not be visible. AE data was acquired only while loading.

At each load step, after applying the nominal stress, the sample was unloaded by ~30% in order to minimize deformation due to creep and to prevent damage evolution during the scanning time. In the remainder of this paper, we will report the maximum applied stress of a given load step, i.e., the applied stress before unloading. Assuming linear elastic material behaviour during unloading, the reported displacements are thus expected to be ~30% lower than they were at the nominal stress.

The initial load step during *in situ* synchrotron tests was set to a nominal stress of $\bar{\sigma}_{xx} \sim 10$ MPa. According to the SEM observations of the preliminary tests, due to the limitation of the X-ray images, no damage is expected to be detectable at this load level.

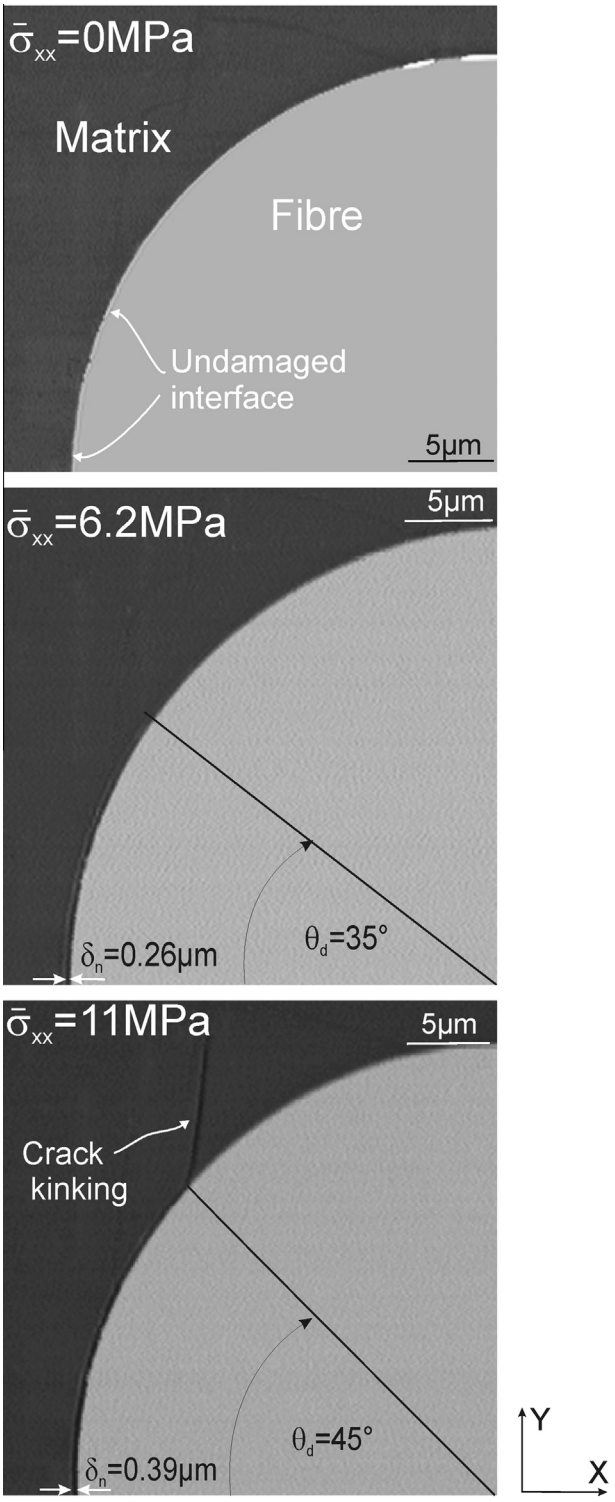

Fig. 4. Debonding sequence and the interfacial crack kinking observed in the SEM.

2.4. Beamline and data acquisition

The *in situ* microtomography tensile tests were performed at the TOMCAT beamline of the Swiss Light Source, Switzerland. The samples were mounted in the tensile rig at a distance of 128 mm from the CCD camera, which means that the data was ac-

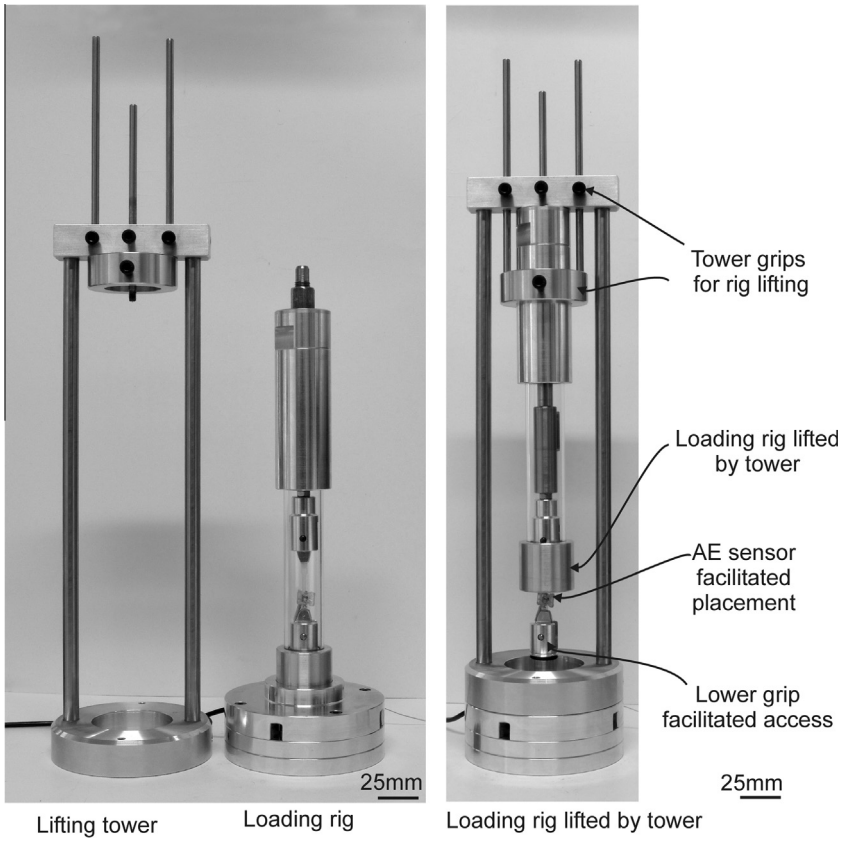

Fig. 5. Lifting tower designed for the *in situ* tests at synchrotron facility.

quired in the so-called 'edge enhanced' tomography mode [22]. Samples were scanned using an X-ray beam with photon energy of 20 keV and an exposure time of 350 ms per projection. In total 1601 projections were acquired during a rotation through 180° in equal angle increments. In total 2048 slices were collected at each load step with a voxel size of 0.74 × 0.74 × 0.74 μm. To allow for high resolution imaging of the fibre/matrix interface, local tomography was utilised. Thus, a volume of 1.5 mm × 1.5 mm × 1.5 mm was scanned. This corresponds to approximately half of the samples thickness in the *z*-direction. The scanned volume is marked with red lines in Fig. 2.

The mentioned above parameters chosen for the X-ray tomography experiments ensured sufficient contrast to differentiate between the polymer matrix material and the glass fibre, as well as to observe the development of cracks. In order to analyse the acquired tomography data, 3D volumes as well as representative 2D projections were investigated using the commercial Avizo software package [23].

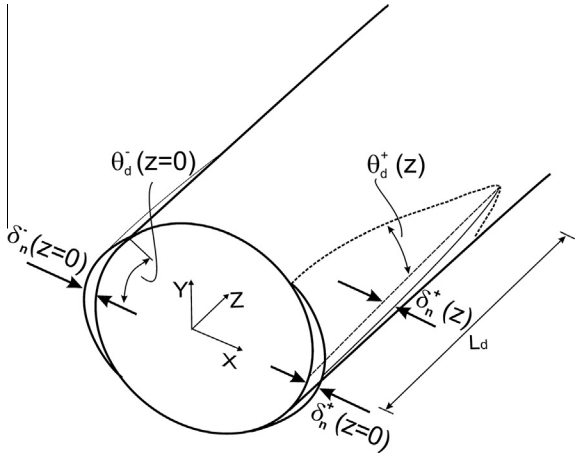

Fig. 6. Nomenclature used for 3D debond profiles.

3. Results

3.1. Overview of damage evolution

The debond profiles observed in the experiments will be presented by measured debond angles, $2\theta_d$ and normal openings, δ_n along the fibre (in *z*-direction) (see nomenclature in Fig. 6).

Fig. 7a shows an example of 2D planes for both the free surface (*x*, *y*-plane), and an internal plane (*x*, *z*-plane) of the test specimen at the initial load step of $\bar{\sigma}_{xx} = 10$ MPa. No interfacial debonding can be observed at this stage. A debond crack was detected at the free surface at a nominal stress $\bar{\sigma}_{xx} = 17.8$ MPa (Fig. 7b) and the damage was observed to evolve at each subsequent load step (Fig. 8). The debond angle at the free surface (defined in Fig. 6) reached $2\theta_d \sim 140°$ at a nominal stress of $\bar{\sigma}_{xx} = 42.5$ MPa (Figs. 8 and 9) and normal opening reached $\delta_n \sim 16$ μm. At this stage, the detected crack tip of the debond crack in the depth direction (*z*-direction), denoted L_d (see Fig. 6), reached $L_d^- \sim 106$ μm (Fig. 11). Subsequently, at $\bar{\sigma}_{xx} = 44.2$ MPa the debond crack had propagated unstably in the *z*-direction along the full length of the scanned volume (Figs. 12 and 13). The debond angle, $2\theta_d(z)$, and the maximum normal opening, $\delta_n(z)$, inside the sample were found to remain the same all the way through the scanned volume (Figs. 12–15).

Most of the detected AE events had low amplitude in the range of 40–55 dB. According to the reported studies on AE used in

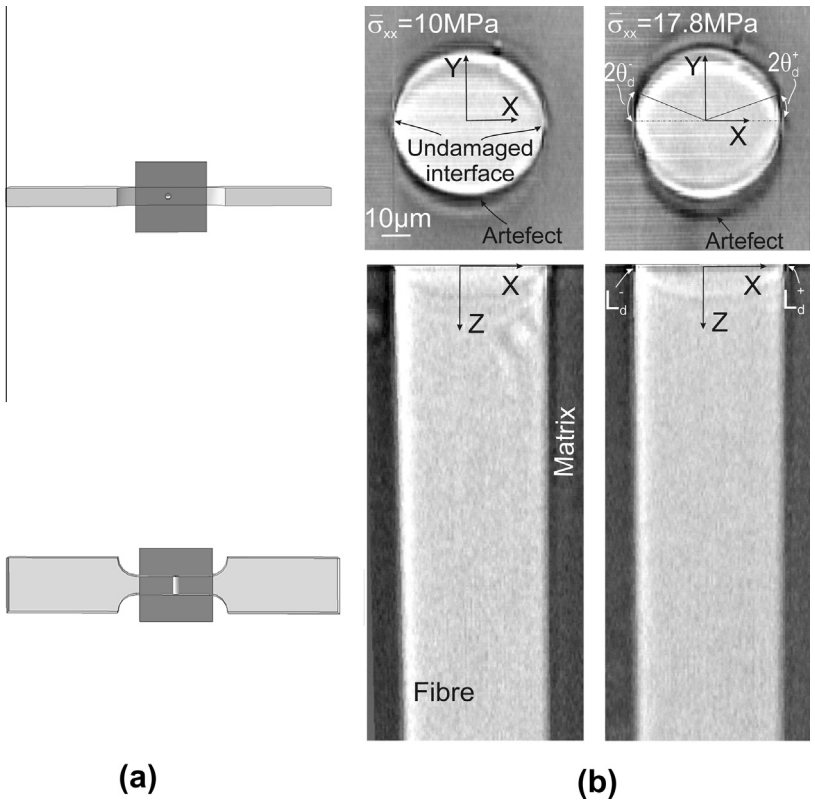

Fig. 7. Interfacial debonding initiation on the free surface; 2D slices for two initial load steps: (a) undamaged microstructure at nominal stress of $\bar{\sigma}_{xx} = 10$ MPa, (b) debonding initiation at the free surface at $\bar{\sigma}_{xx} = 17.8$ MPa x, y-plane corresponds to free surface and x, z-plane corresponds to the internal plane along $\theta_d = 0$–$180°$ normal to x, y-plane as indicated in (a).

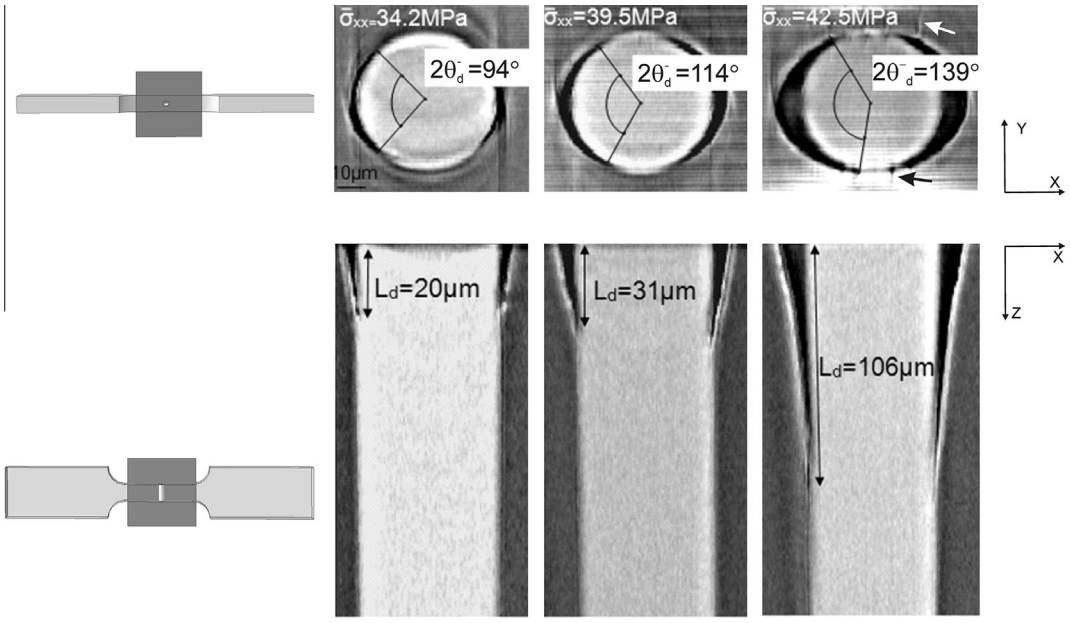

Fig. 8. Interfacial damage sequence; 2D slices for three final load levels: (a) $\bar{\sigma}_{xx} = 34.2$ MPa, (b) $\bar{\sigma}_{xx} = 39.5$ MPa and (c) $\bar{\sigma}_{xx} = 42.5$ MPa. x, y-plane corresponds to free surface and x, z-plane corresponds to the internal plane along $\theta_d = 0°$–$\theta_d = 180°$ normal to x, y-plane as indicated in Fig. 5a.

microscale tests of composites, AE signals with amplitudes in this range are associated mainly with fibre/matrix debonding or matrix plastic deformation [24]. Therefore, it is believed that most of the acquired AE signals in the present study were caused by the initiation/propagation of the debond crack in the sample. However, in some cases crack growth was observed in tomography images without accompanying AE signals.

Based on the 3D *in situ* observations, the fibre/matrix interfacial debonding can be divided into three distinguishable stages: (i) fibre/matrix interfacial debond initiation at the free surface, (ii) pro-

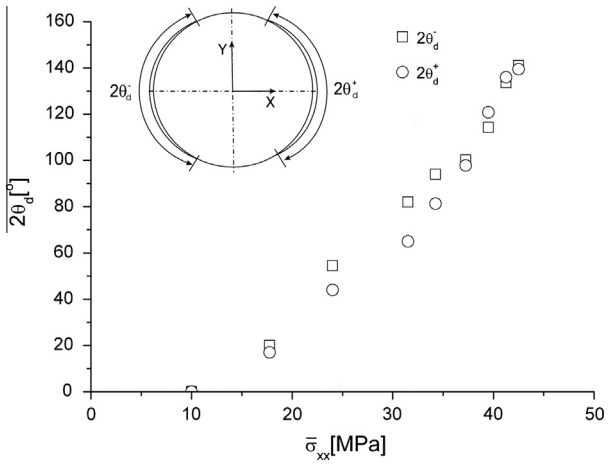

Fig. 9. Free surface debond angle, $2\theta_d$ as a function of applied stress.

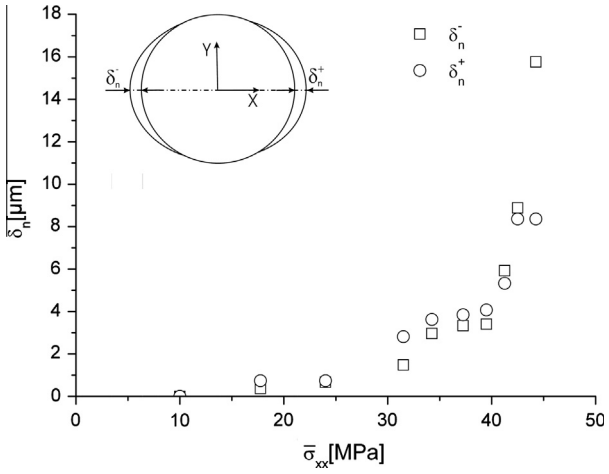

Fig. 10. Normal opening on the free surface for different load steps for two debonding positions.

gressive debonding at the free surface as well as along the fibre, and (iii) debond crack tunnelling.

3.2. Fibre/matrix interfacial debond initiation

Interfacial debonding initiation was detected at the free surface of the sample at a nominal stress of $\bar{\sigma}_{xx} = 17.8$ MPa. Debonding was observed at two positions simultaneously, at angles $\theta_d = 0°$ and $\theta_d = 180°$ with respect to applied load direction (Figs. 1 and 7b). The sample is symmetric about the $x = 0$ plane. It is therefore of interest to study if the debonding develops symmetrically. All measurements of the debond profiles including the debond angle, $2\theta_d$, the maximum normal opening, δ_n, and the maximum debond depth, L_d will be distinguished in the remainder of this paper between the two sides of the fibre, by using superscripts + and −, for position $\theta_d = 0°(x > 0)$ and $\theta_d = 180°(x < 0)$ with the respect to the applied load respectively (Fig. 6). The initial stage of debonding was found to develop symmetrically. For both debond initiation positions ($\theta_d = 0°$ and $\theta_d = 180°$) the measured debond angle was

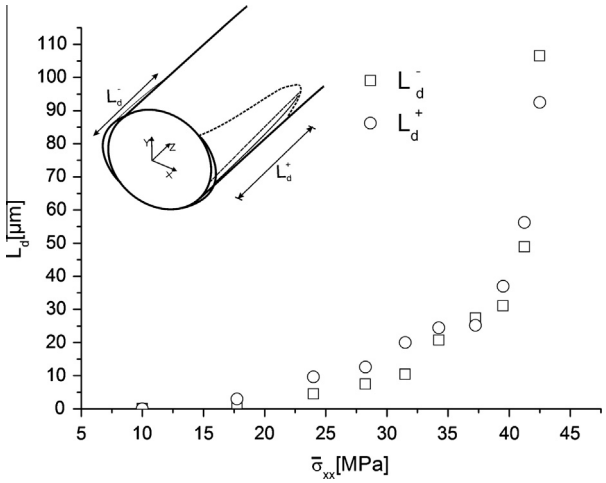

Fig. 11. Debond depth L_d as a function of applied stress.

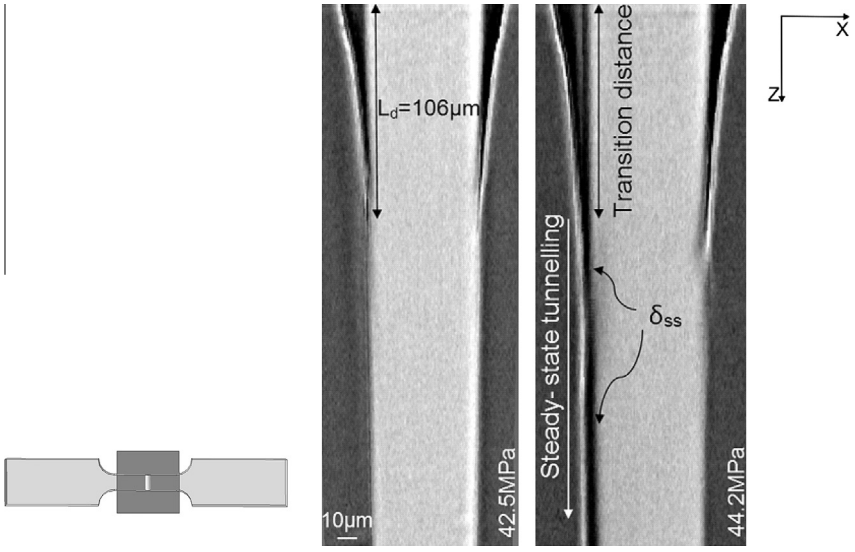

Fig. 12. Steady-state interfacial crack tunnelling-transition from stable crack growth to steady-state crack tunnelling; x, z-plane corresponds to the internal plane along $\theta_d = 0°$–$\theta = 180°$ normal to x, y-plane as indicated in Fig. 7a.

$2\theta_d \sim 18° \pm 1°$ (Fig. 7b). The normal openings at a nominal applied stress of $\bar{\sigma}_{xx} = 17.8$ MPa reached $\delta_n^+ \approx \delta_n^- \approx 0.74\mu m$.

3.3. Progressive interfacial debonding

At subsequent increasing load levels, both the debond angle at the free surface and the debond depth along the fibre (z-direction) were observed to increase after each load step (Fig. 8).

The growth of the debond angle at the free surface over the whole loading process, for both sides of the fibre, denoted as $2\theta_d^-$ and $2\theta_d^+$ (Fig. 1), is presented in Fig. 9. The increase of the debond angle observed by X-ray microtomography seems to be rather stable and symmetric for both sides. A slight difference of the debonding angles, $2\theta_d^-$ and $2\theta_d^+$, is observed only for few load steps. A maximum value of $2\theta_d \sim 140°$ was reached at the free surface of the sample at the nominal stress of $\bar{\sigma}_{xx} = 42.5$ MPa (Figs 8c and 9). Up to this load level, the normal opening at the free surface evolves in a rather symmetric manner on both sides (designated as δ_n^- and δ_n^+) as well (Fig. 10).

The maximum debond depth, L_d is shown as a function of the nominal applied stress, $\bar{\sigma}_{xx}$, in Fig. 11 for both sides of the fibre (L_d^-, L_d^+). The debond is seen to develop fairly symmetrically along the fibre until the load level of $\bar{\sigma}_{xx} = 42.5$ MPa. The maximum debonding depth, L_d^- reaches 106 μm just before the onset of unstable debonding. This debonding depth corresponds to ~2 fibre diameters ($2 \times D$).

According to the surface observations of the preliminary SEM tests, at the stress level of $\bar{\sigma}_{xx} \sim 15$ MPa the interfacial crack had kinked into the matrix. Thereby, it is believed that several kinking cracks are likely to have formed around the interface in the sample which was loaded up to $\bar{\sigma}_{xx} = 42.5$ MPa during the *in situ* tomography experiments. However, at low stress levels the kinking cracks were difficult to detect in the tomography data due to their small size. Only at the final load steps, ($\bar{\sigma}_{xx} > 42.5$ MPa), the kinked cracks were visible in tomography images near to the free-surface of the sample as pointed with arrows in Fig. 8c. The crack kinking was found to be a free-surface phenomenon observable only down to $z \sim 10$ μm. Therefore, it is believed that interfacial kinked cracks do not influence the interior debond profiles which is the focus of this study.

3.4. Interfacial crack tunnelling

The transition to unstable growth of a crack with constant width is similar to tunnelling cracking of constrained layers [25]. A steady-state is reached when the tunnel front is assumed to maintain its shape as it advances and the energy released does not depend on the crack length [25,26].

3D volumes presenting interfacial damage evolution including transition to debond tunnelling observed at $\bar{\sigma}_{xx} = 44.2$ MPa are showed in Fig. 13. For better visualisation, the matrix is rendered invisible.

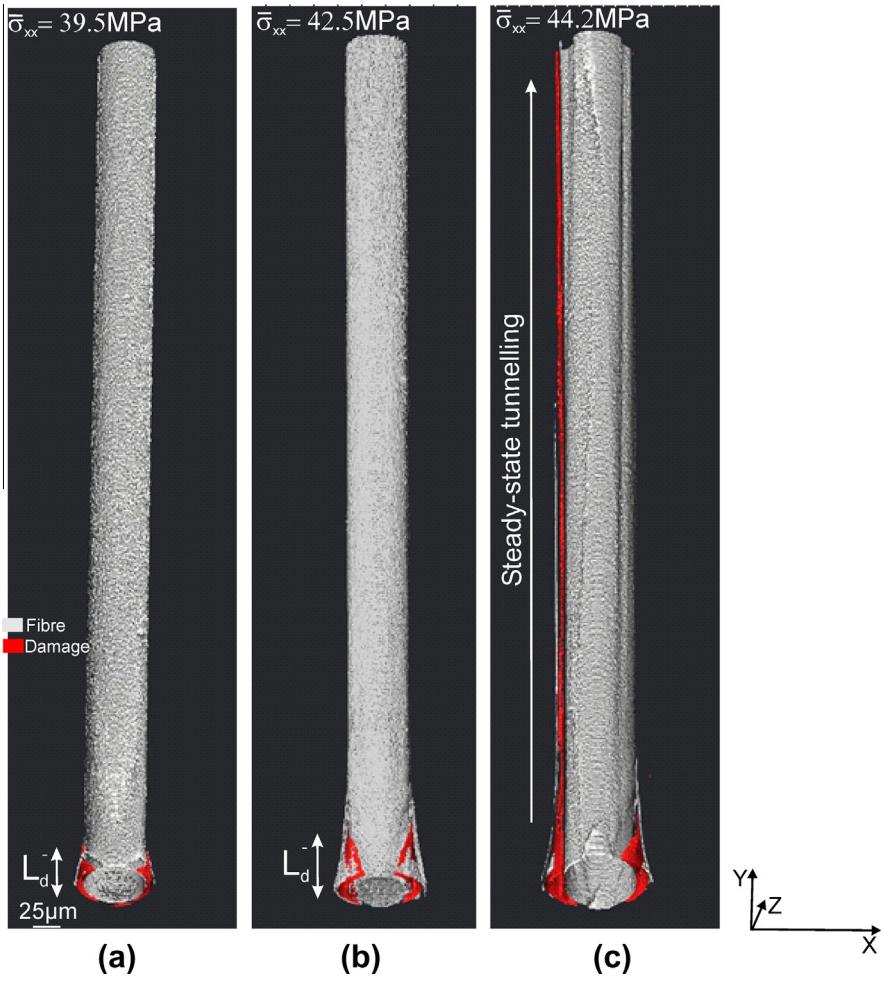

Fig. 13. 3D visualisation of interfacial progressive debonding for final three load levels: (a) $\bar{\sigma}_{xx} = 39.5$ MPa, (b) $\bar{\sigma}_{xx} = 42.5$ MPa and (c) $\bar{\sigma}_{xx} = 44.2$ MPa (debonding tunnelling).

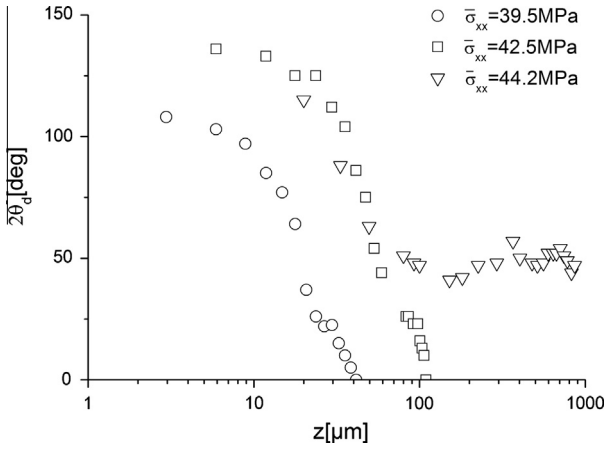

Fig. 14. Internal debonding angle $2\theta_d$ as a function of distance from the free surface for three different load steps including steady-state tunnelling.

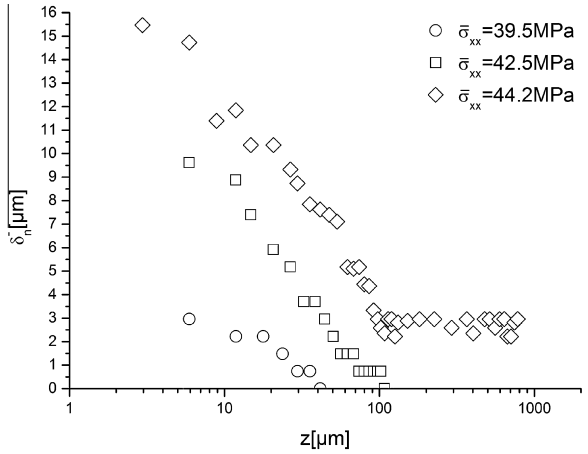

Fig. 15. Normal opening evolution along the fibre.

Fig. 14 shows the debond angles along the fibre, $2\theta_d^-(z)$, for the final load steps, measured using tomography data. After the transition at the final load step of $\bar{\sigma}_{xx} = 44.2$ MPa (Fig. 12), for this load level the debond profile for $z > 106$ μm remains the same along the fibre. The steady state debond angle, $2\theta_{ss}$ (the steady state debond angle is defined in Fig. 16c) remained at the level of $2\theta_{ss} \sim 48°$ (Fig. 14) and normal opening (labelled δ_{ss} in Fig. 12) remained at the level of ~3 μm (Fig. 15).

Asymmetry in the normal opening at the free surface at the transition load step to the tunnelling stage is visible in Figs. 10 and 12. The normal opening at the free surface ($z = 0$) reached δ_n^- ~16 μm (at $\theta_d = 180°$), whereas on the other side of the fibre (at $\theta_d = 0°$), the normal opening reached only δ_n^+ ~9 μm. Both of the normal openings at the free surface are much larger than the opening observed inside the sample at the tunnelling stage ($\delta_{ss} \sim 3$ μm for $z > 106$ μm). The difference between the free surface observations and those inside the specimen is visible in the debond angles as well. The debond angles observed at the free surface reached $2\theta_d \sim 140°$ (Fig. 9) whereas the debond angle at the tunnelling stage ($\bar{\sigma}_{xx} = 44.2$ MPa), inside the specimen ($z > 106$ μm), for this load step remains at the level of $2\theta_{ss} \sim 48°$ (Fig. 14).

3.5. After-scanning observations

Protrusion of the partially debonded fibre out of the matrix was observed in the X-ray images after each load step. Since the sample was unloaded only by 30% of nominal load after each load step, this behaviour was expected due to the matrix contraction (Poisson's effect) caused by the applied external load. However, the fibre protrusion after the load steps from $\bar{\sigma}_{xx} = 39.5$ MPa to $\bar{\sigma}_{xx} = 44.2$ MPa seems to be large in comparison with those of the previous loading steps. Once the tomography testing was finished, local shape changes of the sample in the position of the scanned volume were visible to the naked eye. Moreover, a colour change was observed in the scanned volumes of the tested samples. Samples that had been exposed to the X-rays for longer time were found to have a much more intensive colour change of the scanned volume than those with shorter scanning times. The possible implications of these observations will be discussed in the next section.

4. Discussion

4.1. Testing approach

Based on previous studies on composite materials it was initially assumed that X-ray tomography as a non-destructive testing method does not have significant influence on the materials properties. However, the observed fibre protrusion and the colour change observed after the scanning suggest that potentially X-rays may damage the samples. Since the intensity of the colour change seems to be related to the exposure time of the samples, it seems plausible that the observed large fibre protrusions were caused by inelastic matrix contraction which could be caused by the X-rays. This hypothesis requires further investigations. The scanning time should be minimized during *in situ* mechanical tests of polymer composites at synchrotron facilities in order to decrease the risk of radiation damage. The X-rays influence on the composites being under external load could be revealed by the studies of several scanning energies and exposure times of the polymer composites being under external load.

4.2. Fibre/matrix interface debond initiation

The fibre/matrix interfacial debonding was first observed in the tomography data at an applied stress level of $\bar{\sigma}_{xx} = 17.8$ MPa. It is recognized that the damage observed at this load level can be considered as the damage initiation only for this particular X-ray tomography resolution. Although it can be shown that using 'edge enhanced' tomography allows for detection of crack openings smaller than the voxel size [27], the quantification of crack openings is for most practical applications limited by the voxel resolution, i.e. in the present case to ~0.74 μm. Nevertheless, the presented observations show that the damage initiation takes place at the free surface of the sample. It is recognized, that the size of the debond (especially the debond normal opening), might be influenced by the fibre diameter and the matrix's elastic properties. The elastic modulus of the epoxy resin used in this study is E_m = 3 GPa (data provided by the manufacturer). Using different epoxy may influence the debond size/shape. Likewise, the fibre diameters is expected to influence the debond size. The further investigation should be carried out to address these assumptions. Likewise, the kinking is identified to be a surface phenomenon. Therefore, this study shows that investigations of damage initiation and crack kinking could be well accomplished by 2D *in situ* observation carried out e.g. in the chamber of a SEM. The analysis of damage initiation and kinking cracks in the matrix will be the topic of a subsequent paper dealing with 2D observations.

4.3. Fibre/matrix interface debond evolution

This study shows that, unlike the debond initiation the characterisation of the debond evolution requires 3D observations.

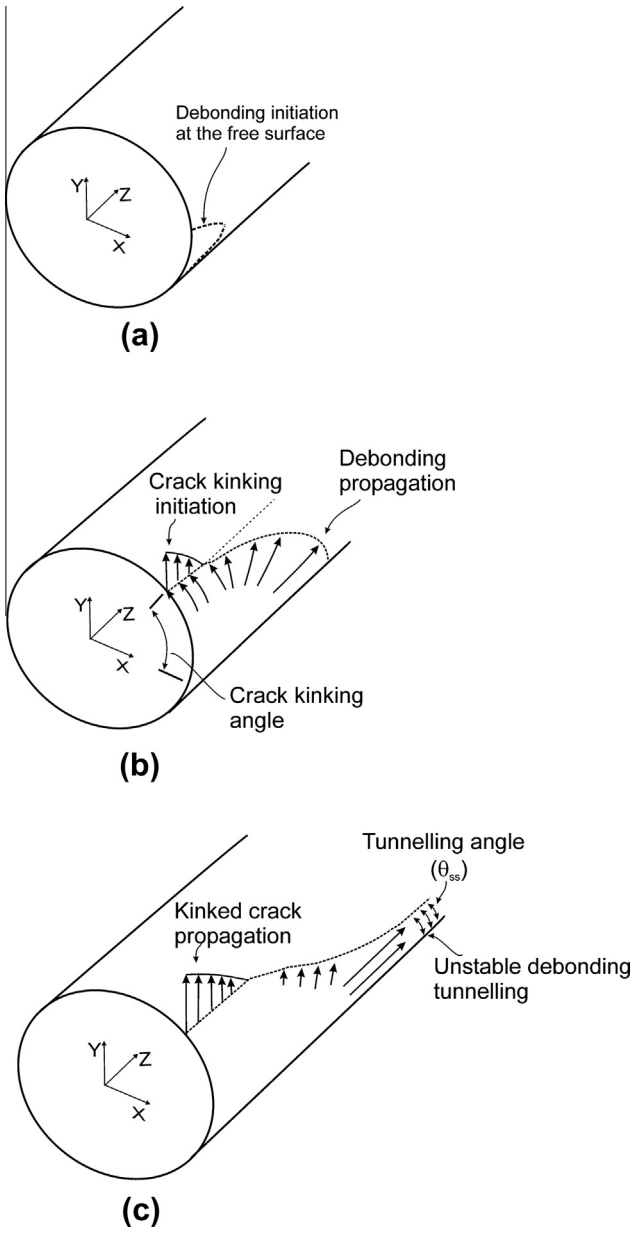

Fig. 16. Schematic 3D interface debonding sequence of a single fibre under transverse load applied in the *x*-direction: (a) debonding initiation at the free surface, (b) debonding propagation and interface crack kinking and (c) unstable debond tunelling.

Following the debond initiation at the free surface, interface crack propagation away from the free surface ($z > 0$) along the fibre was observed after each subsequent load step. 3D observations allowed for the comparison of the debond crack opening profiles at the free surface with those inside the specimen. A significant difference was observed. The debond angle at the free surface of the sample ($z = 0$), reached $2\theta_d \sim 140^\circ$ with a maximum normal opening, $\delta_n \sim 16$ μm. The measured debond angles and openings inside the specimen were much smaller than those at the free surface as seen in Figs. 12–15. It is believed that the difference is caused by uneven stress states at the free surface and in the interior of the specimen as well as by the interfacial kinked crack being present only near the surface.

The kinking phenomenon was studied by numerical simulations [9] and it was predicted that crack kinking should occur when the debond angle reaches $2\theta_d \sim 130$–140° [9]. This prediction is in good agreement with preliminary SEM observations. This supports the hypothesis that the kinking phenomenon is related to a critical debond angle. However, inside the specimen, for $z > 10$ μm, the debond crack does not reach the critical debonding angle and therefore kinking does not occur. The clear difference of the interfacial fracture process at the free surface and inside the specimen illustrates the importance of 3D studies. However, the colour and geometry change of the scanned volume indicates possible influence of the X-rays on the sample and therefore should not be neglected when referring to the measured features. If those visual changes are due to radiation damage, it should be investigated to what extend the difference between free edge debonds profiles and interior debonds could be related to such radiation damage. Moreover, the sample preparation process which includes grinding and polishing of the free surfaces using different lubricants might also influence the interface properties at the free surface, so that they may differ from the interface properties further inside the specimen.

4.4. Debond tunnelling

The tunnelling cracking was detected at a load level of $\bar{\sigma}_{xx} = 44.2$ MPa after the debond depth had reached $L_d \sim 106$ μm. The fibres used in the sample have a diameter of $D \sim 50$ μm which means that the debond tunnelling was attained when the debond depth exceeded the distance equal to two fibres diameter, $L_d \sim 2 \times D$ (Figs. 11 and 12). Modelling has shown that for crack tunnelling in plane layers the energy release rate is attained after the tunnel length exceeds a few times the layer thickness [25,26]. Since it is believed that the provided data is accurate within approximately 1 μm, it can be concluded that the observed phenomenon of a curved tunnelling crack is consistent with the theory for straight tunnelling cracks [25]. For further investigation of this phenomenon, a variety of fibres with different diameters could be tested to study the influence of fibre diameter on the energy release rate. It is expected that debonding should occur at a lower applied stress for the thicker fibre diameter, since energy release rate is expected to scale linearly with the fibre diameter [9].

4.5. 3D experimental data for micromechanical modelling

The data obtained from the *in situ* microtomography tests are both qualitative and quantitative and thereby useful for micromechanical model development. 3D X-ray microtomography data has already been successfully utilised for model development by Wright et al [16]. In the results presented in the current paper, the 3D debond profiles are described by debond angles, normal openings and debond depth. The resolution of the presented data allows only for detecting the crack openings that are approximately 1 voxel size in magnitude in the normal opening. Consequently, the crack tip positions reported in the present study are "apparent" crack tip positions, i.e. the locations where the crack opening in a direction normal to the crack is approximately 0.74 μm. Due to the mixed mode conditions of the interfacial crack tip, which involves normal as well as tangential crack openings, the accuracy of the debond angle measurements is assumed to be lower than the estimated accuracy based on the microtomography spatial resolution (~1 μm). In particular under dominated tangential opening (Mode II), which according to the numerical simulations occurs when the debonding angle reaches $2\theta_d \sim 120^\circ$ [12]. The tangential (shear) opening displacements cannot be determined by the proposed experimental set up. Experimentally, tangential displacements could be obtained by e.g. identifying particles spread in the sample and tracking their displacements after each loading step [28]. However, the maximum normal openings (at $\theta_d = 0^\circ$ and $\theta_d = 180^\circ$ with respect to the applied load,

Fig. 1), obtained from the presented experiments, are measured within the accuracy of approximately 1 μm. Therefore, the measurements of normal openings presented in this paper can be considered as more precise than the measured debond angles. By comparison of the normal openings obtained in the present study with those obtained by numerical simulations, the relevant microscale parameters could be determined. Moreover, by a coupled experimental/numerical approach the difference of the debonding profiles observed at the free surface and inside the sample could be investigated. If similar differences between interior debond profiles and those at the free surface are obtained in numerical simulations as for experiments, the manufacturing as well as possible radiation damage are likely not to have influenced the experimental results significantly. However, the debond crack kinking should be taken into account in the numerical modelling. It must be noticed, that kinking observed in the experiments might have an influence on the debond profiles close to the free surface ($z \sim 10$ μm). Therefore, results presented in this study should be rather used for model validation considering only the interior debond profiles (away from free surface).

A cohesive-zone finite element model is currently under development to address such issues and numerical predictions will be compared with the results presented in the current paper. At this stage, the elastic behaviour is assumed and therefore, it is believed that the applying of the external load in one step would result in the same debonding as the one observed in tomography. This can be verified in the numerical modelling. The fracture parameters of the fibre/matrix interface are expected to be obtained by coupled experimental and numerical studies. The interfacial mixed-mode strength, the fracture energy, and the interfacial cohesive law parameters will be identified.

5. Summary of fibre/matrix interface debonding observations

Combining the 2D observations from the preliminary SEM tests and the 3D tomography data we can get a picture of the evolution of the fibre/matrix debonding process. Interfacial debonding initiates at the free surface at the location of the tensile direction ($\theta_d = 0°$ and $\theta_d = 180°$) as shown schematically in Fig. 16a. With increasing applied stress, the debonding evolves from the free surface, both along the fibre (the z-direction) and around the interface (increasing the debonding angle, $2\theta_d$). The debond angle is found to be the largest at the free surface ($z = 0$). When the debond angle at the free surface reaches a critical value of $2\theta_d \sim 130°$, the crack kinks out of the interface into the matrix (Fig. 16b). Since at the final load step the debond angle attains this critical angle only close to the free surface of the sample ($0 < z < 10$ μm) (Fig. 14), the crack kinking is only a surface phenomenon at this load level. With increasing applied stress the debond crack front propagates unstably into the specimen and the debond profile remains the same all the way through the scanned volume (tunnelling) (Fig. 16c).

6. Conclusions

Progressive fibre/matrix interfacial debonding was studied in 3D using X-ray microtomography. The debonding was found to initiate at the free surface and propagate inside the sample attaining an unstable crack tunnelling. The tomographic images allowed for quantification of the debond crack profiles by measured the debond angles, the normal openings and interfacial crack depth. The ability of X-ray tomography to provide detailed parameters for quantification of 3D debonding process makes it a promising tool for generating data for 3D micromechanical modelling. Disadvantages of the technique, caused mainly by limited resolution, have been assessed. The advantages and importance of 3D *in situ* observations have been presented by showing the difference between the debond evolution at the free surface and that inside the specimen. Further investigations should be carried out to study influence of X-ray radiation on polymer composites being under external load.

Acknowledgements

The authors would like to thank to the staff at the TOMCAT beamline for technical assistance as well as PSI for granting the beam time. We thank Mr. Jukka Koulu from Ahlstrom Glassfibre, Finland for providing glass fibres for samples manufacturing, as well as Malcolm McGugan, Stergios Goutianos, Jens Olsson and Erik Vogeley for their help with the test set up. Research technicians Jonas Kreutzfeldt Heininge, Christian H. Madsen from DTU Wind Energy and Steen Johannes Bang from DTU Energy Conversion and Storage, Technical University of Denmark, Risø Campus are thanked for the help with specimen preparation. Dr. Qingda Yang is acknowledged for inspiring discussions. The research leading to these results has received funding from the Danish Agency for Science, Technology and Innovation. The Danish Research Council is thanked for travel support (via Danscatt).

References

[1] Blanco C, Casal E, Granda M, Menéndez R. Influence of fibre–matrix interface on the fracture behaviour of carbon-carbon composites. J Eur Ceram Soc 2003;23:2857–66.
[2] Larson BK, Drzal LT. Glass fibre sizing/matrix interphase formation in liquid composite moulding: effects on fibre/matrix adhesion and mechanical properties. Composites 1994;25:711–21.
[3] Zhandarov SF, Pisanova EV. The local bond strength and its determination by fragmentation and pull-out test. Compos Sci Technol 1997;57:957–64.
[4] Kerans RJ, Parthasarathy TA. Theoretical analysis of the fiber pullout and pushout tests. J Am Ceram Soc 1991;74:1585–96.
[5] Watson MC, Clyne TW. The tensioned push-out test for fibre–matrix interface characterisation under mixed mode loading. Mater Sci Eng A 1993;160:1–5.
[6] Hutchinson JW, Suo Z. Mixed mode cracking in layered materials. Adv Appl Mech 1992:63–191.
[7] Hutchinson JW. Mixed mode fracture mechanics of interfaces. Metal–Ceram Acta – Scripta Metall Proc Ser 1990;4:295–306.
[8] Liechti KM, Chai YS. Asymmetric shielding in interfacial fracture under in-plane shear. J Appl Mech 1992;59:295–304.
[9] París F, Correa E, Mantič V. Kinking of transversal interface cracks between fiber and matrix. J Appl Mech 2007;74:703–16.
[10] Koyanagi J, Shah PD, Kimura S, Ha SK, Kawada H. Mixed-mode interfacial debonding simulation in single-fiber composite under a transverse load. J Solid Mech Mater Eng 2009;3:796–806.
[11] Correa E, Mantič V, Paris F. A micromechanical view of inter-fibre failure of composite materials under compression transverse to the fibres. Compos Sci Technol 2008;68:2010–21.
[12] París F, Correa E, Cañas J. Micromechanical view of failure of the matrix in fibrous composite materials. Compos Sci Technol 2003;63:1041–52.
[13] Correa E, Gamstedt EK, París F, Mantič V. Effects of the presence of compression in transverse cyclic loading on fibre–matrix debonding in unidirectional composite plies. Compos Part A: Appl Sci Manuf 2007;38:2260–9.
[14] Meurs PF, Schrauwen BAG, Schreurs PJ, Peijs T. Determination of the interfacial normal strength using single fibre model composites. Compos Part A: Appl Sci Manuf 1998;29:1027–34.
[15] Bogy DB. Two edge-bonded elastic wedges of different materials and wedge angles under surface tractions. J Appl Mech 1971;38:377–86.
[16] Wright P, Moffat A, Sinclair I, Spearing S. High resolution tomographic imaging and modelling of notch tip damage in a laminated composite. Compos Sci Technol 2010;70:1444–52.
[17] Rask M, Madsen B, Sørensen BF, Fife JL, Martyniuk K, Lauridsen EM. In situ observations of microscale damage evolution in unidirectional natural fibre composites. Compos Part A: Appl Sci Manuf 2012;43:1639–49.
[18] Brøndsted P, Lilholt H, Lystrup A. Composite materials for wind power turbine blades. Annu Rev Mater Res 2005;35:505–38.
[19] Zhu Q, Geubelle PH, Li M, Tucker CL. Dimensional accuracy of thermoset composites: simulation of process-induced residual stresses. J Compos Mater 2001;35:2171–205.
[20] Tanoglu M, Ziaee S, Mcknight SH. Investigation of properties of fiber/matrix interphase formed due to the glass fiber sizings. J Mater Sci 2001;36:3041–53.
[21] Sørensen BF, Horsewell A, Skov-Hansen P. In situ observations of crack formation in multi-filament Bi-2223 HTS tapes. Physica C 2002;372–376:1032–5.

[22] Stampanoni M, Groso A, Isenegger A, Mikuljan G, Chen Q, Bertrand A, et al. Trends in synchrotron-based tomographic imaging: the SLS experience. Proc SPIE 2006;6318. 63180M–63180M–14.
[23] http://www.vsg3d.com/avizo/overview.
[24] Ageorges C, Friedrich K, Schüller T, Lauke B. Single-fibre Broutman test: fibre–matrix interface transverse debonding. Compos Part A: Appl Sci Manuf 1999;30:1423–34.
[25] Ho S, Suo Z. Tunneling cracks in constrained layers. J Appl Mech 1993;60:890–4.
[26] Nakamura T, Kamath MS. Three-dimensional effects in thin film fracture mechanics. Mech Mater 1992;13:67–77.
[27] Cloetens P, Pateyron-Salomé M, Buffière JY, Peix G, Baruchel J, Peyrin F, et al. Observation of microstructure and damage in materials by phase sensitive radiography and tomography. J Appl Phys 1997;81:5878.
[28] Haldrup K, Nielsen SF, Wert AJ. A general methodology for full-field plastic strain measurements using X-ray absorption tomography and internal markers. Exp Mech 2008;48:199–211.

APPENDIX A2

In situ determination of mixed mode fracture energy of glass fibre/matrix interface

Submitted to Composites Part A

In situ determination of mixed mode fracture energy of glass fibre/matrix interface

Karolina Martyniuk [a], Bent F. Sørensen [a*], Stergios Goutianos [a]

[a] Section of Composites and Materials Mechanics, Department of Wind Energy, Technical University of Denmark, Risø Campus, 4000 Roskilde, Denmark

Corresponding author: bsqr@dtu.dk

Section of Composites and Materials Mechanics, Department of Wind Energy, Technical University of Denmark, Risø Campus, Frederiksborgvej 399, 4000 Roskilde, Denmark

Tel.: +45 46775825, E-mail: bsqr@dtu.dk

Abstract

Tensile testing of a specimen consisting of a single glass fibre (oriented perpendicular to the tensile direction) embedded in an epoxy resin is conducted in the vacuum chamber of a scanning electron microscope. Fibre/matrix debonding initiation and propagation, and subsequent interfacial crack kinking into the matrix are observed *in situ*. The debond crack length is measured as function of the applied stress. The experimental measurements are combined with linear elastic fracture mechanics results for energy release rate and mode mixity for the glass fibre/matrix interface available in the literature. Thereby, the fracture energy of the fibre/matrix interface is determined as a function of mode mixity.

Keywords: B. Interface; C. Micro-mechanics; D. Electron microscopy

1 Introduction

The fibre/matrix interface of composite materials has been of scientific interest for a long time, since it plays a crucial role in the load transfer between the matrix and the fibres [1] and thus affects the macroscopic behaviour of the composite material. The first micro-failure which leads to a macro-failure in transverse plies of composite laminates is fibre/matrix interface debonding which subsequently leads to transverse crack formation [2]. Therefore, characterization, understanding and control of the mechanical properties of the interface are of high importance.

Most studies of the fibre/matrix interface properties focus on the interface subjected to shear stresses parallel to the fibre direction. Methods like fibre pull out and push out test [3] or the single fibre fragmentation test [4] have been well established and applied in the research. Thereby, the mechanical properties of the fibre/matrix interface can be characterized in terms of a Mode II fracture energy and a frictional sliding shear stress. The Mode II fracture energy of E-glass fibre/epoxy interface was determined using a single fibre fragmentation test method and found to be in the range of 60-230 J/m^2 depending on the fibre /matrix bonding quality [5]. Analysing a single fibre pull out test Hampe and Marotzke [6] determined the Mode II interface fracture energy for the glass fibre/polycarbonate matrix to be in the range of 70-130 J/m^2.

The experimental methods mentioned above are relevant for debond growth along the fibre direction which occurs for plies where the fibre direction is parallel to the load. However, in multidirectional laminates for structural applications, the first damage often develops in the form of cracks in the transverse plies originating from fibre/matrix debonding. This debonding occurs under mixed mode. For this problem, a single fibre of such a ply loaded transversally as shown schematically in Figure 1 can provide useful information of the fibre/matrix interface properties. The problem depicted in Figure 1 is investigated in the present study. A single fibre embedded in the matrix material is subjected to a remote uniaxial tensile stress acting in the *x*-direction. The fibre

has a radius *a* and a debond crack has formed, spanning an angle θ_{dI} towards the positive *y*-axis direction and an angle θ_{dII} in the negative *y*-axis direction. Due to the elastic mismatch of the fibre and the matrix, the interfacial crack tip is under mixed mode conditions (pure Mode I and pure Mode II do not in general exist for an interface crack [7–9]). It can be noticed in Figure 1 that for small debond angles, $\theta_d \approx 0°$ with respect to the applied load, the interface crack tip will be subjected mainly to normal opening. With increasing debond angle, more tangential crack opening displacement is induced. The mode mixity, ψ, evolves therefore with the debond angle, $\psi = \psi(\theta_d)$, from dominant normal opening ($\psi \approx 0°$) at $\theta_d = 0°$, approaching tangential dominant opening ($\psi \approx 90°$) for higher values of θ_d (Figure 1).

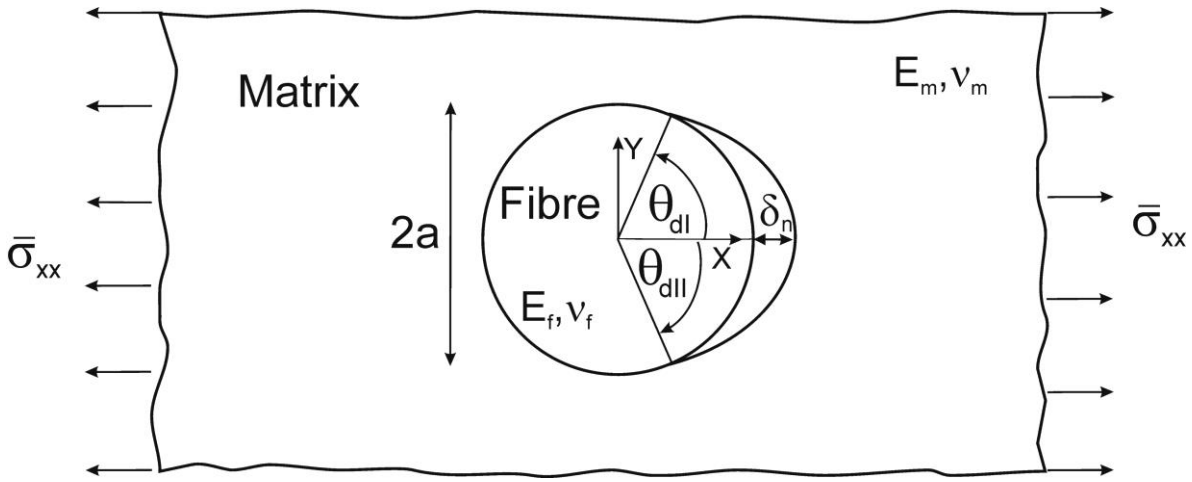

Figure 1. Single fibre embedded in a matrix under remote uniform stress.

It is well established that the fracture energy of bi-material interfaces strongly depends on the mode mixity [10,11]. The fracture energy has been found to increase significantly with an increasing amount of tangential crack opening displacement. Thus, in order to characterize the fibre/matrix

interface completely, the interfacial fracture energy must be determined as a function of mode mixity, $G_c = G_c(\psi)$.

The study of the debonding of a single fibre subjected to a transverse stress may become a method to characterize the mixed mode fracture energy of fibre/matrix interfaces. This was recognized by Varna et al. [12] and Zhang et al. [13], who linked the model results and experimental observations of fibre/matrix interface debonding of a fibre subjected to a transverse stress. Thereby, the interfacial fracture parameters were determined for both fracture under nominal Mode I and nominal Mode II (in [12,13] nominal Mode I is considered for the crack tip at $\theta_d \to 0°$ and nominal Mode II is obtained for the crack tip at $\theta_d \to 57°$). The fracture energy of a glass fibre/matrix interface for nominal Mode I was found to be $G_{Ic} = 2J/m^2$ for the fibres without any coupling agent in the sizing and $G_{cI} = 10J/m^2$ for the fibres with coupling agent [12]. The fracture energy for nominal Mode II was found to be several times higher than for nominal Mode I, $G_{IIc} = 6J/m^2$ and $G_{IIc} = 25J/m^2$ for the fibres without and with coupling agent respectively [12]. For $\theta_d > 57°$ the debond surfaces are assumed to be partly in contact [12].

The energy release rate of a glass fibre/matrix interface was determined by numerical simulations elsewhere [14–18]. The energy release rate and the mode mixity were determined as functions of debonding angle by París et al. [14] and Correa et al. [11]. The results predicted an unstable debonding from $\theta_d = 0°$ up to $\theta_d = 60° - 70°$, followed by either a stable debond crack growth (under dominant Mode II) or by crack kinking out of the interface into the matrix [14,17].

As described before, fracture energy of the fibre/matrix interface can be determined as a function of mode mixity by measuring the debond angle, θ_d of a single fibre undergoing debonding under a remote uniform stress. However, most of the reported experimental methods for investigation of debonding of a single fibre under transverse stress utilize optical microscopy for the debond

observations using a viewing direction perpendicular to the fibre direction [13,15,17,19]. This viewing direction is not well suited for the determination of the debond angle. Precise debond angle measurements require the viewing from the fibre direction (the *z*-direction) as shown in Figure 1.

In the present study, a method for *in situ* fibre/matrix interfacial debonding observations with a viewing direction parallel to the fibre direction is proposed. The method involves testing of a specimen with a single fibre embedded in the matrix, subjected to a transverse stress in the chamber of scanning electron microscope (SEM). Debond crack length and opening are measured *in situ* for several load steps. Subsequently, the experimental measurements are combined with results from model results by París et al. [14] and the mixed mode fracture energy is determined as a function of mode mixity.

2 Fracture mechanics of an interface crack - theory

2.1 Mixed mode fracture energy of the fibre/matrix interface, $G_c(\psi)$

An analytical solution of the energy release rate as a function of the debond angle for a circular inclusion embedded in infinite solid has been developed by Toya [20]. The energy release rate for the interfacial debonding, derived by the use of the Irwin's virtual crack closure technique [21], can be written as [14]:

$$G = g^* \pi \frac{(1-\nu_f^2)\bar{\sigma}_{xx}^2 a}{E_f}, \qquad \text{Equation 1}$$

where $\bar{\sigma}_{xx}$ is the applied remote stress, E_f and ν_f are the fibre Young's modulus and the Poission's ratio respectively, a is the fibre radius and g^* is a non-dimensional parameter that depends on the debond angle, θ_d and the Dundurs bi-material mismatch parameters, α, β [18, 22],

$$g^* = g^*(\theta_d, \alpha, \beta) \qquad \text{Equation 2}$$

The two Dundurs' parameters, α and β, depend on E_f, ν_f as well as on the Young's modulus and Poisson's ratio of the matrix material, E_m and ν_m.

2.2 Mode mixity of the fibre/matrix interfacial crack tip, ψ

The mode mixity of an interface crack tip is defined as [8,9]:

$$\psi = \tan^{-1}\left\{\frac{I_m\{Kl^{i\varepsilon}\}}{\mathrm{Re}\{Kl^{i\varepsilon}\}}\right\} \qquad \text{Equation 3}$$

where, $K = K_1 + iK_2$ is the complex stress intensity factor of the interface crack, ε is the bi-material constant given by

$$\varepsilon = \frac{1}{2\pi}\ln\frac{1-\beta}{1+\beta} \qquad \text{Equation 4}$$

and l is a chosen length scale [8,9].

3 Materials and methods

3.1 Specimen

In the present study, dogbone shaped tensile test specimens consisting of a single fibre embedded in the epoxy matrix were manufactured and tested. Glass fibres (provided by Ahlstrom, Finland), with diameter of D~50μm were embedded in an epoxy resin (Epoxydharz HT 2, from Faserverbundwerkstoffe GmbH, Composite Technology). The fibres were kept pre-strained while the specimens were cured in an attempt to minimize the process induced residual stresses in the fibre direction [22]. The manufacturing process here was similar to that reported elsewhere [23]. No tabs were attached to the specimen. The surfaces to be observed in the experiments were polished,

so the microcracks were removed making the samples suitable for SEM scanning. Since SEM was to be used for observing and measuring the fibre/matrix interfacial debonding, the surface to be observed was coated with a conductive carbon layer in order to prevent sample charging during scanning in the SEM. Additionally, a double-sided carbon tape was placed on both ends of the samples, so that there was a contact between the sample, the carbon layer deposited on the sample and the sample holder. Thereby, the electron flow from the non-conductive sample was facilitated. The charge accumulated on the non-conductive sample surface flows to the ground (Figure 2).

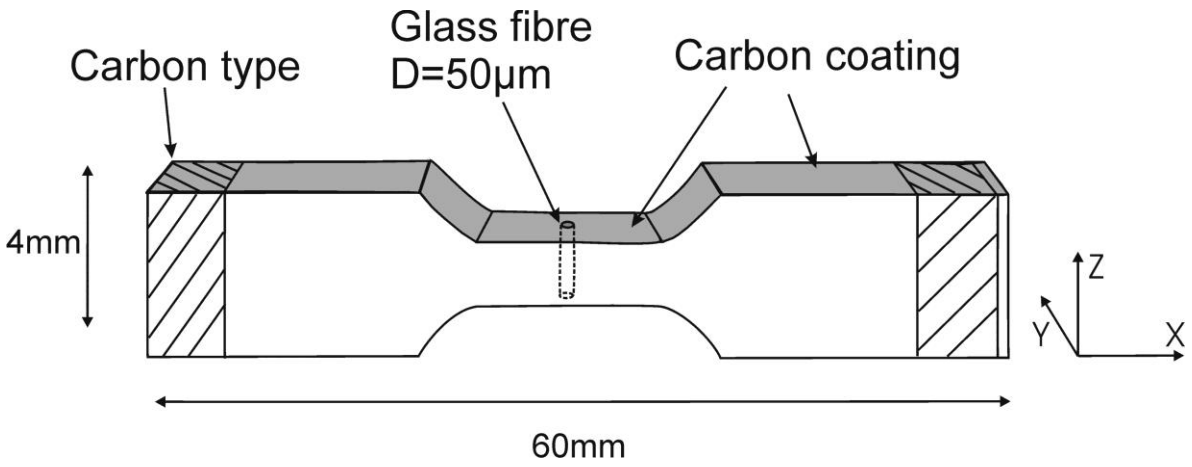

Figure 2. Sample geometry tested in the experiments. Details about the sample dimensions can be found in [23].

3.2 Experimental testing procedure

Prior to the loading, the samples were examined in the SEM in order to investigate whether the fibre/matrix bonding was intact after the manufacturing process. An example of proper (i.e. not debonded) fibre/ matrix interface is shown in Figure 5a. Three samples were successfully tested.

The fracture tests were conducted in the vacuum chamber of a SEM (Zeiss, EVO60) in order to observe the fibre/matrix interfacial crack initiation and propagation *in situ*. An in-house made

tensile loading fixture [24] with 500N load cell was placed in the SEM chamber. The fixture with mounted specimen is shown in Figure 3. One of the specimen ends was fixed to a loading block and the load was imposed by displacing the loading block gradually along the specimen in longitudinal direction (*x*–direction in Figure 2) using an electrical motor.

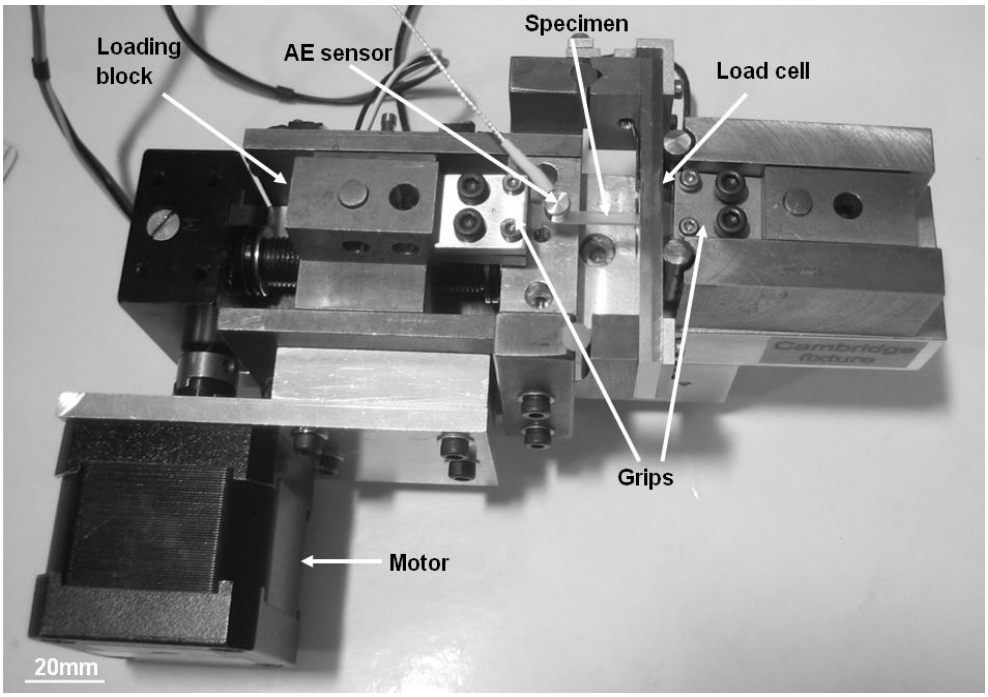

Figure 3. Test set up for *in situ* SEM observations.

The load was applied with a constant displacement rate of ~16 μm/min, in steps in such a way that the nominal tensile stress increment was ~1-2MPa. After applying the nominal stress, the sample was unloaded by ~30% in order to minimize deformation due to creep and to prevent damage evolution during the scanning time. During the image acquisition, the position of the grips was held fixed. After imaging, the displacement was increased until the stress had exceeded the previous maximum stress by ~1-2MPa, where after the specimen was unloaded by ~30% again, etc. In the remainder of this paper, we will report the maximum applied stress of a given load step, i.e. the

applied stress before unloading. The step wise loading is schematically shown in Figure 4. The load was converted to a nominal stress, $\bar{\sigma}_{xx}$, calculated as the applied force divided by the cross sectional area of the specimen gauge section (2×2mm).

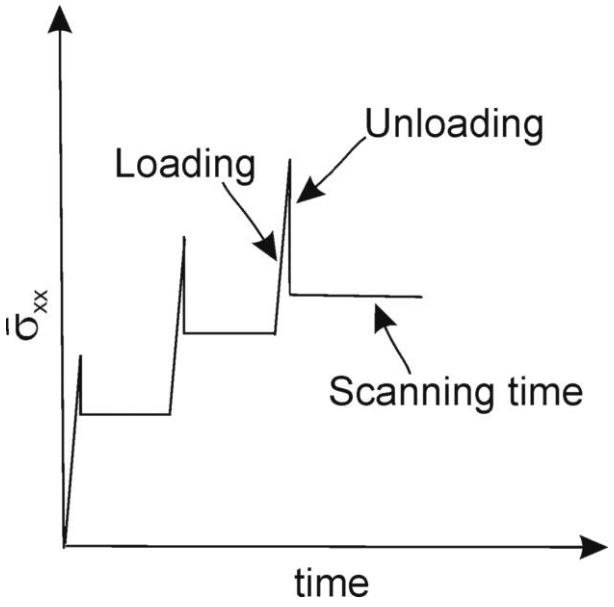

Figure 4. Step wise loading in *in situ* fracture tests in SEM.

Additionally, an acoustic emission (AE) sensor (Pico sensor, Physical Acoustic Corp., Princeton), was placed on the sample to facilitate detection of damage during loading (see Figure 3). The sensor was attached to the sample by a small clip without using any couplant which allowed for mounting the sensor inside the high vacuum chamber of SEM. An AE system was used during some of tests as additional detector for any damage initiation/propagation. The threshold of the AE system was set to 30dB. AE signal was recorded during loading and the loading was interrupted when any AE event was recorded. Otherwise, the loading was applied in increments of ~1-2 MPa.

SEM images of the free surface of the sample were acquired with a magnification of ~1000× which allowed for the viewing the entire fibre with the pixel size of ~128±5nm. Secondary electron mixed

with back scattered electron signals were used which allowed for imaging the new surfaces created during interfacial debonding with minimized charge-up effect on the images quality.

4 Experimental results

The debond angle, θ_d and the normal opening of the debond, δ_n (defined in Figure 1), were measured from the SEM images for all load steps. Since the problem is symmetric about the *x*-plane, two debond angles θ_{dI} and θ_{dII} were measured as indicated in Figure 1.

An example of the general sequence of the fibre/matrix debonding initiation, propagation and the interfacial kinking into the matrix is shown in Figure 5.

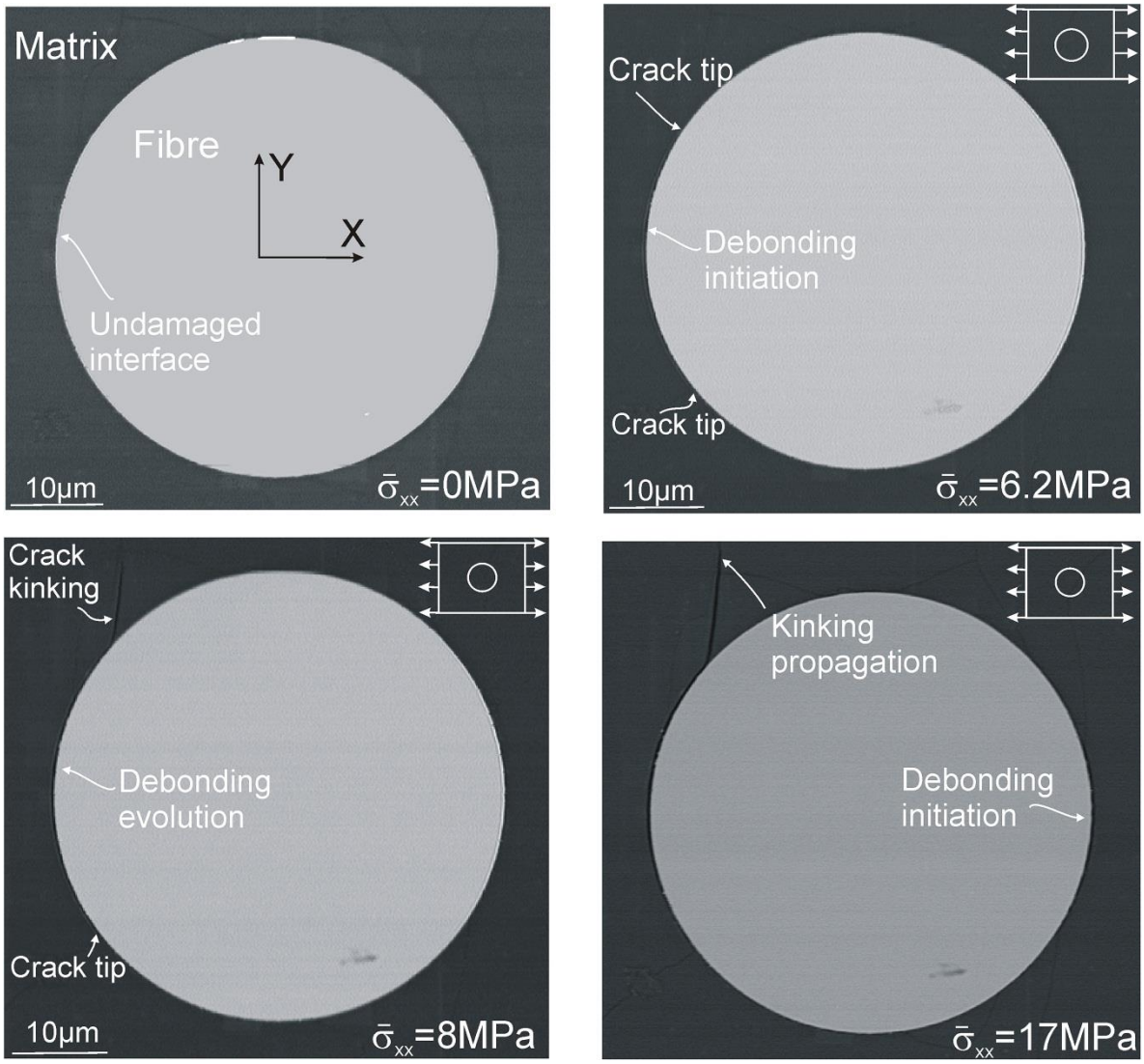

Figure 5. Micrographs of the damage sequence of a single fibre under remote uniform stress observed in SEM.

The example of the measurements of the debond angle and the normal opening is shown in Figure 6. In Figure 6 only a quarter of the fibre is shown, so that debonds are more visible.

The first crack was observed at the nominal stress of $\bar{\sigma}_{xx} \sim 5MPa$ (Figure 5b). Since the load was applied in increments of ~1-2MPa, the debonding initiation must have occured in the nominal stress range of $\bar{\sigma}_{xx} = 3\text{-}5MPa$. The normal opening, δ_n at this stress level was in the range of

$\delta_n \sim 0.17\mu m$ and the debond angle had reached $\theta_d = 50° \pm 15°$ showing that the initial debonding was unstable. An example of the first debond arrest is shown in Figure 5b and Figure 6b. The debonding was observed to evolve in the subsequent load steps. However, at some of the applied load steps, the debond angle did not increase. In other words, the crack tip was stationary although the load was increased (see Figure 7a). The debond angles and normal openings measured at different load steps are presented in Figure 7a and Figure 7b, respectively, as functions of the applied stress for three identical tests. The debond angles θ_{dI} and θ_{dII} developed fairly similarly for all load steps in all experiments. The maximum debond angle reached an average value of $\theta_d = 60° \pm 10°$ at stress level of $\bar{\sigma}_{xx} \sim 12MPa$ (see Figure 7a). The maximum normal opening at this level was found to be $\delta_n \sim 0.3\mu m$ (see Figure 7b).

Only one to two debond crack propagation/arrests were observed in each sample before crack kinking occurred at the average stress of $\bar{\sigma}_{xx} \sim 13MPa$. The crack kinked out of the interface into the matrix at a debond angle of $\theta_d = 60° \pm 14°$. The kinked crack propagated unstably into the matrix nearly perpendicular to the applied stress direction as shown in Figure 5c. Further stress increase caused further propagation of both the debond crack and the matrix crack, and eventually the initiation of a second debond crack on the other side of the fibre, at $\theta_d = 180°$ (see example in Figure 5d).

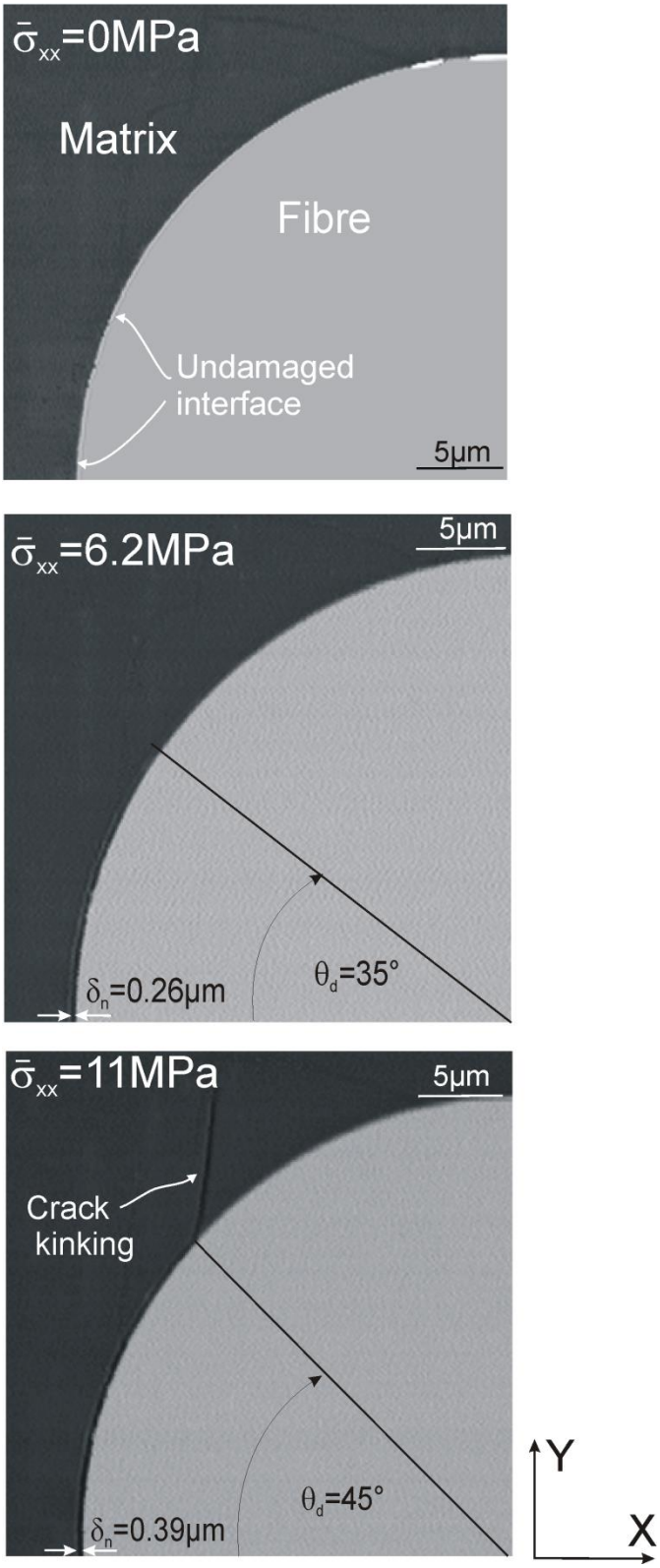

Figure 6. Micrographs of interfacial crack sequence and debond crack tip advancement.

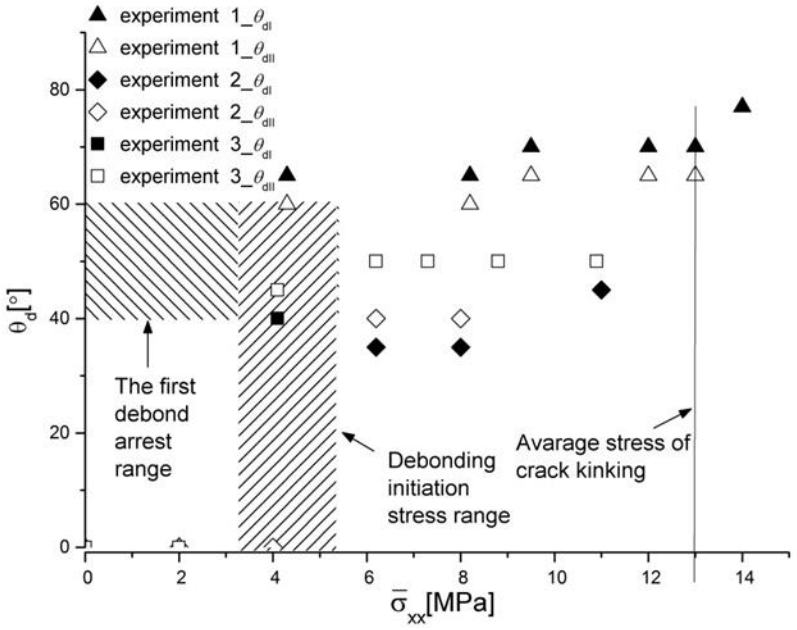

(a)

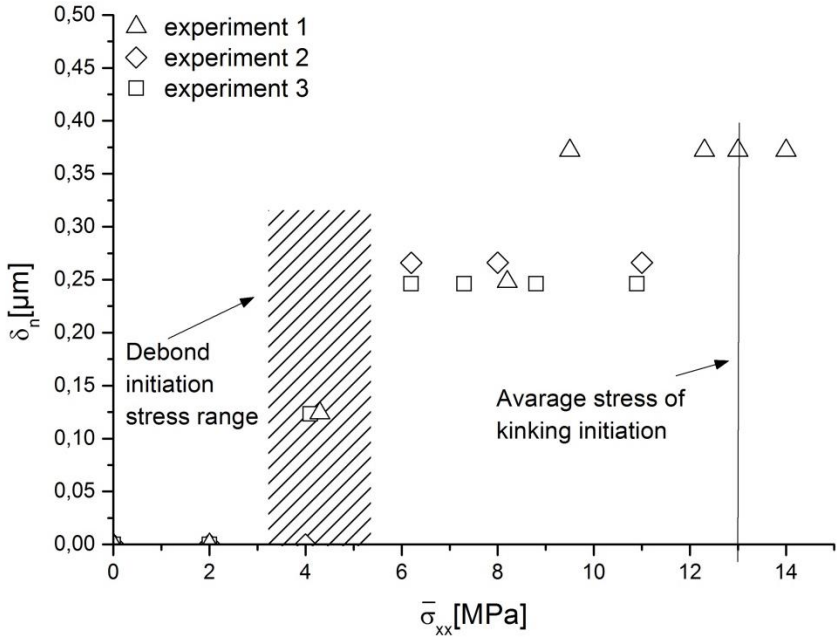

(b)

Figure 7. Experimental results for debond profiles as functions of applied stress: a) debond angle, b) normal opening.

The later stages of propagation of the first debond crack (assumed to start at $\theta_d = 0°$) is obviously influenced by the presence of the second debond crack (observed at $\theta_d = 180°$) and by any crack kinking. Therefore, in the present study, only the measurements of the debond angles of the first debond crack until kinking or the debonding initiation of the second debond occurred will be used in the interface fracture energy calculations. The last debond angle included in the measurements presented in Figure 7a is the angle at kinking. Likewise, the last normal opening data points presented in Figure 7b are the ones measured before the initiation of the second debond (at $\theta_d = 180°$). Although the stress was applied with the increment of ~1-2MPa, in some cases due to the low image quality, the debond measurement was impossible. No fracture process zone was identified in the images acquired with the resolution.

In some cases where AE activity was detected, damage was seen on the micrographs. However, at some of the load steps the damage initiation/propagation visible in the SEM micrographs was not detected by AE system.

5 Data analysis

The results obtained from the *in situ* observations in SEM are used for determination of the interface mixed mode fracture energy as a function of mode mixity, $G_c = G_c(\psi)$. The experimental measurements presented in the previous section are combined with the model results by París et al. [14]. The following section includes the data analysis and the procedure for the *in situ* determination of the fracture energy and the mode mixity.

París et al. [14] applied LEFM for the analysis of fibre/matrix debonding. Use of LEFM requires that the fracture process zone (FPZ) is assumed to be very small in comparison with the fibre diameter and the debond length [25].

The mixed mode fracture energy for the experimental measurements is determined as follows. First, from Figure 9 in París et al. [14] we read off the non-dimensional parameter g^* (defined in

Eq. 2 in Sec. 2) for each debond angle. The values of g^* used in calculations in this paper are listed in Table 1. G is then obtained from Equation 1 using the experimental data (radius of the fibre used in the experiments, a=0.025mm, the applied tensile stress level, $\bar{\sigma}_{xx}$), and the elastic data in Table 3.

Table 1. Non-dimensional energy release rate, g^* by París [14], used in the calculations in this paper.

θ_d [°]	g^*
10	0,182
30	0,469
44	0,609
60	0,662
75	0,615
90	0,469
100	0,338
110	0,212
120	0,107
130	0,040
140	0,008

Since the debond angle increased in small bursts (see Figure 7a), it is appropriate to characterise the interface fracture energy in terms of two values of G_c for each crack growth event, a value G_c^p for the onset of the crack propagation and a value of G_c^a corresponding to the arrest of crack growth. G_c^p is calculated using $\bar{\sigma}_{xx}$ and the debond angle θ_d prior to cracking, G_c^a is calculated using $\bar{\sigma}_{xx}$ and θ_d after the crack arrest. When there was no crack propagation observed after increasing the load, the crack tip is considered to be stationary and therefore no fracture energy is determined.

The mode mixity as a function of the debond angle $\psi = \psi(\theta_d)$ was read off from Figure 10 in [14]. The values of $\psi = \psi(\theta_d)$ from [14] and the values are listed in Table 2.

Table 2. Results for the mode mixity as a function of debond angle by París [14] and used in the calculations in this paper.

θ_d [°]	ψ[°]
10	20,43
25	40,00
30	46,22
44	63,30
50	70,63
60	83,34
70	94,48
75	101,50
90	120,74

The mode mixity in numerical simulations in [14] was determined using Eq.3. The Dundurs parameters for glass fibre-epoxy system used in [14] are $\alpha = 0.919$ $\beta = 0.229$, giving $\varepsilon = -0.074$; the length scale chosen in [14] in the calculations of ψ is $l = 0.045985mm$. The elastic parameters used in the present study are listed in Table 3.

Eventually, having determined the fracture energy as a function of the debond angle at arrest and propagation, $G_c^a(\theta_d)$, $G_c^p(\theta_d)$, and the phase angle with respect to the debond angle, $\psi(\theta_d)$, the desired fracture energy as a function of the mode mixity was obtained, $G_c^a = G_c^a(\psi)$ and $G_c^p = G_c^p(\psi)$.

Table 3. Materials parameters used in numerical simulation by París et al. [14] and in the calculations

in the current paper.

Material	Young's Modulus [GPa]	Poisson's ratio [-]
Glass fibre	E_f=70	ν_f=0.22
Epoxy	E_m=2.2	ν_m=0.33

6 Results

The fracture energy of the interface in the form of $G_c^a(\psi)$ and $G_c^p(\psi)$ is presented in Figure 8. Due to the unstable debond propagation up to $\theta_d = 50° \pm 15°$ (see experimental results in Figure 7a), no measurements of the fracture energy were obtained for $\psi < 50°$. It can be seen in Figure 8 that the fracture energy increases with increase of the mode mixity for both, G_c^a and G_c^p; the fracture energy for $\psi \approx 90°$ is several times that for $\psi \approx 50°$. A similar tendency for has been found in other experimentally determined mixed mode interfacial fracture energy, see e.g. [8,10]. The function [8]

$$G_c(\psi) = G_I^c\{1 + tan^2[(1-\Lambda)\psi]\} \qquad \text{Equation 5}$$

is used to fit the data. Here, G_I^c is the value of G_I at $\psi = 0°$ and Λ is a dimensionless constant. Two different fitting curves, for crack arrest and crack propagation, respectively, are plotted in Figure 8 using the function in Eq. 4. The parameters used in fitting the curves are listed in Table 4. Based on the fitted curves, the fracture energy for mode mixity $\psi \sim 0°$ is extrapolated to be

$G_c^a(\psi = 0°) \sim 0.2\, J/m^2$ and $G_c^p(\psi = 0°) \sim 0.4\, J/m^2$ for crack arrest and crack propagation respectively; for $\psi \sim 90°$ the fracture energy is in the range of $G_c^a(\psi = 90°) \sim 2\, J/m^2$ and $G_c^p(\psi = 90°) \sim 3\, J/m^2$.

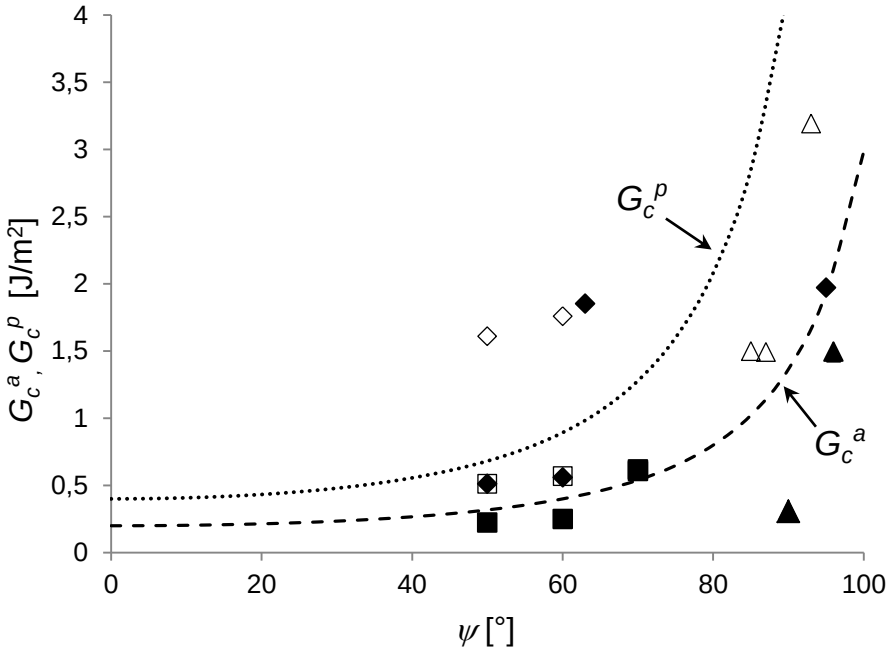

Figure 8. Experimentally determined fracture energy for the crack propagation (open symbols) and crack arrest (fill symbols) as a function of phase angle. Symbols are experimental values; curves are fits.

Table 4. Fitting parameters for G_c^a and G_c^p .

Fitting parameter	Value
$G_c^a \ [J/m^2]$	0.2
Λ_a [ ]	0.25
$G_c^p \ [J/m^2]$	0.4
Λ_p [-]	0.2

8 Discussion

Comparison of fracture energy data

The fracture energy of the glass fibre/epoxy interface found in the present study is relatively low in comparison with data from the literature. For the similar materials system, the interface fracture energy was found to be in the range of 2-10 J/m^2 and 6-25 J/m^2 for $\psi = 0°$ and $\psi = 90°$ respectively [12,13]. One reason for this difference can be that the present method (high magnification SEM images) enables a very early detection of cracking, possibly earlier than most of other experimental methods. Other possible reasons are discussed in the subsequent section. Moreover, the fracture behaviour in the present study was such that it was useful to make a distinction between the fracture energy at crack arrest and at crack propagation. A similar behaviour was observed in cracking of ceramics [26] and in silicon/epoxy interface cracking [27].

Estimation of the steady-state energy release rate of a tunnelling crack

An independent of the estimate of the average interfacial fracture energy can be made by from the occurrence of the tunnelling cracking. According to Hutchinson and Suo [8], the steady-state energy release rate of a tunnelling crack can be computed according to

$$G_{ss} = \frac{1}{h}\int_0^h G(c)\,dc \qquad \text{Equation 6}$$

where h is the "hight" of the tunnelling crack and $G(c)$ is the energy release rate of the plane strain crack with a crack length c. Converting to cylindrical coordinates and using the solution for the partially debonded fibre of Paris *et al*. [14], Eq. (6) leads to

$$G_{ss} = g_{ss}^{*}\,\pi\frac{\left(1-\nu_f^2\right)}{E_f}\bar{\sigma}_{xx}^2\,a \qquad \text{Equation 7}$$

where the function $g_{ss}^{*}(\theta_{ss},\alpha,\beta)$ is defined

$$g_{ss}^{*}(\theta_{ss},\alpha,\beta) = \frac{1}{\theta_{ss}}\int_0^{\theta_{ss}} g^{*}(\theta_d,\alpha,\beta)\,d\theta_d \qquad \text{Equation 8}$$

and $g^{*}(\theta_d,\alpha,\beta)$ is given by Eq. (2). In the study of fibre/matrix debonding for the same material system and test specimen observed in 3D by means of X-ray tomography, Martyniuk *et al*. [23] found tunnelling cracking to occur with $\theta_{ss} \approx 50°$ at $\bar{\sigma}_{xx} = 44.2MPa$. Fitting a third order polynomial to the function for $g^{*}(\theta_d)$ data of Paris *et al*. (in the range from 0° to 60°, values given in Table 1) and performing the integration according to Eq. (8), we find $g_{ss}^{*}(\theta_{ss},\alpha,\beta) = 0.379$ for

$\theta_{ss} \approx 50°$. Then by Eq. (7) we get $G_{ss} = 0.79 J/m^2$. During tunnelling, G_{ss} must be equal to the average mixed mode fracture energy of the tunnelling crack front. Since the exact shape of the crack front is unknown we cannot estimate the (average) mode mixity along the crack front. Never the less, it is relevant to compare the value of G_{ss} (determined from 3D X-ray) with the mixed mode fracture energy for propagation, G_c^p determined from the 2D (SEM) experiments, since tunnelling cracking is expected to occur unstably. The value of G_{ss} (0.79 J/m^2) lies within the range of G_c^p for $\psi \approx$ 50 -60°, see Figure 8.

The finding that the value of steady-state energy release rate, G_{ss} determined independently from tunnelling cracking taking place far below the free edge, is in good agreement with the G_c^p values determined from the surface observations, supports the hypothesis that the fracture energy values determined from the 2D SEM observations are representative of the fibre/matrix interface along the entire fibre and thus supports the approach of using 2D surface observations for the determination of the mixed mode fracture energy of the fibre/matrix interface.

Limitations of the experimental measurements in SEM

The *in situ* observations during the fracture tests in SEM allowed only for debond measurements by normal opening displacement of the interface crack. For the normal crack openings displacement measurements at $\theta_d = 0°$, the accuracy is limited only by the SEM micrographs resolution. The accuracy of the debond angles measurements, however, is additionally limited by the mode mixity conditions of the crack tip; with an increase in the debond angle the tangential opening displacement becomes dominant. However, in the present experimental approach the tangential crack opening displacement at the crack tip is not measureable. Therefore, the debond angles might be larger than those measurable in SEM micrographs (shown in Figure 7a). On the other hand, the kinking observed in the experiments indicates that the debond crack tip had been at the location

where the kinking occurred. In other words, the angle of kinking, which is clearly visible in SEM micrographs, can be seen as indications of the accurate debond angle measurements. The accuracy of the debond measurements can be improved by the use of the Digital Image Correlation (DIC) technique which has been proposed for microscopic displacement mapping using images acquired by SEM [28–30]. The use of the DIC method would enable the measurements of both the normal and tangential crack opening displacements [30]. Possibly, the mode mixity might be determined using the near crack tip opening displacements measured experimentally.

The debond angle measurements are also limited by the occurrence of unstable crack growth (see Figure 5, Figure 7). Although undesirable from the point of view of fracture energy determination, the unstable debond propagation up to the interval of $\theta_d = 40° - 60°$ is in good agreement with the numerical predictions in [14]. It is of high interest, however, to be able to obtain the fracture energy for the smaller debond angles such that it becomes possible to measure fracture energy for lower values of ψ. The debond growth of one fibre might be stabilized e.g. by another fibre positioned in its neighbourhood. It is expected that performing the same type of tensile tests as presented in the present paper, using the samples with more fibres placed relatively close to each other would allow for a stable debonding propagation and thereby for the fracture energy determination for mode mixity $\psi < 50°$. Design of such experiments, however, also requires a fracture mechanical model of two fibres.

It is also recognized that the experimental set up proposed in this paper allows only for 2D observations of the free-edge of the sample. Due to the complex stress state existing near the free edge of bi-material specimens [31], the crack is expected to initiate at this location and subsequently propagate into the specimen. In fact a 3D X-ray tomography study has shown that the shapes of debond crack front inside the sample were different from those at the free surface of the sample [23].

Another error source that may influence the debonding at the surface is the sample preparation which involves grinding and polishing of the surfaces of the samples. The polishing (involving mechanical pressure, and different lubricants etc.), might have affected the fibre/matrix interface at the surface. Thus, there is a potential risk that the interface properties at the free surface might be not representative for the interface properties further inside the sample. Moreover, the process induced residual stresses may also influence the interface properties. Although the fibres were pre-strained while they were encased in the epoxy in an attempt to minimize the residual stresses, we have no measurements that show that the residual stresses in the samples can be ignored.

Experiments vs numerical simulations

In the current paper, LEFM approach was applied for the interface fracture energy determination. In the use of LEFM, the size of the fracture process zone (FPZ) of the debond crack is assumed to be very small in comparison with the fibre diameter and the debond crack length [25]. If the FPZ is small, the details of the cohesive law describing interface debonding are unimportant and the fracture energy is sufficient to be used as a criterion for crack growth. In order to test this assumption and to estimate the size of the FPZ, a 2D cohesive-zone micromechanical model is currently under development. The applicability of the LEFM approach will be verified by studying the influence of the cohesive law parameters on the fibre/matrix interface debonding initiation and propagation. Only the debond angle measurements were used in the LEFM analysis in the current paper; however, the debond normal openings (defined in Figure 1) were also measured in the experiments. Therefore, in the cohesive-zone modelling of the fibre/matrix interface fracture process the two main debond features can be used, the debond angle and the normal opening. This can possibly increase the accuracy of the determination of the mixed mode fracture energy.

It is also recognized that the elastic properties of the materials used in the experiments are slightly different from those used in the model in [14] giving the values of g^* and ψ that are used in this

paper. However, it was shown in [14] that the geometrical features of the problem play a more important role in the fracture process than the elastic properties of involved materials. It is therefore reasonable to conclude that the experimental observations presented in this paper can be interpreted by the use of the model results in [14] regardless the differences of the elastic parameters of used materials.

Summary and conclusions

A method for the *in situ* determination of the mixed mode fracture energy of a fibre/matrix interface has been developed and used. The debond angle and the normal opening were measured as functions of applied stress from SEM images. By combining the experimental measurements with model predictions based on LEFM approach, the fracture energy of the interface was determined as a function of the mode mixity, ψ . The fracture energy is determined in terms of values corresponding to both crack propagation and crack arrest, G_c^p and G_c^a . Due to the instability of the debond propagation observed in the experiments, the fracture energy was determined only for $\psi > 50°$. However, the data for smaller values of ψ is estimated using extrapolation to about $G_c^a(\psi \approx 0°) \sim 0.2\, J/m^2$ and $G_c^p(\psi \approx 0°) \sim 0.4\, J/m^2$ for crack arrest and crack propagation respectively; for $\psi \sim 90°$ these values are found to be $G_c^a(\psi \approx 90°) \sim 2\, J/m^2$ and $G_c^p(\psi \approx 90°) \sim 3\, J/m^2$. It has been also shown that the fracture energy values determined from the 2D SEM observations for the debond propagation are representative for the fibre/matrix interface along the fibre.

Acknowledgements

The authors would like to thank Mr. Jukka Koulu from Ahlstrom Glassfibre, Finland for providing glass fibres for samples manufacturing. At DTU Wind Energy, we would like to thank Malcolm McGugan, Jens Olsson and Erik Vogeley for their inspiration and help with the test set up. Research

technicians Jonas Kreutzfeldt Heininge, Christian H. Madsen from DTU Wind Energy and Steen Johannes Bang from DTU Energy Conversion and Storage are thanked for the help with specimen preparation. Elena Correa Montoto from University of Seville, Continuum Mechanics Department is thanked for providing numerical results used in this work and for her advices. Julie Anne Glasscock from DTU Energy Conversion and Storage is acknowledged for the support in SEM test set up and scanning. Hans Lilholt from DTU Wind Energy is thanked for inspiring discussions and ideas for data analysis.

References

[1] D. Hull, T.W. Clyne, An introduction to composite materials, Second Edi, Press Syndicate of the University of Cambridge, Cambridge, 1981.

[2] E.K. Gamstedt, B.A. Sjögren, Micromechanisms in tension-compression fatigue of composite laminates containing transverse plies, Composites Science and Technology. 59 (1999) 167–178.

[3] R.J. Kerans, T.A. Parthasarathy, Theoretical Analysis of the Fiber Pullout and Pushout Tests, J. Am. Ceram. Soc. 74 (1991) 1585–1596.

[4] H.D. Wagner, J.A. Nairn, M. Detassis, Toughness of Interfaces from Initial Fiber-Matrix Debonding in a Single Fiber Composite Fragmentation Test, Applied Composite Materials. 2 (1995) 107–117.

[5] A.T. DiBenedetto, Measurement of the Thermomechanieal Stability of Interphases by the Embedded Single Fiber Test A. T. DiBenedetto, Composites Science and Technology. 42 (1991) 103–123.

[6] A. Hampe, C. Marotzke, The fracture toughness of glass fibre- polymer matrix interface: measurement and theoretical analysis., Proc. Third Int.Conf. Deformation and Fracture of Composites. (1995) 132.

[7] J.W. Hutchinson, Mixed mode fracture mechanics of interfaces, Metal-Ceramics, Acta-Scripta Metallurgica Proceedings Series. 4 (1990) 295–306.

[8] J.W. Hutchinson, Z. Suo, Mixed Mode Cracking in Layered Materials, in: Advances in Applied Mechanics, 1992: pp. 63–191.

[9] J.R. Rice, Elastic Fracture Mechanics Concepts for Interfacial Cracks, Journal of Applied Mechanics. 110 (1988) 98–103.

[10] K.M. Liechti, Y.S. Chai, Asymmetric Shielding in Interfacial Fracture Under In-Plane Shear, Journal of Applied Mechanics. 59 (1992) 295–304.

[11] H.C. Cao, A.G. Evans, An experimental study of the fracture resistance of bimaterial interfaces, Mechanics of Materials. 7 (1989) 295–304.

[12] J. Varna, L.A. Berglund, M.L. Ericson, Transverse single-fibre test for interfacial debonding in composites:2. Modelling, Composites Part A: Applied Science and Manufacturing. 28A (1997) 317–326.

[13] H. Zhang, M.L. Ericson, J. Varna, L.A. Berglund, Transverse single-fibre test for interfacial debonding in composites: 1. Experimental observations, Composites Part A: Applied Science and Manufacturing. 28 (1997) 309–315.

[14] F. París, E. Correa, V. Mantič, Kinking of Transversal Interface Cracks Between Fiber and Matrix, Journal of Applied Mechanics. 74 (2007) 703–716.

[15] J. Koyanagi, P.D. Shah, S. Kimura, S.K. Ha, H. Kawada, Mixed-Mode Interfacial Debonding Simulation in Single-Fiber Composite under a Transverse Load, Journal of Solid Mechanics and Materials Engineering. 3 (2009) 796–806.

[16] E. Correa, V. Mantič, F. Paris, A micromechanical view of inter-fibre failure of composite materials under compression transverse to the fibres, Composites Science and Technology. 68 (2008) 2010–2021.

[17] E. Correa, E.K. Gamstedt, F. París, V. Mantič, Effects of the presence of compression in transverse cyclic loading on fibre–matrix debonding in unidirectional composite plies, Composites Part A: Applied Science and Manufacturing. 38 (2007) 2260–2269.

[18] V. Mantič, Interface crack onset at a circular cylindrical inclusion under a remote transverse tension. Application of a coupled stress and energy criterion, International Journal of Solids and Structures. 46 (2009) 1287–1304.

[19] P.F.M. Meurs, B.A.G. Schrauwen, P.J.G. Schreurs, T. Peijs, Determination of the interfacial normal strength using single fibre model composites, Composites Part A: Applied Science and Manufacturing. 29 (1998) 1027–1034.

[20] M. Toya, A crack along the interface of a circural inclusion embedded in an infinite solid, J. Mech. Phys. Solids. 22 (1974) 325–348.

[21] G.R. Irwin, Analysis of stress and strain near the end of a crack transversing a plate, Journal of Applied Mechanics. 24 (1957) 361–364.

[22] H.D. Wagner, X.-F. Zhou, A twin-fiber fragmentation experiment, Composites Part A: Applied Science and Manufacturing. 29A (1998) 331–335.

[23] K. Martyniuk, B.F. Sørensen, P. Modregger, E.M. Lauridsen, 3D in situ observations of glass fibre/matrix interfacial debonding, Composites Part A: Applied Science and Manufacturing. 55 (2013) 63–73.

[24] B.F. Sørensen, A. Horsewell, P. Skov-Hansen, In situ observations of crack formation in multi-filament Bi-2223 HTS tapes, Physica C: Superconductivity. 372-376 (2002) 1032–1035.

[25] J.R. Rice, Mathematical Analysis in the Mechanics of Fracture, in: Mathematical Fundamentals, 1968: pp. 191–311.

[26] A.N. Kumar, B.F. Sørensen, Fracture Resistance and Stable Crack-Growth Behavior of, J. Am. Ceram. Soc. 83 (2000) 1199–1206.

[27] S. Gowrishankar, H. Mei, K.M. Liechti, R. Huang, A comparison of direct and iterative methods for determining traction-separation relations, International Journal of Fracture. 177 (2012) 109–128.

[28] J. Kang, M. Jain, D.S. Wilkinson, J.D. Embury, Microscopic Strain Mapping Using Scanning Electron Microscopy Topography Image Correlation at Large Strain, The Journal of Strain Analysis for Engineering Design. 40 (2005) 559–570.

[29] M.A. Sutton, N. Li, D. Garcia, N. Cornille, J.J. Orteu, S.R. McNeill, et al., Scanning Electron Microscopy for Quantitative Small and Large Deformation Measurements Part II: Experimental Validation for Magnifications from 200 to 10,000, Experimental Mechanics. 47 (2007) 789–804.

[30] M.A. Sutton, J. Orteu, H.W. Schreier, Image Correlation for Shape, Motion and Deformation Measurements, 2009.

[31] D.B. Bogy, Two Edge-Bonded Elastic Wedges of Different Materials and Wedge Angles Under Surface Tractions, Journal of Applied Mechanics. 38 (1971) 377–386.

APPENDIX A3

Mixed mode cohesive-zone model for identification of fracture properties of a fibre/matrix interface under transverse load

To be submitted to Composites Part A

Mixed-mode cohesive-zone model for identification of fracture properties of a fibre/matrix interface under transverse load

Karolina Martyniuk [a *], Bent F. Sørensen [a], Qingda Yang [b], Wei Liu [b]

[a] Section of Composites and Materials Mechanics, Department of Wind Energy, Technical University of Denmark, Risø Campus, 4000 Roskilde, Denmark

[b] Department of Mechanical and Aerospace Engineering, University of Miami, Coral Gables, FL, USA

Corresponding author: bsqr@dtu.dk

Section of Composites and Materials Mechanics, Department of Wind Energy, Technical University of Denmark, Risø Campus, 4000 Roskilde, Denmark

Frederiksborgvej 399, 4000 Roskilde, Denmark

Abstract

The fracture properties of a fibre/matrix interface were determined by a coupled experimental and numerical approach. In previous work, *in situ* observations of fibre/matrix debonding initiation and propagation were obtained by performing tensile tests of a specimen with a single glass fibre. In the present study, numerical simulations of a single fibre subjected to a transverse load were carried out using an augmented finite elements method (A-FEM). By this coupled experimental and numerical approach, mixed-mode fracture energy of a glass fibre/matrix interface is determined and the

interface cohesive law parameters are identified. The observed interfacial crack kinking out of the interface into the matrix is shown to be controlled by the interface strength.

Keywords: single fibre, fibre/matrix interface, kinked crack, cohesive law, A-FEM

1 Introduction

The microscale properties of composites strongly affect their macroscopic behaviour. Therefore understanding and control of the interface properties is of high importance. In order to be able to predict the macroscopic behaviour of composites, an understanding of microscale damage evolution is required. The properties of all microscale parameters should be characterized, including the fibres, the fibres distribution, the matrix, the fibre/matrix interface, and the porosity contents and distribution. For instance, it has been found that macroscale transverse cracks in fibre composites are caused by the coalescence of the interfacial fibre/matrix debonds via cracks kinked out to the matrix [1,2]. Therefore, a considerable attention has been directed to the interfacial debonding of the fibres subjected to a transverse load as well as to the interfacial crack kinking into the matrix.

The determination of the fibre/matrix interface strength and fracture parameters is challenging. Due to the elastic mismatch, the fibre/matrix interface debonding is essentially mixed mode cracking. In order to investigate debonding initiation, a single fibre specimen subjected to a transverse load has been studied in the literature (Figure 1). The problem of a single fibre under transverse load has received considerable attention especially in numerical simulations which aimed to predict the damage initiation and propagation by applying an energy-based fracture mechanics approach [3–7]. It was found that the debonding propagates unstably starting from $\theta_d = 0°$ (or $\theta_d = 180°$ (see Figure 1 for notation), to the angle of $\theta_d = 60° - 70°$ under mixed mode conditions, dominated by normal opening for debond angles smaller than 30°. Subsequently, for $\theta_d > 60°$ the growth of the interfacial crack is stable in tangential opening [4].

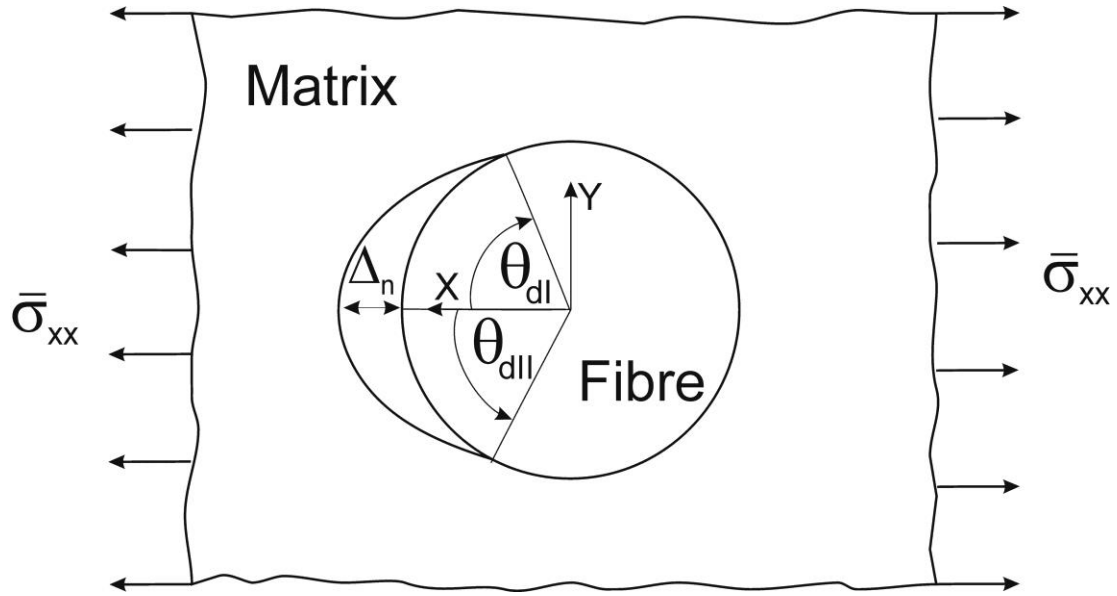

Figure 1. Single- fibre model composite under transverse load.

Crack kinking out of the interface into the matrix has been studied as well [3,4,7]. It was found, that the most plausible angle for the kinking to occur is in the interval of $\theta_d = 60° - 70°$ with the respect to the direction of the applied load (Figure 1) [4]. The difference between energy release rate of the crack when initiating the propagation through the matrix (crack kinking) with that released when continuing to grow along the interface was shown to reach the maximum in this interval. The path of a crack kinking out of an interface between dissimilar materials studied before by Evans et al. [8] shown that the magnitude of the phase angle at the crack tip, dictates whether the interfacial crack propagates along the interface or deviates into the adjoining material. A general problem of the crack penetration at interfaces and the crack deflection to the substrate was studied by energy release rate approach [9] and by cohesive-zone approach [10]. The results of He and Hutchinson [9] show that the interfacial crack kinking phenomenon is controlled by the relation of the interface toughness and the bonded materials' toughness. Parmigiani and Thouless [10] found that the crack propagation path is controlled by the ratio of substrate to the interface cohesive strength more than by their toughness.

An interface of a single fibre composite under transverse load has been also studied by a mixed mode cohesive-zone approach [11]. The relation of the shear strength of the interface to a normal strength was estimated in this study. However, the simulations were carried out in 3D without including the kinking issue.

A single fibre specimen is a suitable way to determine fibre/matrix interface properties. However, in order to study the transverse macrocracking initiation, the interfacial crack kinking phenomenon should be included in the study. Therefore, A-FEM is proposed for numerical simulations of this problem. It allows for simultaneous debonding initiation studies, its propagation and crack kinking out of the interface [12,13] .

In this paper a coupled experimental and numerical approach is presented for studying damage initiation and propagation in a single fibre specimen under transverse load. An approach to create a rigorous link between microscale fracture parameters and overall composite behaviour is first to identify the microscale fracture parameters from a single fibre specimen and then use the identified properties in micromechanical model consisting of multiple fibres to predict composite fracture. Results from previous work in which single fibre specimens were tested inside the chamber of scanning electron microscope (SEM) are used to estimate the interface parameters through the numerical simulations. The mixed mode fracture energy of fibre/matrix interface and the interface cohesive law parameters are estimated. A parametric study is performed in order to investigate the influence of cohesive law parameters on the debond initiation and propagation. The interfacial crack kinking is studied by the same coupled experimental and numerical approach.

2 Review of experimental findings

In the previous work (manuscript submitted: *In situ determination of a mixed- mode fracture energy of a glass fibre/matrix interface*), the debonding initiation and evolution was observed *in situ* by performing the tensile tests inside the vacuum chamber of SEM. The thick glass fibre with the diameter of ~50μm and the epoxy resin were used for the samples manufacturing. Details of samples manufacturing are described elsewhere [14]. The major findings of those experiments will be summarized in this section.

Although the loading conditions in the experiments are expected to be symmetric as indicated in Figure 1, the interface debonding was observed to start and propagate always on the same side of the fibre (at $\theta_d = 180°$ in Figure 1). The nominal stress required for the first debonding to occur was found to be in the range of $\bar{\sigma}_{xx} = 3-5MPa$. The debond crack propagated unstably to a crack arrest at the debond angle of $\theta_d = 40° - 60°$ as shown in Figure 2a. The debond crack grew at subsequent load steps reaching $\theta_d \sim 60° - 70°$ at the applied stress of 10-12 MPa. Since the problem is considered symmetric about the *x*-plane, two debonding angles can be measured as indicated in Figure 1. Therefore, for each sample two sets of debond angles are measured denoted as debond angle I and II, θ_{dI} and θ_{dII} respectively (see Figure 1).

The maximum normal openings of the debond, Δ_n (measured at $\theta_d = 180°$ as shown in Figure 1) for all load steps are shown in Figure 2b.

At the average stress of $\bar{\sigma}_{xx} \sim 13MPa$, the interface crack was observed to kink out into the matrix as shown in Figure 3c. The interface crack was found to kink out at an average debond angle of $\theta_d = 57 \pm 13°$ with respect to the applied load direction. The kinked crack propagated unstably in direction nearly perpendicular to the applied load.

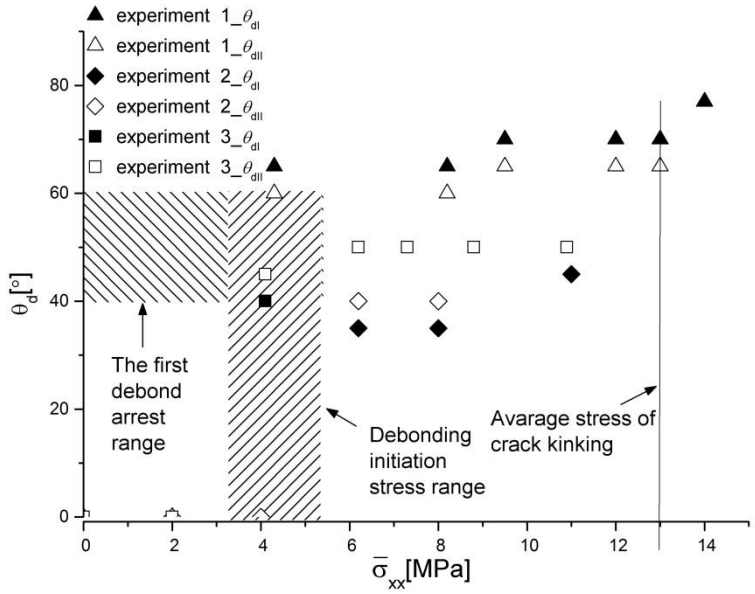

(a)

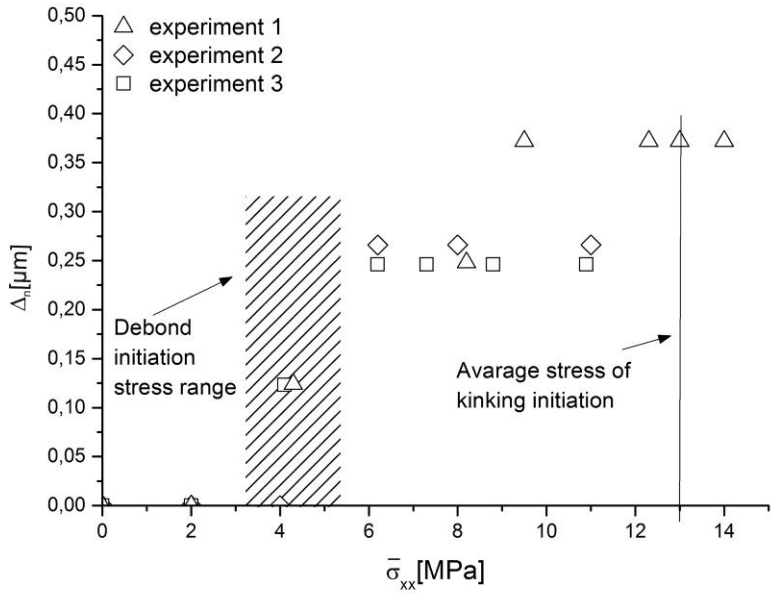

(b)

Figure 2. Experimental results: (a) normal opening and (b) angle of debonding crack tip as functions of applied nominal stress.

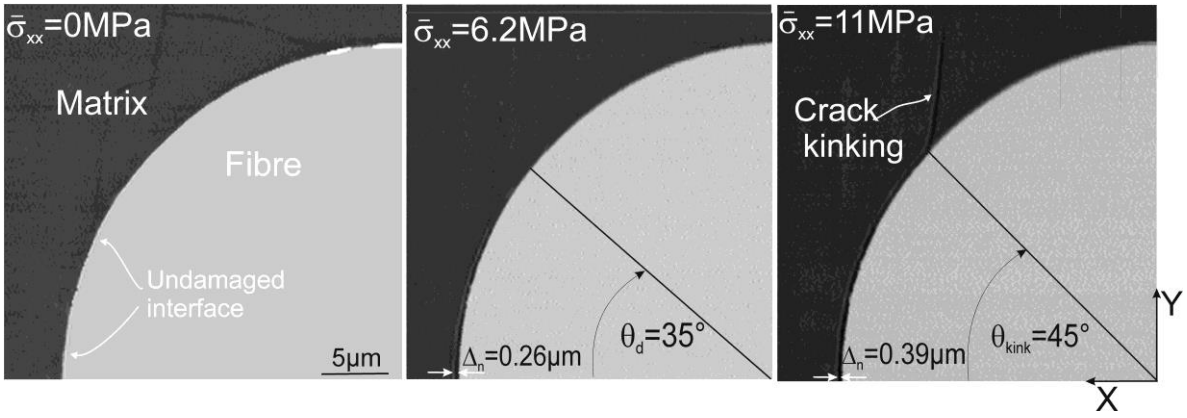

Figure 3. Micrographs of interfacial damage sequence: a) debonding initiation, b) debond propagation and c) kinking into the matrix.

3 Numerical modelling

In the current study, three numerical models were analysed. The geometry of the model is the same in all cases. They are meshed with different elements though (elastic or cohesive ones), depending on the studied problem as it will be described later on. A 2D domain with the size of 2 mm x 2 mm, represents the part of the sample tested in experiments (marked with the red square in Figure 4).

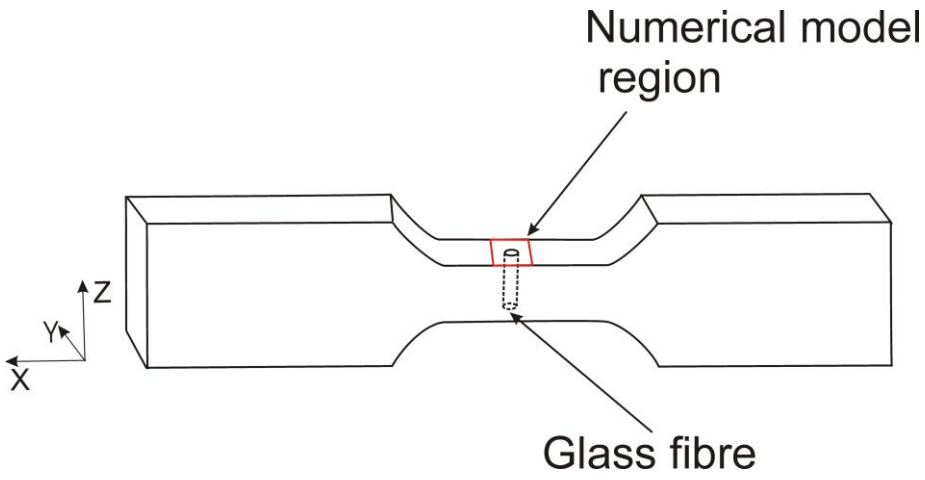

Figure 4. Sample tested in the experiments and numerical model region.

The single fibre with a diameter of *D*~ 0.05 mm is located in the centre of the model. The left edge of the model is fixed (U_1=0) and a uniform stretching is imposed in *x*-direction on the right edge ($U_1=\Delta U_1$) as shown in Figure 5a. The other edges are traction free ($\sigma_{yy} = \sigma_{xy} = 0$). The problem is symmetric about *x* and about *y*- axis (see Figure 1), and in principle a quarter of the fibre could be considered. However, the full representation model is more close to the realistic experimental set up and test. The entire model was meshed with 16434 4-node plain strain elements. Since no significant evidence of matrix plasticity was observed in the *in situ* tests, elastic material properties were assumed for both the matrix and fibre domains. The Young's modulus and Poisson's ratio for the fibre are $E_f = 70GPa$, $\nu_f = 0.21$ and those for the matrix are $E_m = 4GPa$, $\nu_f = 0.3$. The matrix's parameters are based to the data provided by the manufacturer of the epoxy resin used in the experiments. The fibre parameters have not been determined experimentally and therefore they are set close to the data found in the literature [15].

In models used in this study no damping was used. The details of each model will be described in following sections.

3.1 Model I: Elastic model for pre-debonding simulations

At first, the domain shown in Figure 5a was meshed with ABAQUS 6.12 continuum elements. The model is used for the stress analysis around the fibre and uses perfect bonding at the interface. The

nominal stress was applied to the domain as indicated in Figure 5a. The predicted stress concentration will be used for the cohesive strength estimation in Sec. 4.

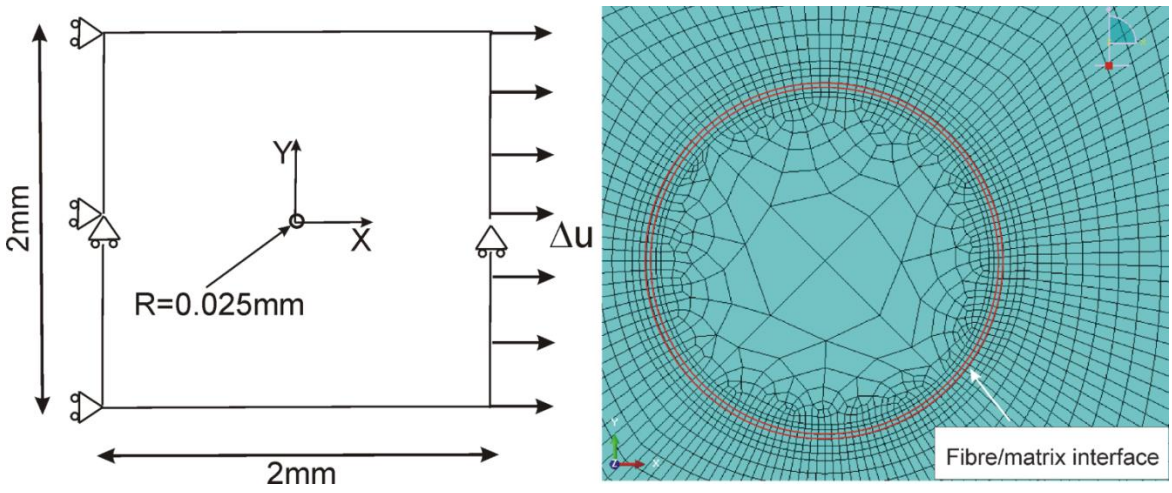

Figure 5. A-FEM model: a) model scheme with boundary conditions, b) a magnified view of meshed model (the fibre surrounding area).

3.2 Model II: Cohesive-zone model of interfacial debonding

In order to characterize the fibre/matrix interfacial debonding, a mode-dependent cohesive-zone model was developed using A-FEM. For this purpose, all elements in the model were replaced by user-defined augmented elements.

The A-FEM does not need to model the fibre/matrix interface explicitly as a single layer of cohesive elements [16]. The interface is embedded into the ring of solid elements representing a weak discontinuity highlighted in red in Figure 5b. That is, all these elements have two materials domains that are initially bonded together perfectly. As load increases, however, the debonding will initiate along the interface when the critical interface stresses are reached [16].

The length of the interface elements is much smaller than the cohesive zone length which is estimated as [17],

$$l_{Ic} = \frac{\Gamma_{Ic} \times E'}{(\hat{\sigma})^2} \qquad (1)$$

where E' is an elastic modulus of the matrix [18], $\hat{\sigma}$ is the peak stress in the Mode I cohesive law and Γ_{Ic} is a fracture energy for pure Mode I. For fracture under pure Mode II the cohesive zone length is estimated also by applying Eq. (1), with $\Gamma_{Ic} \to \Gamma_{IIc}$ and $\hat{\sigma} \to \hat{\tau}$, where Γ_{IIc} is the fracture energy for pure Mode II, and $\hat{\tau}$ is the peak stress for Mode II. However, for mixed mode cracks, it is satisfactory that the elements size is smaller than lesser of the cohesive zone lengths estimated for either pure Mode I or pure Mode II [17].

In this study, a mixed mode cohesive law with assumed triangular traction-separation relation for Mode I and Mode II fracture is used (Figure 6).

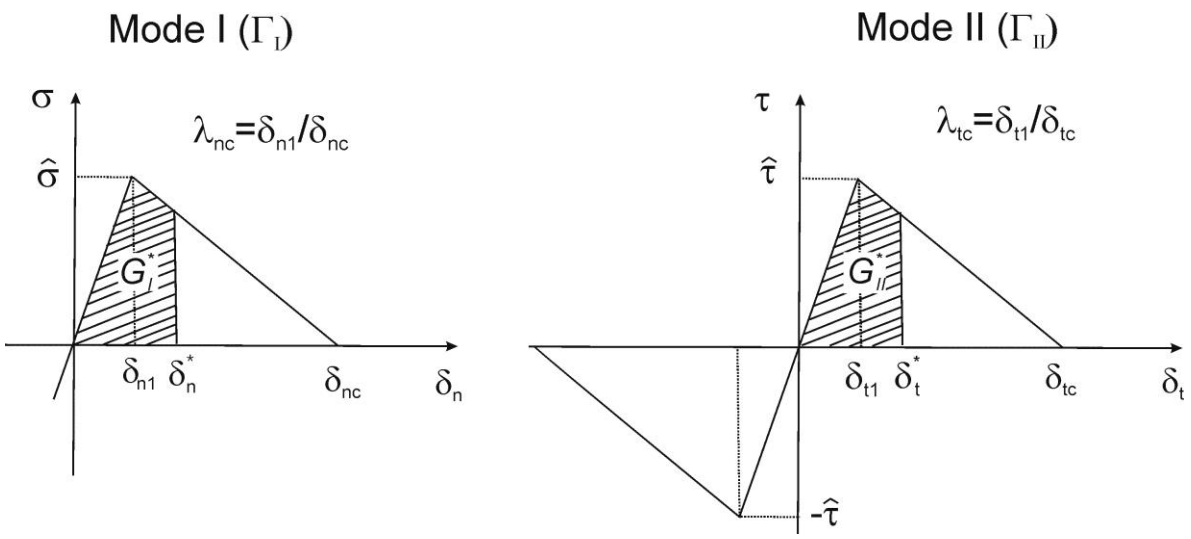

Figure 6. Mixed-mode cohesive laws used in this study.

Following Yang & Thouless [19], it is recognized that the total traction-separation work absorbed during fracture process, G, can be separated into the opening and shear components, G_I and G_{II} respectively,

$$G^* = G_I^* + G_{II}^* \qquad (2)$$

G_I and G_{II}, represent the work of the cohesive tractions per unit area which can be calculated by integration of the Mode I and Mode II traction-separation curves [19] shown in Figure 6:

$$G_I^* = \int_0^{\delta_n^*} \sigma(\delta_n) d\delta_n \tag{3}$$

$$G_{II}^* = \int_0^{\delta_t^*} \tau(\delta_t) d\delta_t \tag{4}$$

where δ_n, δ_t denote the normal and tangential displacement respectively, σ, τ corresponding to normal and shear tractions. The critical normal and tangential displacements (the displacements at which the tractions vanish), are denoted as δ_{nc} and δ_{tc}, respectively. The pure Mode I and pure Mode II fracture energies can be obtained from Eq. (2) and (3) with $\delta_n^* = \delta_{nc}$ and $\delta_t^* = \delta_{tc}$ respectively, giving $\Gamma_I = \hat{\sigma}\delta_{nc}/2$ and $\Gamma_{II} = \hat{\tau}\delta_{tc}/2$.

The opening and tangential traction-separation laws are uncoupled and related by a failure criterion [20]:

$$G_I^* / \Gamma_I + G_{II}^* / \Gamma_{II} = 1 \tag{5}$$

where, Γ_I and Γ_{II} are Mode I and Mode II toughness respectively, represented by the total areas given by the traction-separations curves for each mode (Figure 6).

In order to initiate the debonding only on one side of the fibre as it was observed in the experiments, non-even interface parameters were prescribed around the fibre as presented in Figure 7. On one side of the fibre ($x < 0$ in Figure 1), the interface is several times stronger than the interface on the other side of the fibre ($x > 0$ in Figure 1).

In the remainder of this paper the fracture parameters for the interface and those for the matrix will be denoted with subscripts *i* and *m* respectively.

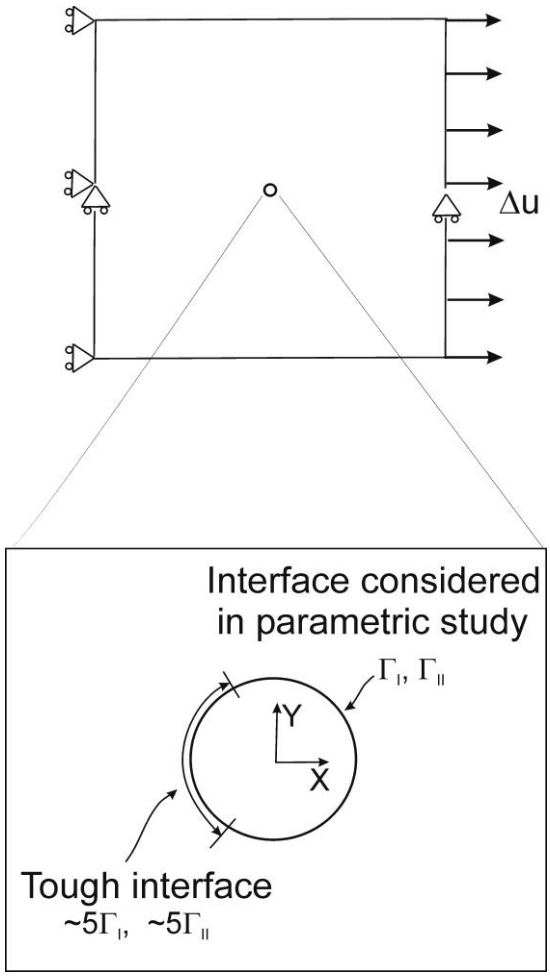

Figure 7. Uneven properties around the fibre applied in the model.

3.3 Model III: Cohesive-zone model of interfacial crack kinking

Once the fibre/matrix interface cohesive laws parameters were estimated, the interfacial crack kinking phenomenon was included in the simulations. Since the whole model was meshed with A-FEM elements, a study of the multiple intra-element discontinuity was possible [12]. The kinking crack simulations required only allowing a secondary crack into the matrix when the principle stress in the matrix meets a maximum stress criterion. The cracking through the matrix occurs only when the criterion in Eq. (5) is fulfilled. The triangular cohesive laws described in the previous section were assumed for the matrix domain.

4 Interface cohesive law parameters determination- approach

The two key parameters for Mode I interface cohesive law, the strength, $\hat{\sigma}_i$ and the normal critical opening displacement, $\delta_{nc\,i}$ can be determined from the experimental results as follows. We assume that before debonding initiation, the entire problem is purely elastic and the debonding observed at $\theta_d = 0°$ is predominantly Mode I (Figure 1). Thus, $\hat{\sigma}_i$ can be deduced from the stress concentration analyses (described in Sec. 3.1.), which shown that the normal stress at the location of the debonding initiation is 1.5 higher than the nominal applied stress ($\sim 1.5 \times \bar{\sigma}_{xx}$). Given that experimentally observed nominal stress corresponding to the debonding initiation is $\bar{\sigma}_{xx} = 3\text{-}5MPa$ the normal cohesive strength is thus determined to be in the range of $\hat{\sigma}_i = 1.5 \times \bar{\sigma}_{xx} = 4.5\text{-}7.5MPa$. The range of Mode I critical displacement, $\delta_{nc\,i}$ can be also estimated from the experimental results. It was found that at the first debond arrest observed at the applied stress of $\bar{\sigma}_{xx} = 3\text{-}5MPa$, the normal opening reached $\Delta_n \sim 0.17\mu m$ (Figure 2a). An open crack - a complete separation- is seen in Figure 3b, which indicates that $\delta_{nc\,i} < 0.17\mu m$.

For the parameters determination for fracture Mode II, it is noted that for many interfaces, the Mode II fracture energy, Γ_{II} has been found to be several times larger than fracture energy Mode I, Γ_I [22–25]. Therefore, in the present study we vary $\Gamma_{II\,i} / \Gamma_{I\,i}$ by adjusting the normal and tangential critical opening, $\delta_{nc\,i}$ and $\delta_{tc\,i}$ as well as cohesive strength for Mode I and Mode II, $\hat{\sigma}_i, \hat{\tau}_i$.

5 Interface cohesive law parameters - results

Selected results obtained from numerical predictions are shown in the present section. Predicted debond angles, θ_d and normal openings, Δ_n are plotted as functions of applied stress, so that they can be compared with the experimental measurements from Figure 2. θ_d in numerical predictions is determined using failure criteria described in Eq. (5). The last element of the interface whose damage criteria reached nearly 1, ($G_I / \Gamma_I + G_{II} / \Gamma_{II} > 0.96$), was considered to be the

debond crack tip and thereby used for identification of θ_d. In the simulations, the debond angles distinguished as θ_{dI} and θ_{dII} in Figure 1, are found to evolve symmetrically about *x*-plane; therefore, only the averaged debond angle, θ_d, $\theta_d = (\theta_{dI} + \theta_{dII})/2$ will be presented.

5.1 The interface Mode I fracture energy, $\Gamma_{I\,i}$

Several analyses were run in order to find the Mode I fracture energy which allows for obtaining the debonding initiation at the stress level determined experimentally, $\bar{\sigma}_{xx} = 3\text{-}5MPa$. The parameters for Mode I cohesive law were kept in the range which was determined from the experimental results as described in Sec. 4. The debonding initiation was found to occur at $\bar{\sigma}_{xx} = 3\text{-}5MPa$ (the range found in the experiments), for the interface Mode I fracture energy being in the range of $\Gamma_{I\,i} = 0.075\text{-}0.1J/m^2$. Having estimated $\Gamma_{I\,i}$ a set of analyses was carried out in order to verify whether the LEFM approach is applicably for the interface debonding. If the LEFM assumption of small-scale fracture process zone was fulfilled, the debond initiation and propagation would depend only on the fracture energy and all cohesive law parameters would be unimportant [26]. Therefore, in all cases included in this study the fracture energy is kept constant and equals $\Gamma_{I\,i} \sim 0.075J/m^2$. The cohesive law parameters are varied as shown in Table 1. $\hat{\sigma}_i = \hat{\tau}_i$ is adjusted so that $\Gamma_{I\,i}$ is the same in all cohesive laws. The ratio of fracture energy Mode II over Mode I is kept constant ($\Gamma_{II\,i}/\Gamma_{I\,i} = 4$).

Numerical predictions for θ_d and Δ_n as functions of applied stress are shown Figure 8. For all predictions presented in this parametric study except of simulations for which $\hat{\sigma}_i = \hat{\tau}_i = 0.75MPa$, the debond initiation falls within the range determined experimentally (see Figure 2 for comparison). The interface crack propagates unstably until arrest at $\theta_d = 40° \pm 5°$. The damage evolution is different for each simulation and clear effects of cohesive law parameters are seen. Roughly speaking, with increasing $\hat{\sigma}_i = \hat{\tau}_i$, θ_d reached at the final stress levels increases (Figure

8a). Predicted values of Δ_n for the stress level of $\bar{\sigma}_{xx} > 5MPa$ are similar for all simulations (Figure 8b). The only difference in the opening evolution is observed in the debonding initiation stage, for $\bar{\sigma}_{xx} < 5MPa$.

Since $\Gamma_{I\,i}$ and $\Gamma_{II\,i} / \Gamma_{I\,i}$ are kept constant but the resulting fracture behaviour is significantly different, the influence of the cohesive law parameters on the debond initiation/evolution is studied in the following sections.

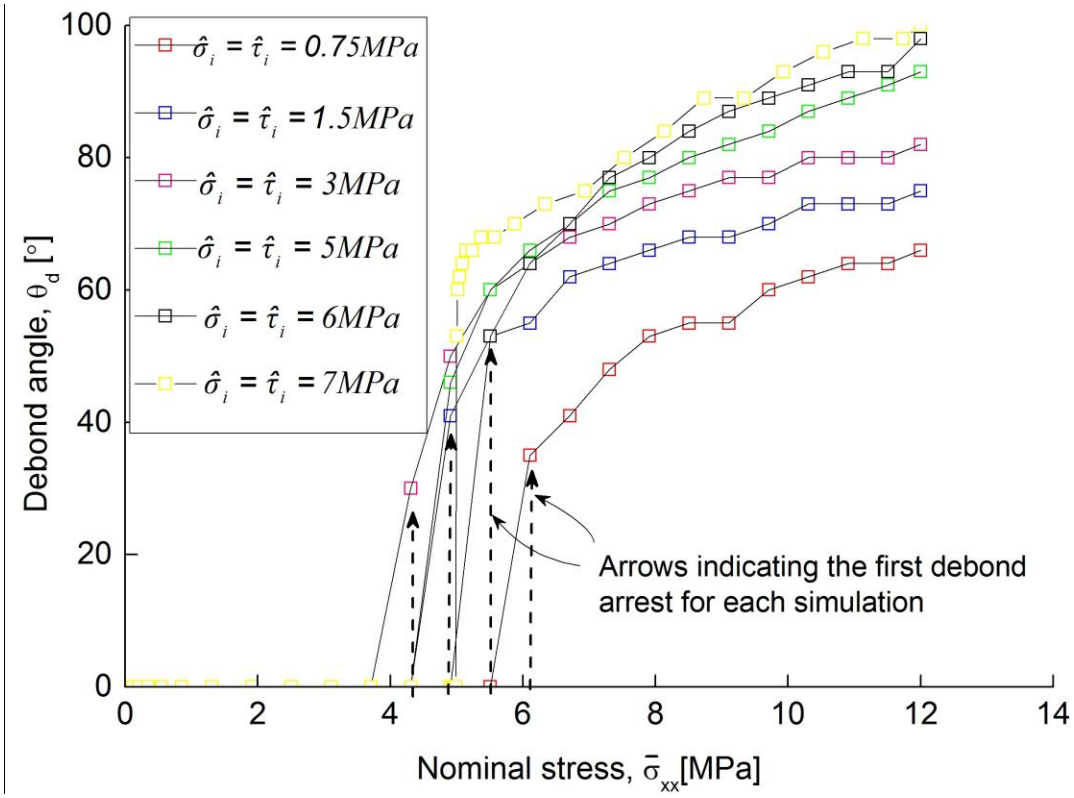

(a)

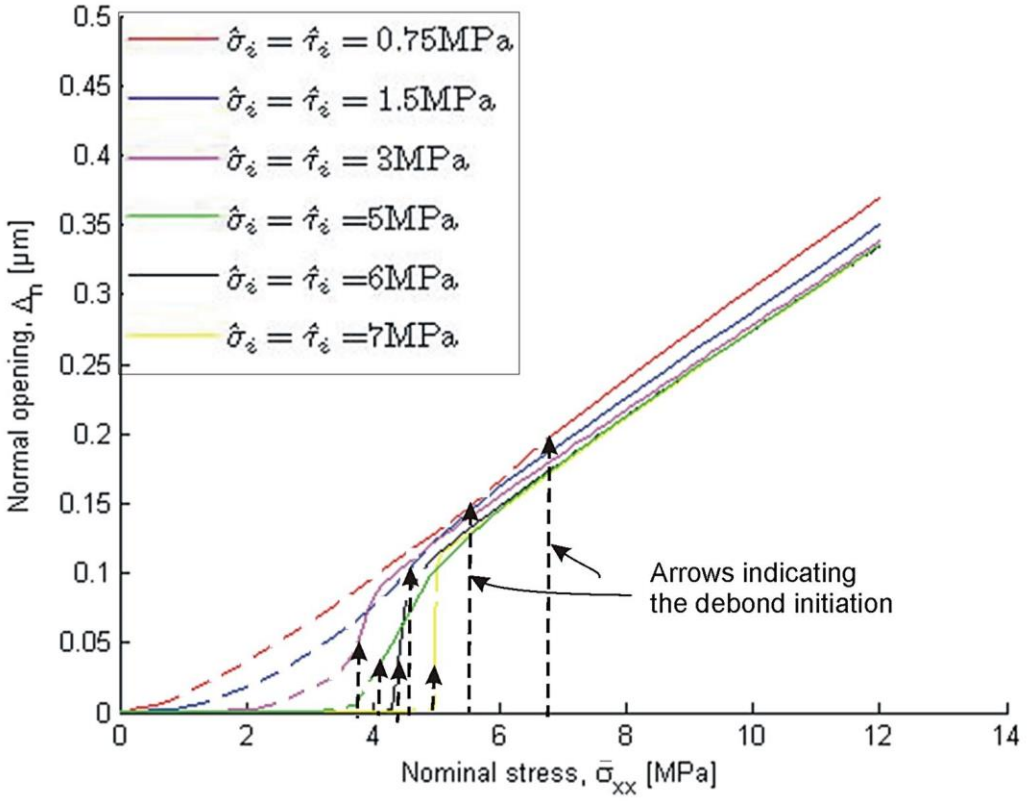

(b)

Figure 8. Cohesive strength influence on the debond propagation; a) debond angles and b) normal openings as functions of applied stress- numerical predictions.

Table 1 Cohesive law parameters used in parametric study for cohesive strength.

$\hat{\sigma}_i = \hat{\tau}_i$ [MPa]	$\delta_{nc\,i}$ [μm]	$\delta_{tc\,i}$ [μm]	$\Gamma_{II\,i} / \Gamma_{I\,i}$ [-]	$\Gamma_{I\,i}$ [J/m^2]
0.75	0.2	0.8	4	0.075
1.5	0.1	0.4	4	0.075
3	0.05	0.2	4	0.075
5	0.03	0.12	4	0.075
6	0.025	0.1	4	0.075
7	0.0214	0.0857	4	0.075

5.2 Cohesive critical normal opening displacement, $\delta_{nc\,i}$

The influence of the normal critical opening displacement, $\delta_{nc\,i}$ on the debonding initiation and propagation was studied next. The Mode I and Mode II cohesive strengths were set as $\hat{\sigma}_i = \hat{\tau}_i = 5MPa$ and the normal critical displacement, $\delta_{nc\,i}$ was systematically changed but kept as $\leq 0.2\mu m$. By changing $\delta_{nc\,i}$, the fracture toughness which is determined as $\Gamma_I = \hat{\sigma}\delta_{nc}/2$, was changed as well. The ratio of the critical opening displacement for Mode II and Mode I was kept the same, $\delta_{tc\,i}/\delta_{nc\,i} = 4$ (Table 2).

Figure 9a shows the predictions of θ_d as a function of applied stress. It can be noticed that the first predicted debond arrest is observed at $\theta_d = 30° - 45°$ in case of each cohesive law. However, the first debond occurs at different nominal stress, $\bar{\sigma}_{xx}$. Only in case of cohesive law whose $\delta_{nc\,i} = 0.03\mu m$ and $\delta_{nc\,i} = 0.04\mu m$, the debonding initiation falls within the range determined by the experiments. For $\delta_{nc\,i} > 0.04\mu m$ (and thus for $\Gamma_{I\,i} > 0.075J/m^2$, see Table 2), the

debonding occurs at the higher stress levels. This is due to the higher critical opening of those cohesive laws. It can be seen in Figure 9 that the debonding initiation (indicated as the first debond angle in Figure 9a), occurs when $\delta_{nc\,i}$ is reached (see Figure 9b). Predicted Δ_n obtained for cohesive laws whose $\delta_{nc\,i} = 0.03\mu m$ and $\delta_{nc\,i} = 0.04\mu m$ are close to those measured in the experiments (see Figure 2). Roughly speaking, with increasing $\delta_{nc\,i}$, the nominal stress, $\overline{\sigma}_{xx}$ required for the debonding initiation increases.

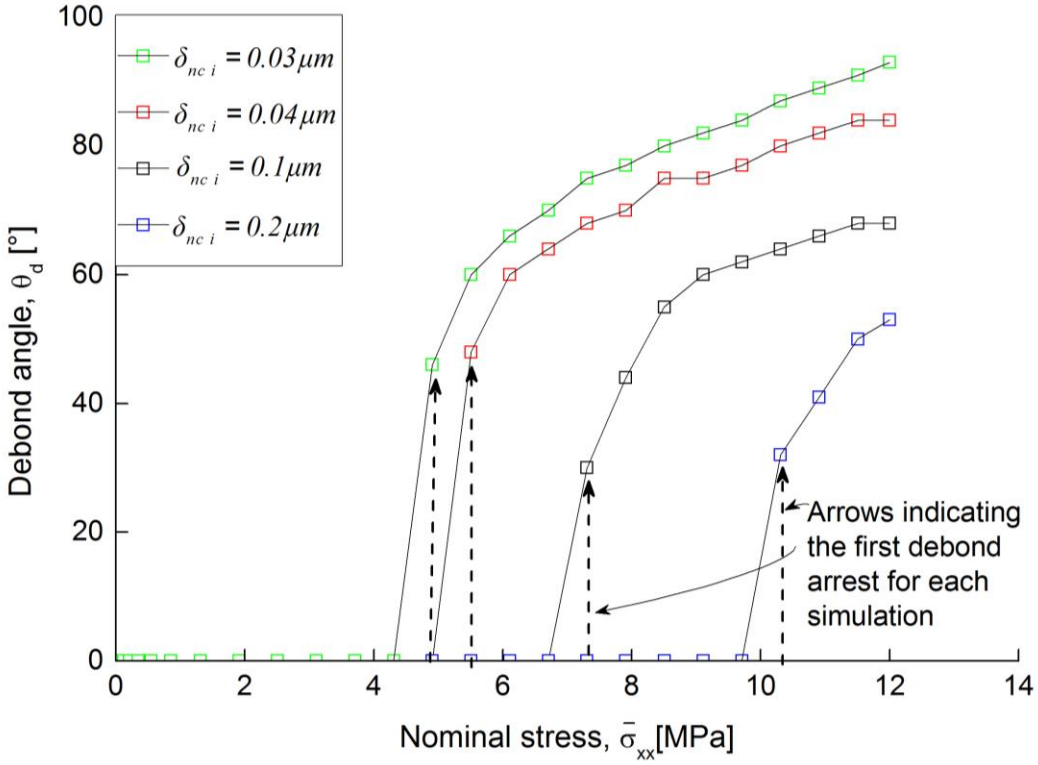

(a)

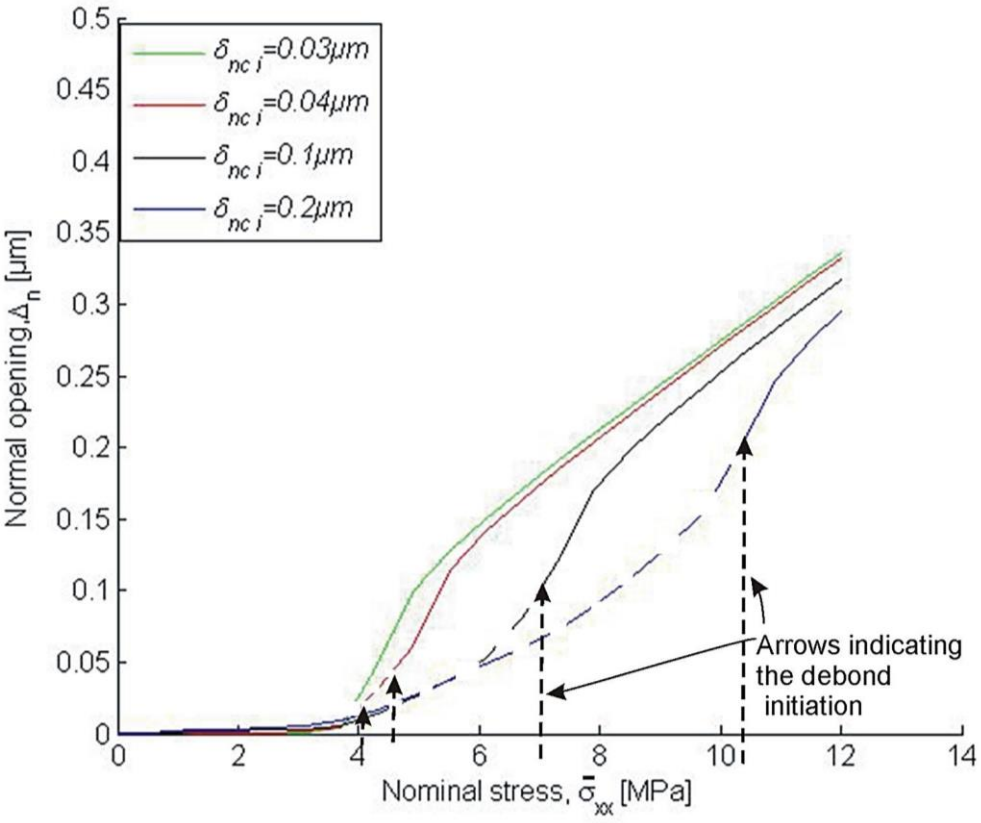

(b)

Figure 9**.** Interface fracture energy influence on the debond propagation; a) debond angles and b) normal openings as functions of applied stress- numerical prediction.

Table 2. Cohesive law parameters used in parametric study for interface fracture energy.

$\hat{\sigma}_i = \hat{\tau}_i$ [MPa]	$\delta_{nc\,i}$ [μm]	$\delta_{tc\,i}$ [μm]	$\delta_{tc\,i} / \delta_{nc\,i}$ [-]
5	0.03	0.12	4
5	0.04	0.16	4
5	0.1	0.4	4
5	0.2	0.8	4

5.3 Cohesive critical tangential opening displacement, $\delta_{tc\,i}$

Next, the influence of the critical tangential displacement, $\delta_{tc\,i}$ was studied. All cohesive law parameters for Mode I were kept constant and $\delta_{tc\,i}$ was varied, so that the ratio $\delta_{tc\,i} / \delta_{nc\,i}$ was varied as well (Table 3).

The numerical results are presented in Figure 10. Predicted θ_d propagates unstably and it evolves in the similar manner at the initiation range for all cases. However, the propagation of θ_d is different for different $\delta_{tc\,i} / \delta_{nc\,i}$. θ_d is the highest for $\delta_{tc\,i} / \delta_{nc\,i} = 2$. Moreover, it can be seen that when $\delta_{tc\,i} / \delta_{nc\,i} > 12$, θ_d is not influenced by $\delta_{tc\,i} / \delta_{nc\,i}$ any more. The evolution of θ_d obtained from the numerical predictions for the cohesive laws whose $\delta_{tc\,i} / \delta_{nc\,i} > 4$, is in the best agreement with the experimental results (see Figure 10a and Figure 2 for comparison). Predicted Δ_n are found to be only weakly influenced by $\delta_{tc\,i} / \delta_{nc\,i}$ (Figure 10b), and they are in good agreement with experimental measurements (see Figure 2b for comparison).

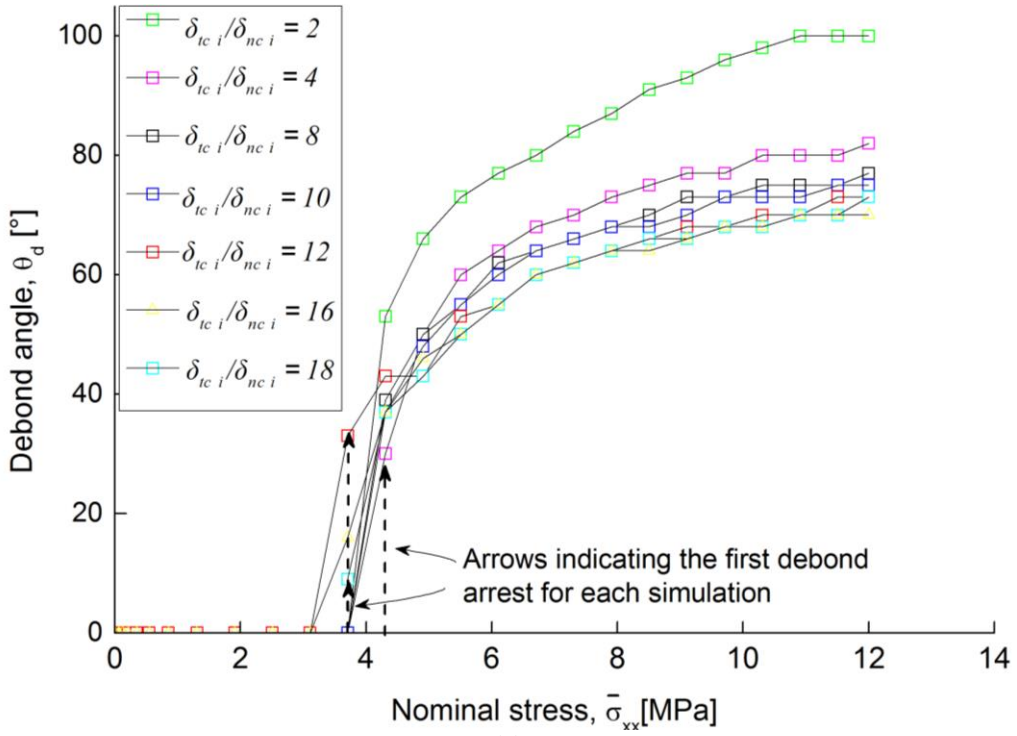

(a)

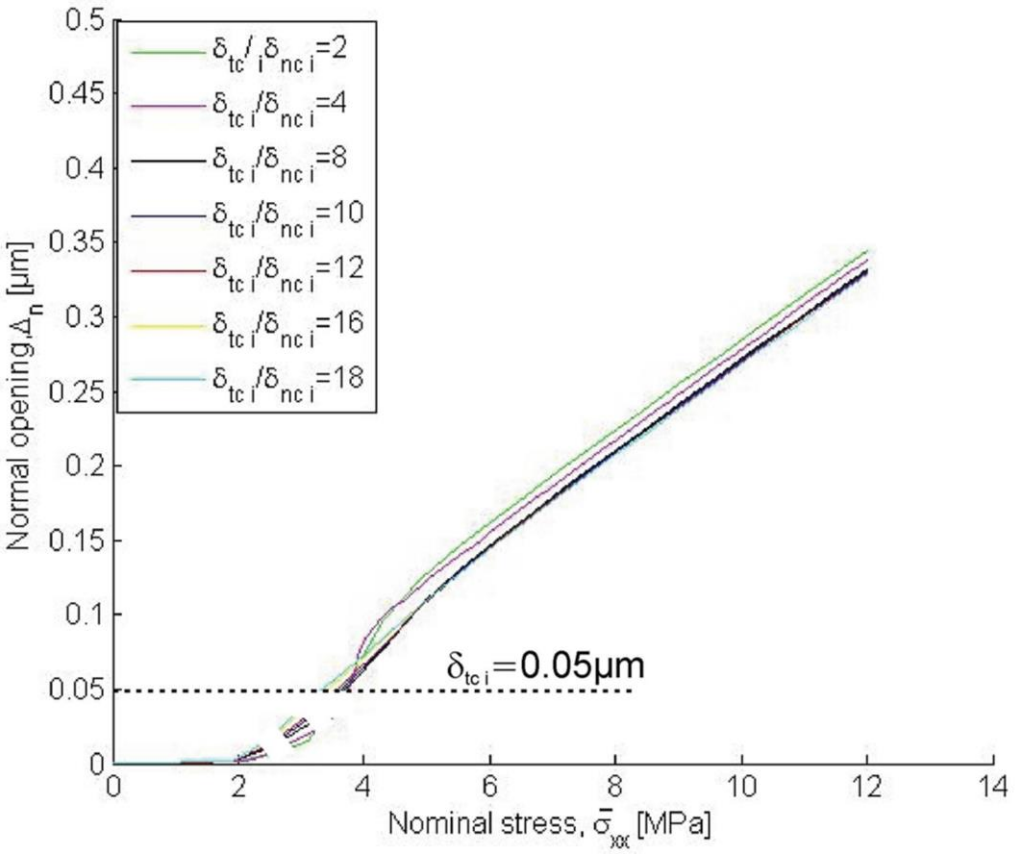

(b)

Figure 10. Parametric study for mode mixity; a) debond angles and b) normal openings as functions of applied stress- numerical predictions.

Table 3 Cohesive law parameters used in parametric study for interface fracture mode mixity.

$\hat{\sigma}_i = \hat{\tau}_i$ [MPa]	$\delta_{nc\,i}$ [μm]	$\delta_{tc\,i}$ [μm]	$\delta_{tc\,i} / \delta_{nc\,i}$ [-]
3	0. 05	0.1	2
3	0. 05	0. 2	4
3	0. 05	0. 4	8
3	0. 05	0. 5	10
3	0. 05	0. 6	12
3	0. 05	0. 8	16
3	0. 05	0. 9	18

5.4 Cohesive strength Mode II over Mode I, $\hat{\tau}_i/\hat{\sigma}_i$

The influence of the Mode II cohesive stress peak, $\hat{\tau}_i$ on the debonding initiation/propagation is presented next. $\hat{\tau}_i$ was varied as shown in Table 4. The results are presented in Figure 11. Again, the debond propagates unstably until $\theta_d = 20° - 55°$. The stress level of the debond initiation is in similar range for all cohesive laws. The debond evolution is different though. With increasing $\hat{\tau}$ (and thereby increasing $\hat{\tau}_i / \hat{\sigma}_i$), θ_d reached at the final stress levels decreases. Predicted θ_d as a function of applied stress are in the best agreement with experimental measurements for cohesive laws whose $\hat{\tau}_i / \hat{\sigma}_i > 2$. This ratio ($\hat{\tau}_i / \hat{\sigma}_i > 2$) is slightly larger than the one found for the same material system in [11] , $\hat{\tau}_i / \hat{\sigma}_i > 0.7\text{-}1.2$. Predicted Δ_n obtained for cohesive laws with $\hat{\tau}_i / \hat{\sigma}_i > 2$ are slightly lower than the experimental measurements (see Figure 11b and Figure 2b for comparison). Roughly speaking, with increasing $\hat{\tau}_i / \hat{\sigma}_i$, predicted θ_d and Δ_n decrease.

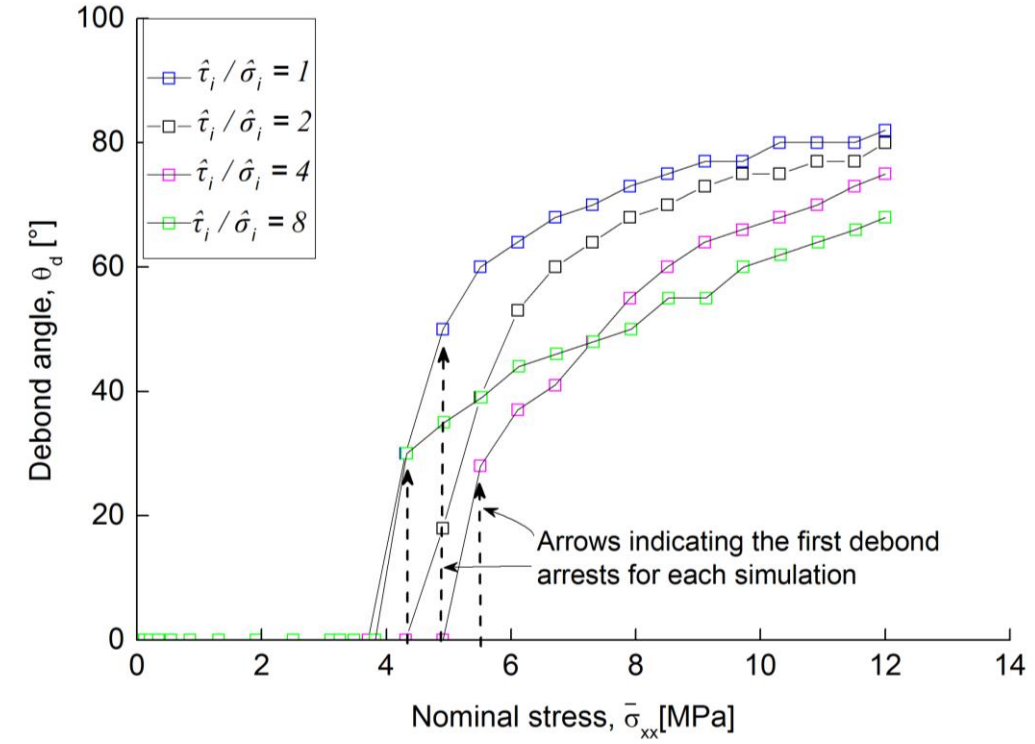

(a)

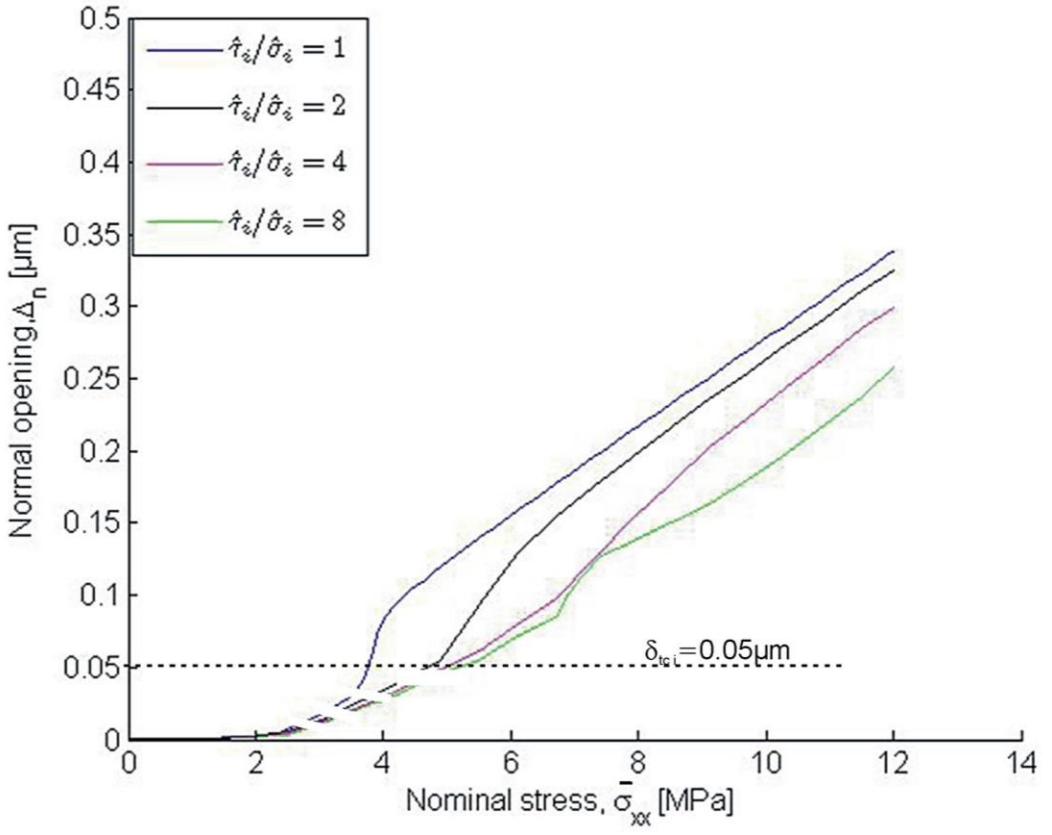

(b)

Figure 11. Parametric study for mode mixity; a) debond angles and b) normal openings as functions of applied stress- numerical predictions.

Table 4 Cohesive law parameters used in parametric study for interface cohesive strength ratio.

$\hat{\sigma}_i$ [MPa]	$\hat{\tau}_i$ [MPa]	$\hat{\tau}_i / \hat{\sigma}_i$ [-]	$\delta_{nc\,i}$ [μm]	$\delta_{tc\,i}$ [μm]
3	3	1	0.05	0.2
3	6	2	0.05	0.2
3	12	4	0.05	0.2
3	24	8	0.05	0.2

7 Fracture parameters determination for the interface crack kinking – approach

Based on the experimental results and on previous numerical studies of kinking phenomena by Paris et al. [4], it is noted that the crack kinked into the matrix propagates in pure Mode I. Therefore, it can be expected that the matrix cohesive law parameters for fracture Mode II do not influence the growth of the kinked crack. Thus, in the numerical simulations of the crack kinking, the matrix cohesive law for Mode I and Mode II are kept the same, $\hat{\sigma}_m = \hat{\tau}_m$ and $\Gamma_{I\,m} = \Gamma_{II\,m}$.

In the experiments the first kinking was observed at the average applied stress of $\bar{\sigma}_{xx} \sim 13MPa$ and the interfacial crack kinked at average angle of $\theta_d = 60° \pm 14°$ (example in Figure 3c). Therefore, in the numerical simulations the applied stress was kept at the level of $\bar{\sigma}_{xx} \sim 13MPa$ and matrix cohesive law parameters were changed systematically until the kinking occurred. Subsequently, the influence of the matrix fracture toughness and matrix cohesive strength on the kinking initiation was studied. In the numerical simulations of crack kinking, the same cohesive laws described in Sec.3.2 were used.

8 Interface crack kinking- results

For interfacial crack kinking simulations the interface cohesive parameters were held fixed according to the results presented in the previous section: $\hat{\sigma}_i = \hat{\tau}_i = 5MPa$, $\Gamma_{I\,i} \sim 0.1J/m^2$, and $\Gamma_{II\,i}/\Gamma_{I\,i} = 4$. Several analyses were carried out using different matrix cohesive strength, $\hat{\sigma}_m = \hat{\tau}_m$. It was found that the maximum $\hat{\sigma}_m = \hat{\tau}_m$ for which the interface crack kinks into the matrix at the nominal stress level determined experimentally ($\bar{\sigma}_{xx} \sim 13MPa$) is $\hat{\sigma}_m = \hat{\tau}_m = 39MPa$. Moreover, for $\hat{\sigma}_m = \hat{\tau}_m = 39MPa$ kinking is predicted to occur at the angle of $\theta_d \sim 60°$ regardless the matrix toughness Mode I and Mode II, $\Gamma_{I\,m} = \Gamma_{II\,m}$ as it can be seen in Figure 12.

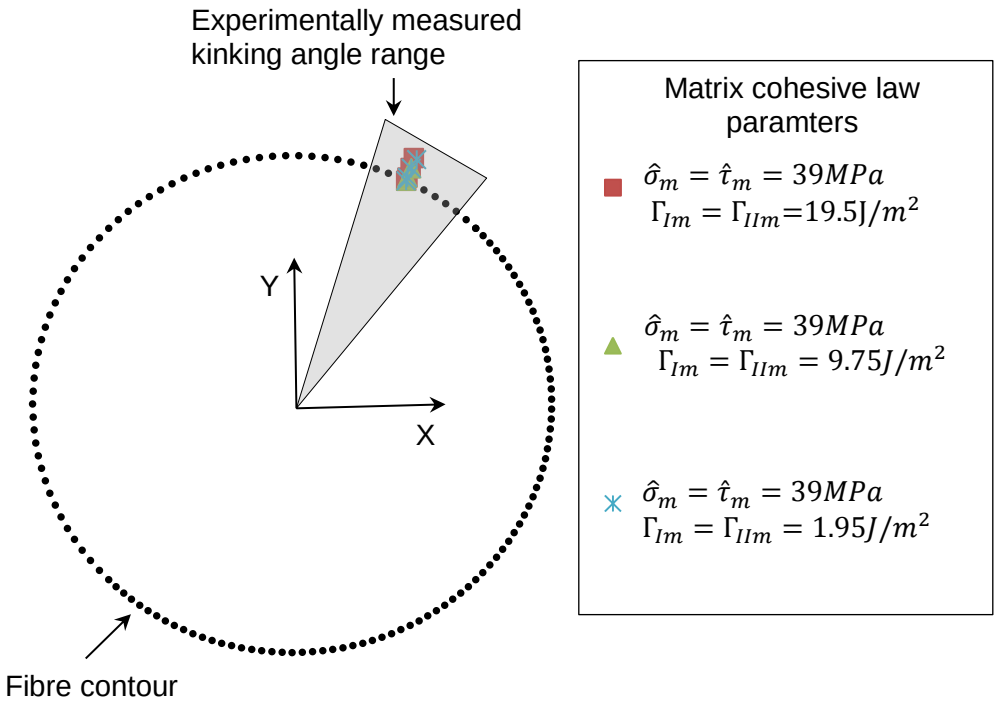

Figure 1. Numerical predictions for the crack kinking initiation obtained for the same matrix strength, $\hat{\sigma}_m = \hat{\tau}_m = 39$ and different interface toughness, $\Gamma_{I\,m} = \Gamma_{II\,m}$. The area marked with grey colour indicates the kinking angle determined in SEM observations.

This indicates that the interfacial crack kinking initiation is primarily controlled by $\hat{\sigma}_m$ and does not depend on $\Gamma_{I\,m}$. For the comparison with SEM observations, the experimental range of kinking angle is marked by grey are in Figure 12.

The study of the influence of $\hat{\sigma}_m$ on the kinking initiation shown that with increasing $\hat{\sigma}_m$, the angle of kinking position decreases (Figure 13). The range of experimentally measured kinking angle is marked as grey area. For $20MPa < \hat{\sigma}_m < 39MPa$, the kinking angle obtained from numerical predictions is in a good agreement with experimental measurements. This suggests that $\hat{\sigma}_m$ is within this range. In all analyses, the kinking crack propagated unstably and nearly in pure Mode I with respect to the applied load as it was observed in the experiments and as predicted by numerical simulation [4].

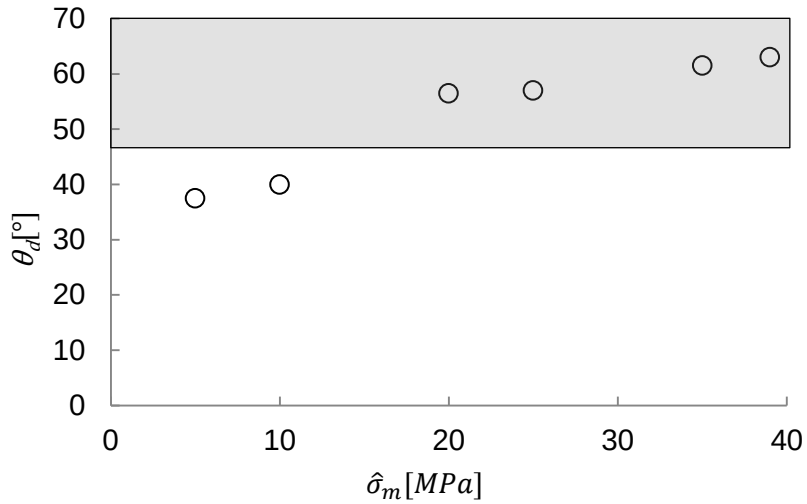

Figure 13. Kinking angle for different matrix strength. The grey are indicates the angle of the crack kinking determined in the experiments. Since it was found that the kinking initiation is independent on the matrix toughness (see Figure 12), in all analyses the matrix fracture toughness was chosen to be $\Gamma_{I\,m} = \Gamma_{II\,m} = 19.5J/m^2$.

8 Discussion

Interface mixed mode fracture energy

The mixed mode fracture energy of the fibre/matrix interface determined in this study is relatively low in comparison with other data from the literature [6]. It should be recognized, that the determined fracture energy is based on the surface observations in SEM. This technique enables a rather high magnification, but SEM testing allows only for the free surface observations of the sample. Due to the sample preparation procedure which involves surface polishing, the free surface observations may not be fully representative for the interface debonding inside the sample. Moreover, due to the complex stress state existing near the free surface of bi-material specimens [27], the stress state is different from that inside the specimen and the crack is expected to initiate at the free surface and subsequently propagate into the specimen. Nevertheless, the mixed mode fracture energy determined in the previous work, based on the LEFM approach, is in the similar range (manuscript in preparation). However, in the current paper it was shown that the interface debonding initiation and propagation is not controlled only by the fracture energy. The influence of the cohesive law parameters might indicate that the LEFM approach applicability for this problem should be further studied and verified.

Interface mixed mode cohesive law parameters identification

It is recognized that the cohesive law parameters estimation presented in this study is limited due to the experimental data. In SEM, *in situ* observations showed that the first debond arrest occurred when the debond angle reached $\theta_d = 40° \quad 60°$. Therefore, term 'debonding initiation' used for the first debond observed in the experiments is in fact the first debond arrest after it has propagated from $\theta_d = 0°$ (with respect to the applied load, where it is assumed to initiate), up to $\theta_d = 40° - 60°$. However, it is believed that by using the nominal stress level for debond initiation in the experiments, the analysis carried out using continuum elements in ABAQUS for the normal stresses estimation at the interface (at $\theta_d = 0°$, where the debond initiates), a reasonably accurate value for

$\hat{\sigma}_i$ was obtained (see Sec. 3 and 4). Moreover, the stress concentration estimated in this analyses seems to be in good agreement with the stress concentration calculated for the same problem of a single inclusion under transverse load elsewhere [21].

The Mode I interface critical opening, $\delta_{nc\,i}$ was estimated by experimental measurements of normal opening at the first debond arrest which corresponds to average value of $\delta_{nc\,i} < 0.17\mu m$ (Figure 2b). It was shown in this paper (e.g. Figure 9), that only for normal critical separation smaller than ~0.2μm, the numerical results are in good agreement with the experimental measurements. The normal opening measurements are limited by the SEM images resolution. The debond opening could be measured with higher resolution using e.g. Digital Image Correlation (DIC) system which has been proposed for microscopic displacement mapping using images acquired by SEM [28–30]. This would possibly allow for debonding observations at the earlier stage; but since the first stage of debonding is unstable, it is unlikely that the initiation had occurred at a significantly lower stress level. Moreover, DIC method enables for the measurements of both the normal and tangential crack opening displacements [30]. Thereby, the critical tangential displacement might be determined. In the experimental set up presented here, only normal opening was measured in fact. It should be therefore noticed, that the tangential crack openings are not directly measured in the experiments.

Interface crack kinking

The kinking angle obtained in the simulations is in good agreement with experimental observations. This indicates that the interface parameters determined in the first part of this study are in the right order of magnitude. Otherwise, for simulations for which the debond angle is much higher than that one determined experimentally, the kinking angle is likely to be higher than those found by experimental observations (or not occur at all as shown in the numerical analyses [4]).

The interfacial crack kinking was shown to be controlled by the matrix strength and independent on its fracture energy (Figure 12). This finding is similar to the results of model studies of the interface crack penetration into the substrate [10]. The crack penetration into the substrate or its deflection

into the interface was shown to be controlled by the substrate to the interface strength ratio rather than by their fracture energy. Further studies of the toughness/ strength role on the interfacial crack kinking to the matrix are required, so the results presented in this paper can be verified.

The matrix strength of $\hat{\sigma}_m = \hat{\tau}_m = 39MPa$ found in this study is rather low with comparison to the typical properties of the epoxies reported in the literature. According to e.g. Kinloch in [31], tensile fracture stress of the typical epoxy is ~63 MPa. However, it should be noticed that the reported values are usually relevant for the macroscopic materials parameters. (???)

8 Summary and conclusions

The fibre/matrix interfacial debonding initiation and propagation including subsequent interfacial crack kinking into the matrix was studied by a coupled experimental and numerical approach. The comparison of the results obtained from numerical predictions with the experimental measurements from the previous work allowed for the interface mixed mode cohesive law parameters identification.. The Mode I cohesive strength and critical opening displacement of the fibre/matrix interface have been found to be $5MPa > \hat{\sigma}_i > 0.75MPa$ and $\delta_{nc\,i} < 0.2\mu m$ respectively and thus the Mode I fracture energy is found to be on the level of ~0.1J/m^2. The interface Mode II fracture energy is found to be ~4 times higher than fracture energy Mode I. It was found that the fibre/matrix interface debonding propagation does not depend only on the fracture energy but also on the cohesive law parameters. The influence of the cohesive law parameters on the debonding initiation and propagation have been studied by numerical simulations using A-FEM The interfacial crack kinking into the matrix has been shown to be controlled by the strength of the matrix rather than its toughness. The short computation time without using any damping makes A-FEM an excellent and very promising tool for extending the study to models that include multiple fibres and study effects of microstructure. This would allow for studies of micro crack growth and coalescence which eventually leads to the formation of transversal macroscopic cracking.

Acknowledgements

The authors would like to thank to Danish Centre for Composites Structures and Materials for Wind Turbines for financial support of the part of the research carried out at the University of Miami, Department of Mechanical and Aerospace Engineering, US. Stergios Goutianos are thanked for advices for numerical simulations.

References

[1] Gamstedt EK, Sjoegren BA. Micromechanisms in tension-compression fatigue of composite laminates containing transverse plies. Composites Science and Technology 1999;59:167–78.

[2] Harrison RP, Bader MG. Damage development in CFRP laminates under monotonic and cyclic stressing. Fibre Science and Technology 1983;18:163–80.

[3] Correa E, Mantič V, París F. Numerical characterisation of the fibre–matrix interface crack growth in composites under transverse compression. Engineering Fracture Mechanics 2008;75:4085–103.

[4] París F, Correa E, Mantič V. Kinking of Transversal Interface Cracks Between Fiber and Matrix. Journal of Applied Mechanics 2007;74:703–16.

[5] Zhang H, Ericson ML, Varna J, Berglund LA. Transverse single-fibre test for interfacial debonding in composites: 1. Experimental observations. Composites Part A: Applied Science and Manufacturing 1997;28:309–15.

[6] Varna J, Berglund LA, Ericson ML. Transverse single-fibre test for interfacial debonding in composites:2. Modelling. Composites Part A: Applied Science and Manufacturing 1997;28A:317–26.

[7] Correa E, Mantič V, París F. Effect of thermal residual stresses on matrix failure under transverse tension at micromechanical level: A numerical and experimental analysis. Composites Science and Technology 2011;71:622–9.

[8] Evans AG, Dalgleish M, He M, Hutchinson JW. On crack path selection and the interface fracture energy in bimaterial systems. Acta Metall. Mater 1989;37:3249–54.

[9] He M-Y, Hutchinson JW. Kinking of a Crack Out of an Interface. Journal of Applied Mechanics 1989;56:270–8.

[10] Parmigiani J, Thouless M. The roles of toughness and cohesive strength on crack deflection at interfaces. Journal of the Mechanics and Physics of Solids 2006;54:266–87.

[11] Koyanagi J, Shah PD, Kimura S, Ha SK, Kawada H. Mixed-Mode Interfacial Debonding Simulation in Single-Fiber Composite under a Transverse Load. Journal of Solid Mechanics and Materials Engineering 2009;3:796–806.

[12] Liu W, Yang QD, Mohammadizadeh S, Su XY, Ling DS. An Accurate and Efficient Augmented Finite Element Method for Arbitrary Crack Interactions. Journal of Applied Mechanics 2013;80.

[13] Fang XJ, Yang QD, Cox BN, Zhou ZQ. An augmented cohesive zone element for arbitrary crack coalescence and bifurcation in heterogeneous materials. International Journal for Numerical Methods in Engineering 2011;88:841–61.

[14] Martyniuk K, Sørensen BF, Lauridsen EM, Modregger P. 3D in situ observations of glass fibre/matrix interfacial debonding. Composites Part A: Applied Science and Manufacturing 2013;In press.

[15] Brøndsted P, Lilholt H, Lystrup A. Composite Materials for Wind Power Turbine Blades. Annual Review of Materials Research 2005;35:505–38.

[16] Ling D, Yang Q, Cox B. An augmented finite element method for modeling arbitrary discontinuities in composite materials. International Journal of Fracture 2009;156:53–73.

[17] Yang Q, Cox B. Cohesive models for damage evolution in laminated composites. International Journal of Fracture 2005;133:107–37.

[18] Cox B, Marshall BD. Concepts for bridged cracks in fracture and fatigue. Acta Metall. Mater 1994;42:341–63.

[19] Yang QD, Thouless MD. Mixed-mode fracture analyses of plastically-deforming adhesive joints. International Journal of Fracture 2001;110:175–87.

[20] Wang J-S, Suo Z. Experimental Determination of Interfacial Toughness Curves Using Brazil-Nut-Sandwiches. Acta Metall. Mater 1990;38:1279–90.

[21] Achenbach JD, Zhu H. Effect of interfacial zone on mechancial behavior and failure of fiber-reinforced composites. J. Mech. Phys. Solids 1989;37:381–93.

[22] Cao HC, Evans AG. An experimental study of the fracture resistance of bimaterial interfaces. Mechanics of Materials 1989;7:295–304.

[23] Liechti KM, Chai YS. Asymmetric Shielding in Interfacial Fracture Under In-Plane Shear. Journal of Applied Mechanics 1992;59:295–304.

[24] Thouless MD. Fracture of a model interface under mixed-mode loading. Acta Metall. Mater 1990;38:1135–40.

[25] Jensen HM. Mixed mode interface fracture criteria. Acta Metall. Mater 1990;38:2637–44.

[26] Sørensen BF. Cohesive laws for assessment of materials failure: Theory, experimental methods and application. 2010.

[27] Bogy DB. Two Edge-Bonded Elastic Wedges of Different Materials and Wedge Angles Under Surface Tractions. Journal of Applied Mechanics 1971;38:377–86.

[28] Kang J, Jain M, Wilkinson DS, Embury JD. Microscopic Strain Mapping Using Scanning Electron Microscopy Topography Image Correlation at Large Strain. The Journal of Strain Analysis for Engineering Design 2005;40:559–70.

[29] Sutton MA, Li N, Garcia D, Cornille N, Orteu JJ, McNeill SR, Schreier HW, Li X, Reynolds a. P. Scanning Electron Microscopy for Quantitative Small and Large Deformation Measurements Part II: Experimental Validation for Magnifications from 200 to 10,000. Experimental Mechanics 2007;47:789–804.

[30] Sutton MA, Orteu J, Schreier HW. Image Correlation for Shape, Motion and Deformation Measurements. 2009.

[31] Kinloch AJ. T oughening Epoxy Adhesives to Meet Today ' s Challenges. MRS Bulletin 2003;28:445–8.

APPENDIX B1

Mixed mode cohesive law for fibre/matrix interface- a coupled experimental and numerical study

Proceedings of 19th International Conference on Composite Materials (ICCM-19), July, 2013, Montreal, Canada

MIXED MODE FRACTURE ENERGY OF FIBRE/MATRIX INTERFACE- A COUPLED EXPERIMENTAL AND NUMERICAL STUDY

K. Martyniuk[1]*, B.F. Sørensen[1], Q. Yang[2], W. Liu[2]
[1] Section of Composites and Materials Mechanics, Department of Wind Energy, Technical University of Denmark, Roskilde, Denmark,
[2] Department of Mechanical and Aerospace Engineering, University of Miami, Miami, USA
* Corresponding author (karm@dtu.dk)

Keywords: interface, *in situ*, cohesive law, mixed-mode

1 Introduction

It is well established that the microscale properties of composites strongly affect their macroscopic behaviour. In order to be able to understand the macroscopic behaviour of composites, detailed characterisation of the microscale properties is required. The properties of all composite materials constituents should be characterized, including fibre/matrix interface which plays a key role in the load transfer. It has been found that e.g. macroscale transverse cracks in fibre composites are caused by the coalescence of the interfacial fibre/matrix debonding [1].

Having characterized the relevant microscale mechanical properties including interface properites, overall mechanical properties can be predicted by micromechanical modelling. Moreover, a direct link between the microscopic properties with the macroscopic composite behaviour can be established. Therefore, an understanding and control of the interface properties is of high importance. Thus, the studies of the fibre/matrix interface cracking received considerable attention.

Fibre/matrix debonding is essentially mixed mode interface cracking. In order to investigate debonding initiation and propagation a single fibre specimen subjected to a transverse load has been studied in the literature. The problem is schematically shown in Fig.1. The fibre/matrix interfacial debonding has been studied mainly using Linear Elastic Fracture Mechanics (LEFM) approach. Toya [2], deduced the analytical solution of the energy release rate as a function of the debond angle for a circular inclusion embedded in infinite solid. The same approach was applied in numerical simulations elsewhere [3]. It was found that the debonding propagates unstably starting from $\theta_d = 0°$ to the angle of $\theta_d = 60° - 70°$ under mixed mode conditions, dominated by Mode I for debond angles smaller than 30° (nomenclature according to Fig.1). Subsequently, the growth of the interfacial crack is stable in pure Mode II or the interfacial crack kinks out into the matrix. Elsewhere, the fibre/matrix interface debonding was studied by mixed mode cohesive approach [4]. All numerical predictions availably in the literature were compared with experimental observations obtained by optical microscopy [3,4]. However, these observations do not allow for the precise debonding angle measurements. As mentioned, the interfacial crack occurs under mixed mode conditions. The debonding initiation is predominantly normal opening (Mode I). Subsequently, the crack is under mixed-mode conditions and mode-mixity evolves with the debond angle growth (contribution of a shear opening increases).

It is well established that for the interfaces bonding dissimilar materials the Mode II fracture energy, Γ_{II} is several times larger than energy Mode I, Γ_I [5-7]. Therefore, the fracture energy of the fibre/matrix interface must be determined for mixed mode conditions.

It should be noticed, that a single fibre specimen is only the first step in revealing a transverse crack nucleation in fibre composites. Once the interface parameters have been determined using a single fibre composite, the next step is to simulate a real composite microstructure that includes defects and a number of fibres to predict debonding, interfacial cracks kinking into the matrix, their subsequent coalescence leading to the transverse macro crack nucleation.

The current studies present a coupled experimental and numerical approach for fibre/matrix interface fracture parameters determination. An augmented finite element method (A-FEM) [8] has been used for numerical simulations and *in situ* fracture tests of a single-fibre specimen were conducted in the chamber of scanning electron microscope (SEM).

High resolution SEM micrographs allowed for debonding observations *in situ*. The debond angles and the debond opening displacements are measured as functions of the applied stress. By the comparison of experimental and numerical results micromechanical modelling parameters are identified. Cohesive law parameters are estimated and Mode I fracture energy is determined

2 Experimental method

A transverse tensile load was applied to a single fibre specimen as shown schematically in Fig.1. The sample is made of a thick glass fibre with diameter of ~50μm which is embedded in the epoxy resin. The fibres are pre-strained before casting in the resin in order to minimize the residual stress. The pre-straining procedure is carried out according to the method available in the literature [9]. The sample was dog-bone shaped and polished in order to remove any microcracks and to allow for microscopy observations. The surfaces to be observed in SEM were coated with the carbon coat to prevent charging of the non-conductive polymer. The geometry of the sample which was used in *in situ* tests is shown in Fig.2. The tensile tests were conducted in the chamber of SEM by applying a tensile load in *x*-direction (see Fig.2). A special load rig was used (see Fig.3). The load was applied in increments and the sample was partly unloaded after each increment to avoid any creeping during scanning time. The step-wise loading is shown schematically in Fig.4 where $\bar{\sigma}_{xx}$ is the applied stress. An acoustic emission (AE) sensor was mounted on the sample to assist the detection of the damage initiation/propagation.

3 Experimental results

The debonding initiation and propagation were successfully observed during *in situ* tests in SEM. An example of observed damage sequence is shown in Fig.5. Two characteristic features, the debonding angle, θ_d and the normal opening, Δ_n (see Fig. 1) were measured after each load step. However, in some cases due to the poor micrographs quality the debonding was not visible and no data was obtained. Since the problem is symmetrical along *x*-plane, two debond angles can be measured as indicated in Fig.1. The measured values as functions of applied stress are presented in Fig.6. The debonding propagated unstably right after its initiation and the first debond arrest was observed when the debond angle reached θ_d ~40°-60° at the stress level of $\bar{\sigma}_{xx} = 3-5MPa$ (see Fig.5 and 6). At subsequent stress levels the debond angle propagated and the normal opening evolved as seen in Fig.5 and Fig.6. At the average stress level of $\bar{\sigma}_{xx} \sim 13MPa$ the interfacial crack kinked out of the fibre/matrix interface into the matrix as seen in Fig.5c. The debond angle corresponding to kinking initiation is found to be in the interval of $\theta_d = 60° \pm 14°$.

3 Micromechanical modelling

A unit cell model consisting of 2×2mm matrix domain which includes the fibre with diameter of ~50μm was implemented in ABAQUS 6.12 through user-defined elements. Although, the problem is symmetric and in principle a quarter of the fibre with the surrounding matrix could be considered (symmetry along *x* and *y* plane, see Fig.1), for the studies of symmetry of the problem and capacity of the numerical method, the entire fibre is considered in the numerical simulations. The entire model was meshed with 4-nodal elements. Since no significant evidence of matrix plasticity was observed in the *in situ* tests, elasticity was assumed for both, the matrix and the fibre domains. The Young's modulus and Poisson's ratio for the fibre are $E_f = 70GPa$, $\nu_f = 0.21$ and those for the matrix are $E_m = 4GPa$, $\nu_f = 0.3$. The matrix's parameters are based on the data provided by the manufacturer of the epoxy resin used in the experiments. The fibre parameters are set close to the data found in the literature [3]. A-FEM was utilized for numerical simulations of fibre/matrix interfacial debonding [8,10]. The A-FEM does not need to model the fibre/matrix interface explicitly as a single layer of cohesive elements. The interface is embedded into the ring of solid elements containing the fibre/matrix interface as shown in Fig.7. That is, all these elements have two materials domain. As load increases, the debonding will initiate along the interface when the critical interface stresses are reached [10].

The triangular mixed mode traction-separation law was used for interfacial debonding simulations (Fig.8). The Mode I and Mode II traction-separation laws are only coupled by a failure criterion [11]:

$$G_{\mathrm{I}} / \Gamma_{\mathrm{I}} + G_{\mathrm{II}} / \Gamma_{\mathrm{II}} = 1 \qquad (1)$$

where, Γ_I and Γ_{II} are Mode I and Mode II fracture energy respectively, represented by the total areas

given by the traction-separations curves for each mode (Fig.8).

In the failure criteria described by Equation (1), G_I, G_{II} represent Mode I and Mode II work of the cohesive tractions given by

$$G_I = \int_0^{\delta_n} \sigma(\delta_n) d\delta_n \qquad (2)$$

$$G_{II} = \int_0^{\delta_t} \sigma(\delta_t) d\delta_t \qquad (3)$$

where δ_n and δ_t are normal and tangential displacement respectively, $\hat{\sigma}$, $\hat{\tau}$ are the peak normal and shear tractions, δ_{nc} and δ_{tc} are the critical normal and tangential displacements and δ_{n1} and δ_{t1} are the separations at which the peak normal and shear traction values are reached.

4 Coupled experimental and numerical study

The cohesive law parameters can be estimated by coupled experimental and numerical approach. Two parameters from numerical and experimental results are compared: interface debonding angle, θ_d and normal opening, Δ_n after the debonding crack is arrested (Fig.1). Firstly, Mode I parameters are determined by using experimental results as follows. It is recognized, that the debonding initiation at θ_d=0° is nearly Mode I opening [2]. Therefore, the Mode I cohesive strength is deduced by the stress analyses at this location at the applied nominal stress of $\bar{\sigma}_{xx} = 3-5MPa$ which caused debonding initiation in the experimental observations. The contour plot for the stress analyses which was made using continuum elements of ABAQUS is shown in Fig.9. It was found that the normal stress at the location of the debonding initiation (θ_d=0°) is ~1.5 times higher than the far field nominal stress. Thereby, the cohesive strength for fracture Mode I is found to be in the range of $\hat{\sigma} = 4.5-7.5MPa$.

Critical opening for Mode I cohesive law is also deduced from the experimental results. It is found that the normal opening at the initiation stage is $\Delta_n \sim 0.17\mu m$. It can be therefore deduced, that the critical opening of the Mode I cohesive law must be $\delta_{nc} < 0.17\mu m$.

Having deduced critical normal opening and the cohesive strength, several numerical simulations were run in order to find the Mode I fracture energy of the interface which allows obtaining the debonding initiation at the nominal stress of $\bar{\sigma}_{xx} = 3-5MPa$ as it was observed in the experiments. In the numerical simulations the cohesive strength was fixed and the critical normal opening and shear opening were adjusted. It is noted that for many interfaces, the Mode II fracture energy, Γ_{II} has been found to be several times larger than fracture energy Mode I, Γ_I [5-7]. Therefore, in the present study the fracture energy for Mode II over Mode I was chosen to be $\Gamma_{II}/\Gamma_I = 4$. All parameters for the cohesive laws used in this study are in Table 1.

5 Numerical results

The debond angle which was detected following the failure criteria from equation 1 is measured at each increment and so is the normal opening. The measured values are plotted as functions of applied stress in Fig.10a and Fig.10b. Since the numerically predicted debonding angles distinguished in Fig.1 as θ_{dI} and θ_{dII}, developed fairly symmetrically, the debond angle in Fig.10a is an averaged one, i.e., $\theta_d = (\theta_{dI} + \theta_{dII})/2$. In all cases the debonding occurs and propagates unstably and the first debond arrest is observed at the angle of $\theta_d = 30° - 45°$. The unstable debond propagation is in good agreement with experimental observations. The debonding initiation occurs at the stress level determined in the experiments for simulations whose cohesive critical displacement is in the range of $\delta_{nc} = 0.03-0.04\mu m$. However, the debond angles at the subsequent stress levels are slightly larger than those observed in the experiments (see Fig.6 for comparison and cohesive law parameters in Table.1). For larger critical displacement, the debonding angles at higher stress levels are in better agreement with experimental observations, although the debonding initiation in these cases requires higher stress level (see Fig.6 for comparison and Table.1 for cohesive law parameters). The fracture energy for Mode I and Mode II can be found as $\Gamma_I = \hat{\sigma}\delta_{nc}/2$ and $\Gamma_{II} = \hat{\sigma}\delta_{tc}/2$, respectively. Thus, from Fig. 10a, it appears that the interface toughness Mode I is in the range of $\Gamma_I = 0.1-0.25J/m^2$.

The normal opening (Δ_n) is also plotted as a function of applied stress and the 'stretching' of the interface observed before complete debonding occurs is included in Fig.10b. It can be seen that the debonding initiation occurs when the critical normal opening has been reached. All curves show a distinctive transition from an unstable phase (rapid increase of Δ_n with $\bar{\sigma}_{xx}$) to a stable phase (more

gradual increase of Δ_n) . The transition point Therefore, only in case of cohesive critical opening being in the range of $\delta_{nc} < 0.2\mu m$, the debonding initiation occurs in the desired nominal stress of $\bar{\sigma}_{xx} = 3-5MPa$ determined in the experimental testing. The critical normal opening displacement obtained in the numerical simulations where the fracture energy is in the range of $\Gamma_I \sim 0.1J/m^2$ are similar to the normal openings measured in SEM micrographs. For the fracture energy which is higher than 0.1J/m^2, the normal openings are slightly smaller than experimental ones shown in Fig.6.
All simulations are completed very fast in comparison with non-linear analysis conducted by standard FEM method.

6 Summary and conclusions

A new *in situ* method for debonding observations of fibre/matrix interface debonding is proposed. The sample manufacturing procedure allowed for obtaining a proper fibre/matrix bonding and removing all microcraks. The high resolution SEM images allowed for the *in situ* observations of the debonding process. By comparing the experimental measurements of debond angle and debond normal opening with numerical results obtained using A-FEM the Mode I fracture energy of the interface is found to be ~0.1J/m^2. The Mode I cohesive law parameters are identified by a coupled experimental and numerical approach. The cohesive strength is determined to be in the level of $\hat{\sigma} = 4.5-7.5MPa$ and normal critical opening is found to be $\delta_{nc} < 0.2\mu m$.
The fracture energy and the cohesive law parameters for fracture Mode II can be estimated by the parametric study which compares the debond angle and normal opening evolution from the experiments with numerical predictions. In the present study, the ratio of fracture energy for Mode II over Mode I was chosen to be 4. The debond angles obtained in the numerical predictions are slightly higher than those measured experimentally. Therefore, more parametric studies should be conducted in order to identify the interface parameters for fracture Mode II. It is expected, that the higher ratio of the fracture energies, Γ_{II}/Γ_I would results in smaller debond angles for subsequent stress levels and thereby, in better agreement with experimentally measured debond angles.
A-FEM is shown to be suitable for the cohesive zone modelling of the microscale problems.
In the future work the kinking phenomenon observed in the experiments should be included in the numerical simulations. Since the numerical method is found to be time efficient in the cohesive-zone simulations, it is expected that it will be competitive for standard methods like e.g. X-FEM for kinking problem simulations.

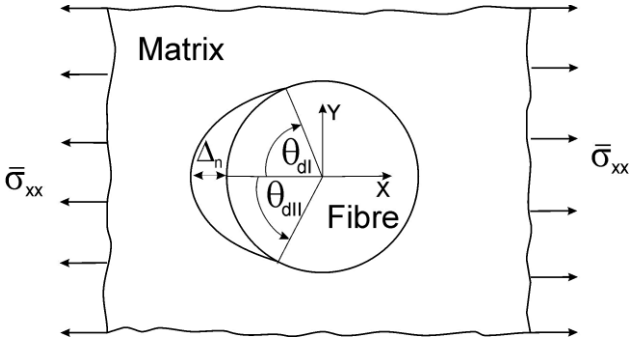

Fig.1. Single- fibre model composite under transverse load.

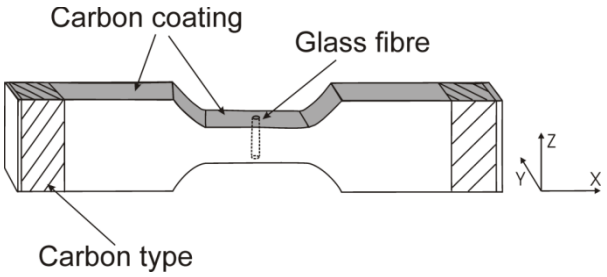

Fig.2. Sample geometry used in the *in situ* tests in SEM.

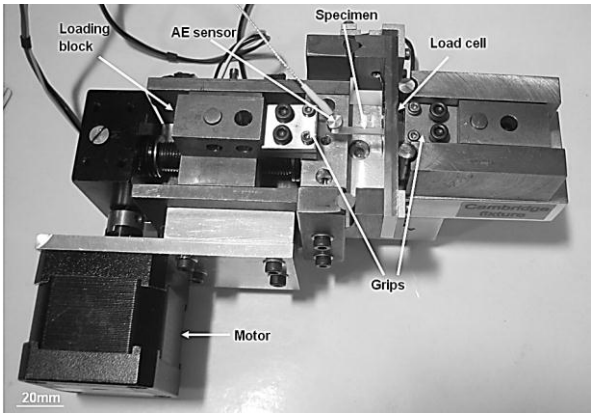

Fig. 3. Test set up for *in situ* SEM observations.

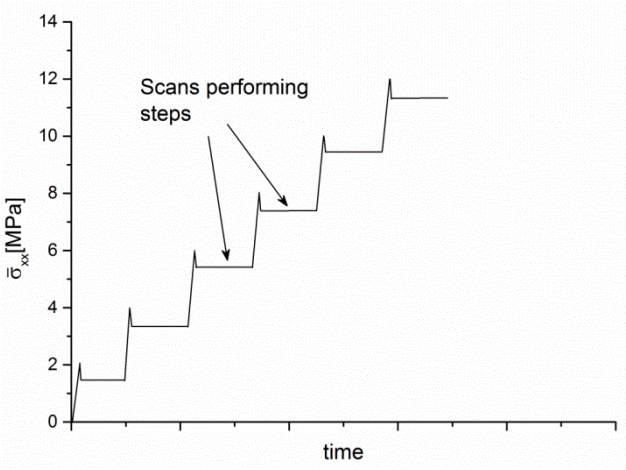

Fig.4. Step wise loading during *in situ* testing.

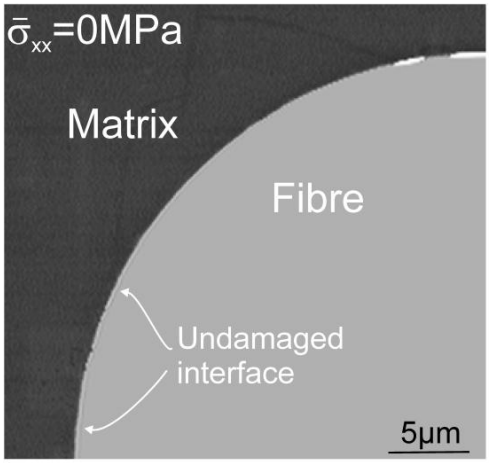

(a)

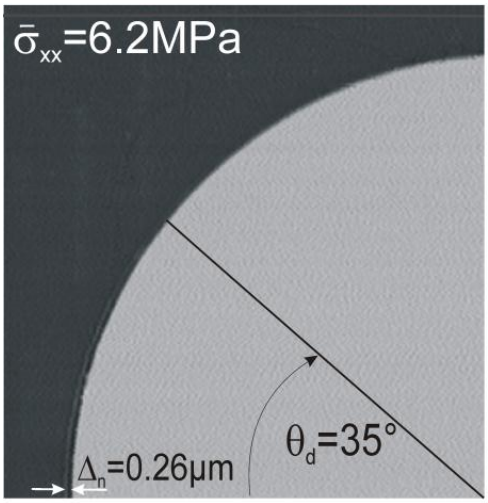

(b)

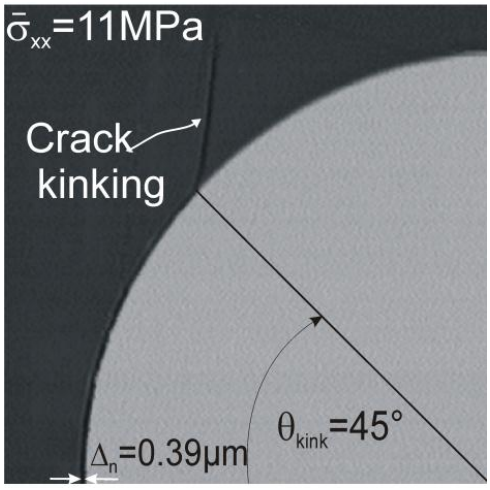

(c)

Fig. 5. Fibre/matrix interface: (a) undamaged interface, (b) interfacial debonding initiation, (c) interfacial crack kinking into the matrix

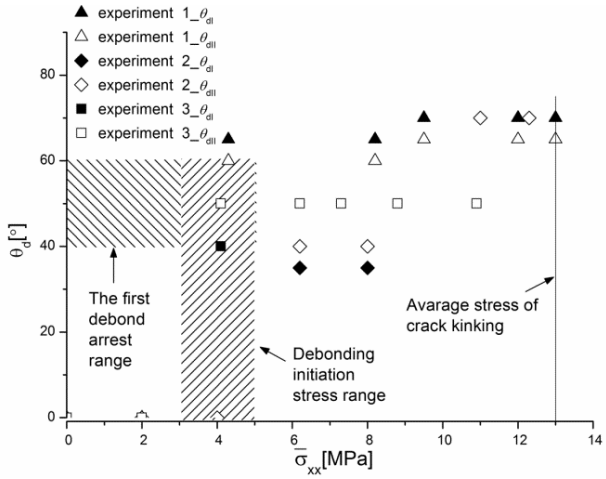

(a)

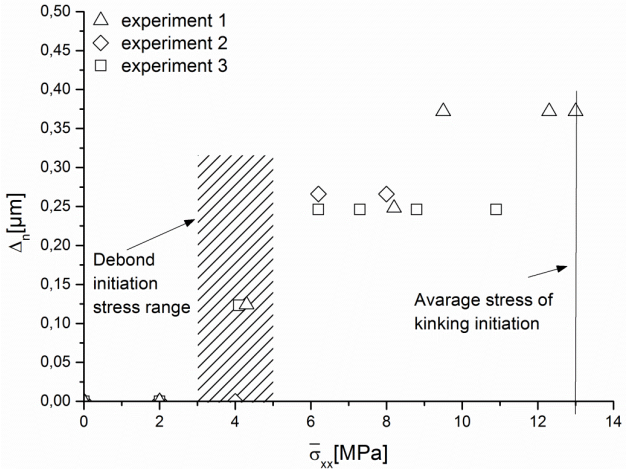

(b)

Fig. 6. Experimetnal results presented as functions of applied stress, (a) debond angle and (b) normal opening

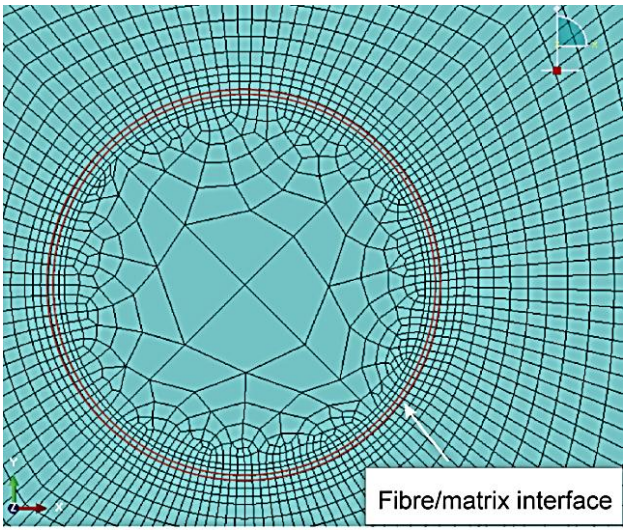

Fig. 7. Fibre/matrix interface represented by solid elements.

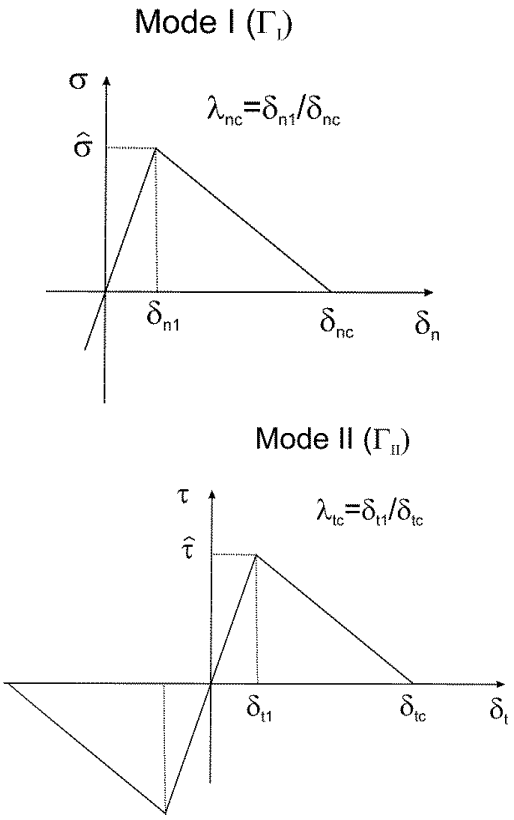

Fig. 8. Mixed-mode cohesive traction-separation laws used in this study.

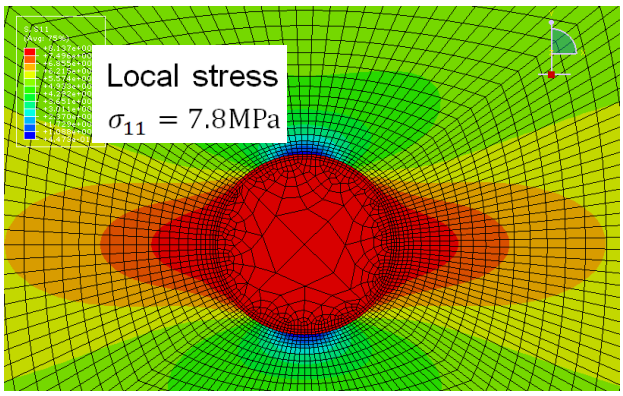

Fig. 9. Stress analyses for estimation of the cohesive strength Mode I; contour plot of local normal stress for the nominal stress $\bar{\sigma}_{xx} \sim 5MPa$.

Table 1. Cohesive parameters used in the numerical simulations

$\hat{\sigma} = \hat{\tau}$ [MPa]	δ_{nc} [µm]	δ_{tc} [µm]	$\delta_{tc} / \delta_{nc}$ [-]	Γ_I [J/m^2]
5	0. 03	0. 12	4	0.075
5	0. 04	0. 16	4	0.1
5	0. 1	0. 4	4	0.25
5	0. 2	0. 8	4	0.5

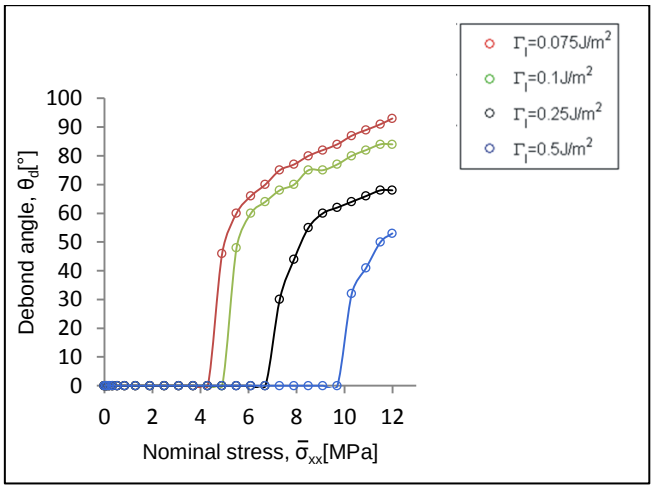

(a)

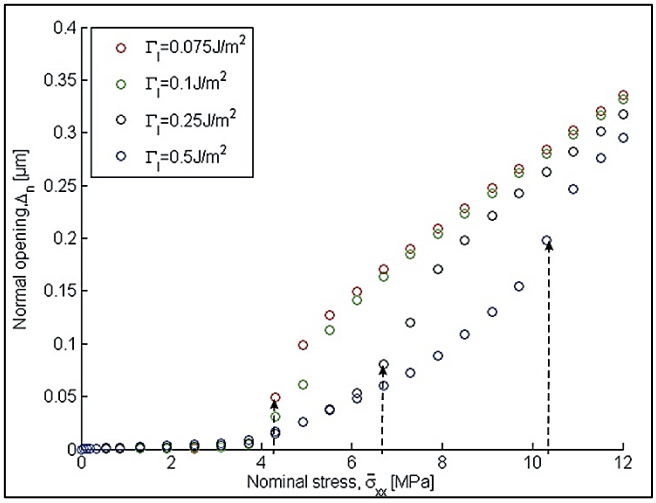

(b)

Fig. 10. Numerical results for different fracture energy, (a) debond angle as a function of applied stress and (b) normal opening as applied stress.

References

[1] E.K. Gamstedt, B.A. Sjoegren "Micromechanisms in tension-compression fatigue of composite laminates containing transverse plies". Composites Science and Technology, Vol. 59, pp 167-178, 1999.

[2] M. Toya, A crack along the interface of a circural inclusion embedded in an infinite solid, J. Mech. Phys. Solids. 22 (1974) 325–348.

[3] F. París, E. Correa, V. Mantič "Kinking of Transversal Interface Cracks Between Fiber and Matrix". Mechanics of Materials, Vol.7, pp295-304, 2007.

[4] J. Koyanagi, P.D. Shah, S. Kimura, S.K. Ha and H. Kawada "Mixed-Mode Interfacial Debonding Simulation in Single –Fiber Composite under a Transverse Load". Journal of Solid Mechanics and Materials Engineering, Vol.3, pp 796-806, 2009.

[5] K.M. Liechti, Y.S. Chai “Asymmetric Shielding in Interfacial Fracture Under In-Plane Shear”. Journal of Applied Mechanics, Vol. 59, pp 295-304, 1992.

[6] M.D. Thouless “Fracture of a model interface under mixed-mode loading”. Acta Metall. Mater., Vol. 38, pp 1135-1140, 1990.

[7] Z.S. J.-S. Wang, Experimental Determination of Interfacial Toughness Curves Using Brazil-Nut-Sandwiches, Acta Metall. Mater., Vol. 38, pp1279–1290, 1990.

[8] W. Liu, Q. D. Yang, S. Mohammadizadeh, X. Y. Su and D. S. Ling “An Accurate and Efficient Augmented Finite Element Method for Arbitrary Crack Interactions”. Journal of Applied Mechanics, Vol. 80, doi:10.1115/1.4007970 (12 pages), 2013.

[9] Q. Zhu, P.H. Geubelle, M. Li, C.L. Tucker “Dimensional Accuracy of Thermoset composites: Simulation of Process-Induced Residual Stresses”. Journal of Composite Materials, Vol. 35, pp 2171-205, 2001.

[10] D. Ling, Q. Yang, B. Cox “An augmented finite element method for modelling arbitrary discontinuities in composite materials”. International Journal of Fracture, Vol. 156, pp 53–73, 2009.

[11] J.-S. Wang, Z. Suo “Experimental determination of interfacial toughness curves using Brazil-nut-sandwiches”. Acta metall, mater. Vol. 38, pp 1279-1290, 1990.